CHARACTERIZATION AND MODELING OF A MEMS-BASED RESONANT MICRO HEAT ENGINE

By

HAMZEH KHALID BARDAWEEL

A dissertation submitted in partial fulfillment of
the requirements for the degree of

DOCTOR OF PHILOSOPHY

WASHINGTON STATE UNIVERSITY
School of Mechanical and Materials Engineering

AUGUST 2010

To the Faculty of Washington State University:

The members of the Committee appointed to examine the dissertation of HAMZEH KHALID BARDAWEEL find it satisfactory and recommend that it be accepted.

_____
Cecilia D. Richards, Professor, Chair

_____
Robert F. Richards , Professor

_____
Michael J. Anderson , Professor

_____
Su Ha, Professor

ACKNOWLEDGMENT

January 2006 was the month I started my journey in the graduate school. I still remember the first day in that journey. It was snowy and cloudy as every other winter day in Pullman. I was scared of tomorrow yet excited about the future. It did look as a long rough journey to me at that time. At that time, I was not sure if I would make it to the end. Now, after over four years from the time I started this journey, I still believe I would have not made it to the end without the help and support from my adviser Professor Cecilia Richards. Professor Michael Anderson and Professor Robert Richards have also been of great help to me. I thank them all for everything they have done to me. To my adviser Professor Cecilia Richards: from you I have learned beyond what I learned from textbooks and classes. I learned how to think "outside the box", how to be creative, and how to be engineer. From you, I have not only learned science and knowledge I, also, learned how to work in a team and how to interact with other colleagues. For that I'm thankful too. Thank you for supporting me in my "ups and downs". When I first came to Pullman, four years ago, I had no family here. But now I count you part of my family.

During my graduate work, many people have come and gone to the lab. Some of them have been very helpful to me. To my friend and colleague Leland Weiss I'm thankful. Thank you for coaching me on fabrication and experimentation. My friend John Youngsman requires special recognition and thanks. Thank you for all the engineering discussions we had.

CHARACTERIZATION AND MODELING OF A MEMS-BASED

RESONANT MICRO HEAT ENGINE

Abstract

by Hamzeh Khalid Bardaweel, Ph.D.
Washington State University
August 2010

Chair: Cecilia D. Richards

The focus of this dissertation is investigating the dynamic and the thermal behavior of a MEMS-based resonant micro heat engine. The thermodynamic cycle of the engine is also investigated. To completely characterize the operation of the engine a new experimental setup is built and used. A lumped parameter model of the engine is developed.

The model is validated against measured data. The velocity transfer function shows a broad plateau with a maximum value of 2.5mm/s/W. No resonant peak is observed over the frequency range 0.1-1000Hz. To reduce the resonant frequency of the engine a small mass is placed on top of the engine. The resonant frequency of the engine is reduced to 100Hz. The amplitude of the velocity transfer function reaches a maximum value of 10mm/s/W at resonant frequency. Thus, at resonance the amplitude of velocity transfer function is increased by a factor of 4. Experiments show that the amplitude of velocity transfer function increases by a factor of 1.5-8.5 when added mass is thermally isolated from the engine. Pulse durations less than 10% of the total engine cycle period are desirable.

Both resonant and off-resonant operations of the engine are investigated. The results show that resonant operation is valuable. For a fixed amount of energy delivered to the engine,

as the resonant operation is approached the cycle opens up and more mechanical work is observed. However, for an off-resonant operation pressure and volume become coupled and less mechanical work is observed.

The thermodynamic cycle of the engine has been acquired experimentally. Vapor pressure, vapor volume, vapor temperature, and vapor entropy changes inside the cavity of the engine are determined. The maximum measured pressure and volume changes are 45Pa and $0.55mm^3$, respectively. The data show that the engine operates at vapor temperature gradient less than 1^oC. Albeit the temperature gradient is low, the measured second law efficiency of the micro heat engine is about 16%. Major sources of irreversibility in the engine are heat transfer over finite temperature differences during heat addition and rejection, heat transfer into and out of engine thermal mass and viscous losses due to liquid working fluid motion.

TABLE OF CONTENTS

Page

ACKNOWLEDGEMENTS iii

ABSTRACT iv

TABLE OF CONTENTS vi

LIST OF TABLES x

LIST OF FIGURES xi

DEDICATION xiii

1. INTRODUCTION 1

1.1 Motivation and overview 1

1.2 Layout of dissertation 4

1.3 Literature review 5

1.3.1 Micro dynamic heat engines 5

1.3.2 Resonant micro heat engines 11

1.3.3 Thermoelectric engines 16

1.4 Objective of this work 21

2. INTRODUCTION TO MICRO HEAT ENGINE 23

2.1 Introduction 23

2.2 Micro heat engine 23

2.3 Micro heat engine operation 26

2.4 Thermal switch 29

3. FABRICATION OF MICRO HEAT ENGINE AND THERMAL SWITCH 32

3.1 Overview 32
3.2 Silicon wafer preparation 32
3.3 Fabrication of bottom membrane (evaporator) 33
3.4 Fabrication of wick micro channels 38
3.5 Fabrication of top membrane (expander) 39
3.6 KOH etching 40
3.7 Fabrication of thermal switch 40
4. EXPERIMENTAL SETUP AND PROCEDURE 44
4.1 Introduction 44
4.2 Experimental setup 44
4.2.1 Laser vibrometer 46
4.2.2 TTL circuit 48
4.2.3 Digital oscilloscope 49
4.2.4 Push-pull device 49
4.2.5 Piezo-stack actuator 50
4.2.6 Edge welded bellows 51
4.3 Experimental procedure 51
5. MATHEMATICAL MODELING 53
5.1 Introduction 53
5.2 Geometry 54
5.3 Governing equations 55
5.4 Linearization of the model 58

5.5 Reduced linearized model, no heat transfer from the bubble 60

5.6 Solution of the linear system of equations 61

6. DATA ANALYSIS AND PERFORMANCE MEASUREMENTS 62

6.1 Overview 62

6.2 Fast Fourier transformation 63

6.3 Transfer function analysis 64

6.4 Least squares method 66

6.5 Parseval's theorem 67

6.6 Performance measurements 69

6.6.1 Pressure and volume measurements 70

6.6.2 Correction of stiffness of top membrane 71

6.6.3 Temperature and entropy 72

6.6.4 Pressure-volume and temperature – entropy diagrams 73

7. EXPERIMENTAL VALIDATION OF MATHEMATICAL MODEL 76

7.1 Overview 76

7.2 Linearity test 77

7.3 Experimental validation of the model 79

7.4 Additional tests and measurements 81

7.4.1 Effect of mass of top membrane on the dynamic behavior of the engine 81

7.4.2 Effect of thermal storage on the dynamic behavior of the engine 82

7.4.3 Effect of duration of heat addition on the dynamic behavior of the engine 84

8. CYCLIC OPERATION OF THE MICRO HEAT ENGINE 87

8.1 Introduction 87

8.2 Determining resonant frequency of the engine 88

8.3 Resonant, sub-resonant, and super-resonant operation of the engine 90

9. RESONANT CYCLE OF THE MICRO HEAT ENGINE 100

9.1 Introduction 100

9.2 Resonant operation of the micro heat engine 100

9.3 Characterization of the thermodynamic cycle of the resonant micro heat engine 103

9.4 Variation of input energy delivered to the micro heat engine 108

10. CONCLUSIONS 111

BIBLIOGRAPHY 114

APPENDICES

A. SOLUTION OF THE LINEARIZED MODEL OF THE MICRO HEAT ENGINE 118

B. FFT ALGORITHM 120

C. LEAST SQUARES ALGORITHM 122

D. MODEL PRESSURE-VOLUME DIAGRAMS 130

LIST OF TABLES

1.1 Examples of waste heat sources.....4

6.1 Example of predetermined parameters used in linearized model computations.....67

7.1 Engine parameters.....77

8.1 Floating parameters used in the model 93

LIST OF FIGURES

2.1 Schematic of micro heat engine 24
2.2 Assembled micro heat engine (courtesy L. Weiss) 25
2.3 Working cycle of resonant heat engine 28
2.4 Thermal switch configuration “on “ and “off” positions 30
3.1 8mm membrane mask (backside) 36
3.2 8mm heater resistance mask (front side) 36
3.3 Fabrication of evaporator membrane 37
3.4 SU-8 wicks structure (courtesy T. Quy) 39
3.5 Fully fabricated evaporator 41
3.6 Gold targets- thermal switch 42
3.7 Micro droplet arrays 43
4.1 Experimental setup 47
4.2 Working principle of Polytec OFV-5000 laser vibrometer. 48
4.3 TTL circuit 49
4.4 Push-pull linear motion feed through 50
5.1 Engine model schematic 55
5.2 Conservation of energy in the bubble 57
6.1 Volume under top membrane 72
6.2 A representative pressure-volume diagram at resonant, f_n=110Hz 75
6.3 A representative temperature-entropy diagram at resonant, f_n=110Hz. 75
7.1 Linearity test-velocity amplitude transfer function 78
7.2 Model validation: Velocity amplitude transfer function 80

7.3 Model validation: Phase of the velocity transfer function 80
7.4 Effect of mass of top membrane on transfer function 82
7.5 Effect of thermal inertia on velocity transfer function 83
7.6 Effect of duration of heat addition process on the heat rate spectrum 85
7.7 Effect of duration of heat addition process on power output 86
8.1 Velocity transfer function of micro heat engine, f_n=110 Hz 89
8.2 Deflection of top and bottom membranes at resonance, f_o=f_n=110 Hz 90
8.3 Pressure and volume time history at resonance, f_o =f_n=110 92
8.4 PV diagram at resonance, f_o= f_n=110 Hz 92
8.5 Deflection of top and bottom membranes, f_o=90Hz 94
8.6 Pressure and volume time history at sub-resonance, f_o =90Hz 94
8.7 PV diagram at sub-resonance f_o=90 Hz 95
8.8 Deflections of top and bottom membranes at super-resonance, f_o=130Hz 96
8.9 Pressure and volume time history at super-resonance, f_o =130Hz 96
8.10 PV diagram at super-resonance, f_o =130 Hz 97
8.11 Mechanical work done by the micro engine 99
9.1 Transient versus steady state top membrane deflection f_o=130Hz 102
9.2 Bottom membrane transient deflection, f_o=130Hz 102
9.3 PV diagram at transient condition, f_o =130 Hz 103
9.4 Pressure and volume- time history at resonance, f_n=115Hz. 104
9.5-Power input to the engine and deflection of the thermal switch-time history. 105
9.6- Pressure-volume diagram at resonance, f_n =115Hz. 106
9.7- Temperature-entropy diagram at resonance, f_n =115Hz.. 106
9.8- Deflection of top membrane at different energy levels, E, f_o=f_n=83Hz 110
9.9- PV diagram at resonance, f_o = f_n =83Hz 110

Dedication

This dissertation is dedicated to the two who loved me the most:

My mother, Adela, and the soul of my father, Khalid.

Chapter 1

INTRODUCTION

1.1 Motivation and overview

Due to the increased need for portable reliable generators and miniature energy systems, considerable efforts have been focused on developing new, power-dense, miniature energy systems that out-perform the current battery technology. Because of the evolution of MEMS technology and microfabrication techniques an enormous amount of effort has been expended to use this technology to address the demand of miniature energy devices. Among those efforts is the development of micro heat engines that are characterized by high energy density. The high chemical energy density of hydrocarbon fuels, the relatively high chemical to mechanical and mechanical to electrical conversion efficiencies, and the small mass of PowerMEMS devices have appealed researchers, all over the globe, to propose the development of, power-dense, heat engines at the micro-scale size. The primary function of these heat engines is converting thermal energy into mechanical energy, which can be used directly or converted into electrical power [1]. The last two decades witnessed massive efforts to create MEMS-based heat engines that out-perform the current battery technology, and thereby provide portable power for both personal and military applications.

Different research groups have taken different approaches. Among those approaches is scaling down macro-scale dynamic heat engines, such as gas turbine engines, Stirling engines, steam engines, and Wankel engines to micro-scale size. One of the earliest miniature dynamic heat engines projects was the MIT gas turbine engine [2], followed by

the Wankel engine developed at Berkeley [3]. A few other research groups were focused on developing resonant-type miniature heat engines based on thermoacoustic engines [4], pulsejet engines [5], and reciprocating heat engines based on the Otto cycle [6]. To benefit from the increase in surface area-to-volume ratio, other groups were focused on converting thermal energy to electrical energy directly via thermoelectric materials [7]. However, development of micro-scale heat engines has proven to be a challenging task. Along the development process of such engines several obstacles and barriers came out to the surface. For instance, as Jacobson *et al.* pointed out two of the main obstacles facing the development of dynamic micro heat engines are thermal isolation and the high frequencies required to operate such engines [1]. On the one hand, high frequency operation implies high stresses on parts of the engine which, in turn limits the mechanical design and material selection. On the other hand, while high temperatures are required for the hot sections of the engine, such as the combustor, low temperatures are needed for heat rejection. As a result of this requirement thermal isolation becomes a crucial design requirement for dynamic heat engines on the micro-scale.

As a part of the efforts to develop micro-scale generators some work has been directed toward harvesting waste heat on the micro-scale. Waste heat is defined as the thermal energy that is produced by machines and industrial processes and regarded as by-product or "waste". Because waste heat is "free energy", many researchers are attracted to the idea of developing micro heat engines that operate from waste heat sources. Table 1.1 shows some examples of thermal energy by-product found in different industrial and daily life applications. Those waste heat sources maintaining high temperature gradients

are known as high quality waste heat. On the other hand, low quality waste heat sources maintain low temperature gradients.

As a rule of thumb, the larger the temperature gradient (higher quality), the higher the Carnot efficiency. That is, Carnot efficiency sets the upper limit on the performance of any waste heat recovery device. Because of that, energy harvesting of high quality waste heat has seen successful application in many real life applications such as heat wheels, heat pipes, and regenerators. On the other hand, recovering waste heat from low temperature gradient sources (low quality) has been challenging. The micro heat engine presented in this work is regarded as an external heat combustion engine with a potential to operate from low quality waste heat sources. The micro heat engine converts thermal power into mechanical power through the use of a novel thermodynamic cycle. The output power may be used either directly as mechanical power done by the engine or it may be converted into electrical power through the use of an electromechanical oscillator. The micro heat engine consists of four major components: a thermal switch to control heat addition and rejection, a bottom evaporator membrane, a top expander membrane, and an engine cavity. The cavity is filled with a two- phase mixture of working fluid. As heat is added to the engine, from an external heat source, the liquid layer evaporates. Thereby, the vapor bubble expands and pushes against the top expander membrane. Likewise, as the heat is removed from the engine, the vapor bubble shrinks because of condensation. Thereby the expander membrane flexes in. Mechanical work is produced as a result of a periodic heat addition and rejection from the engine.

Table 1.1 Examples of waste heat sources.

Application	**Temperature (^{o}C)**
Nickel refining furnace	1370-1650
Zinc refining furnace	760-1100
Steam boiler exhaust	230-480
Cooling water from welding machine	33-88
Internal combustion engine	66-120

1.2 Layout of dissertation

The first few chapters of this dissertation discuss basic issues related to the micro heat engine design and fabrication. The first chapter introduces the micro heat engine and reviews work done by other groups on other types of micro heat engines. The second chapter deals with the basic design, assembly, and operation of the resonant micro heat engine presented in this work. In the third chapter, the basic fabrication techniques used in fabricating the engine parts are discussed. The experimental setup and procedure are documented in chapter four. Mathematical modeling of the engine, data analysis and performance measurements are discussed in chapters five and six, respectively. Model validation and preliminary results of the engine operation are discussed in chapter seven. Chapters eight and nine deal with the off-resonant and resonant operation of the engine, respectively. In chapter eight, the dynamic operation of the micro heat engine at different frequencies is presented. Special attention is paid to resonant operation of the engine in chapter 9. The cycle of the micro heat engine is characterized in chapter 9. Lastly, the

conclusions of this work are presented in chapter 10. Supporting material and MATLAB codes are documented in the appendices.

1.3 Literature review

In the following sub-sections, the work done by other groups on micro heat engines is reviewed. First, the dynamic micro heat engines are reviewed, followed by resonant-type micro heat engines. The thermoelectric heat engines are discussed last.

1.3.1 Micro dynamic heat engines

Because of their success in the macro-scale, different groups have taken different approaches to build a micro-scale version of gas turbine engines operated based on the Brayton cycle [8-11]. A conventional macro-scale gas turbine generator consists of a combustor, a compressor, and a turbine that is driven by the combustion exhaust [11]. A group of researchers, at Tohoku University, investigated the feasibility of a micro-scale gas turbine generator [8-9]. In this work the group aimed at a 100W class micro-scale gas turbine. The compressor pressure ratio and temperature were set to be 3 and 1050^{o}C, respectively. The flow rate was chosen to be 2g/s. To achieve these design parameters, the group showed that the compressor should achieve 68% of its adiabatic efficiency. To achieve this efficiency the smallest diameter of the impeller should be 10 mm. In addition, the micro-combustor has to achieve self-sustained combustion, and the bearing has to stably operate at 870,000 rpm. The group carried out extensive experimental work to validate the feasibility of such design. Experimental results showed that a hydroinertia gas bearing stably ran at 891,000 rpm. A combustion efficiency as high as 99.9% was achieved. A centrifugal compressor of diameter 10 mm was shown to be able to achieve an adiabatic efficiency up to 65%. The group also concluded that a gas with the smallest

quenching distance, such as hydrogen, should be used to guarantee a self-sustained combustion. The group tested the parts of the gas turbine generator individually. The next step was to integrate those parts and build up a micro-scale gas turbine.

Another group of researchers at the Massachusetts Institute of Technology, MIT, put efforts into developing a micro-scale gas turbine engine [10-11]. The primary goal of the project was to demonstrate that a MEMS-based gas turbine was feasible. The gas turbine engine consisted of a compressor and a turbine connected by a shaft, a thin film electric induction starter-generator mounted on a shroud over the compressor blades, a rotor, bearings, and a combustion chamber. The engine was to produce tens of watts of electrical power. The size of the engine was about 20 mm. The combustor exit temperature was to be in the range of 1300-1700 K. A 500 m/s rotor tip speed, corresponding to1.2 Mrpm rotation rate, was adapted as a baseline design. A compressor with a 4:1 pressure ratio was then adapted to operate at the desired speed. A gas bearing type was selected for the baseline engine because of the relative ease of fabrication and load bearing capability. The primary fabrication techniques involved patterning a set of silicon wafers using photoresist lithography, etching, and bonding wafers together to create the enclosed passages and chambers [12]. Six silicon wafers were directly bonded together to define the desired structure of the engine. Although silicon was suitable for the compressor operation (600 K), it was not a good candidate for operation with a high combustor exit temperature (1300-1700 K). Since SiC can operate un-cooled in the range of the combustor discharge temperature (1300-1700 K), it was selected as the baseline material for engine design. However, because SiC fabrication technology was much less developed than that for Si, the individual parts of the engine were demonstrated with Si

while SiC manufacturing technology was being developed. Hydrogen was selected as the baseline engine's fuel because of its rapid mixing and chemical reaction times. Cooling air was used to thermally isolate the compressor from the combustor and turbine, and to cool the induction starter-generator.

Although the MIT gas turbine microengine was demonstrated at the component level, i.e. the turbine, bearings, and combustor were successfully fabricated, the complete integrated engine yet has not been fabricated [11]. In 2003 Epstein reported that the work was still ongoing to improve the components aerodynamic performance, thermal isolation, hydrocarbon combustors, high temperature materials (SiC), bearing system, and generators [11].

As a part of the ongoing efforts to develop a micro heat engine, a group of researchers at University of California at Berkeley proposed a rotary micro heat engine that approaches the Otto cycle in the form of a Wankel engine [3, 13-15]. The micro-rotary (Wankel) engine attracted the attention of the group as a PowerMEMS device due to its two dimensional geometry, high specific power, no complex valving design, and the minimum number of parts needed to operate the engine [13]. The ultimate goal of the project was to build two micro-rotary engines, 1 and 2.4 mm in diameter, capable of producing 10-100 mW of electrical power. To investigate the combustion issues as the engine was scaled down, the group built two "mini-rotary" Wankel engines fabricated using Electro-Discharge Machining (EDM) techniques. The two engines were 10 and 14 mm in diameter. The engine system consisted of rotor, housing, and shaft. A dynamometer/electrical motor was coupled to the engine via a steel shaft. In addition, an optical tachometer was used to measure the speed of the engine. In this preliminary

design an ignition system and a flywheel were used for testing the engine. The results showed that a 10 mm diameter Wankel engine generated 4 W of power at 9300 rpm. As the feasibility of the micro-rotary engine was demonstrated, the group moved toward the fabrication of MEMS micro-rotary engine, 1 and 2.4mm in diameter, respectively. However, as the work progressed the MEMS-based micro-rotary engine faced several fabrication obstacles. The micro-rotary engine suffered from sealing at the rotor apexes. The sealing was a crucial problem in the design of the micro-rotary engine. That is, the performance of the engine was a function of the compression ratio. In addition, the significant lateral etching and the non-uniform etching rates across the wafer were issues for the micro-rotary engine housing and rotor fabrication. In 2003, the group reported in a special issue review that "the research is centered on the fabrication of the individual components of the engine, such as rotor, housing and square shaft. The overall dimensions of these components and their interaction with each other are an important first step toward an operational generation system" [13]. As yet, the parts have not been integrated together in a MEMS-based micro-rotary engine.

C. Lee *et al.* also worked on developing a micro Wankel internal combustion engine [16-18]. To verify the design and fabrication processes needed to build the micro Wankel engine the group, as a first stage strategy, adapted the design and fabrication of a cryogenic CO_2 engine. In the second stage, combustion issues, ignition, and air and fuel mixing of the micro Wankel engine were to be investigated. First, the design study investigated the cryogenic engine and then the micro Wankel engine. A finite element analysis was carried out to verify the design process of both engines. The design study was carried out using a 15x12.2x3 mm sized engine. The engine would have a

compression ratio of 7.2 and a maximum displacement of 63.5 mm^3. A maximum indicated power output of 12 W would be achieved if operated at 17,000 rpm. SU-8 was chosen as the design material of the cryogenic engine due to its relatively good mechanical properties. Nickel was chosen for the micro Wankel engine due to its high melting temperature (1455^0C) which was sufficiently high to withstand the temperature of combustion. The results indicated that the maximum stresses and deformations on the engines components were below fracture limits and displacements clearances, respectively. Fabrication process of the cryogenic engine parts was then started using SU-8. Advanced UV-lithography processes were developed to fabricate the features of the engine. C. Lee *et al.* reported in 2004 that complete engine was under testing using liquid CO_2 and fabrication of micro Wankel engine was underway.

Using Homogenous Charge Compression Ignition (HCCI) a free piston engine that approached the Otto cycle was investigated by a group of researchers at The University of Minnesota [19-20]. As noted by the group, a common problem with micro-combustion engines was flame quenching. The group suggested that such a problem would be minimized if HCCI were used. That is, the charge would be burned without flame propagation, and external ignition system would not be necessary. Furthermore, auto-ignition would result in uniform and rapid charge consumption. That is, HCCI introduces pre-mixed fuel and air into the combustion cavity which ignites due to compression supplied by the piston, like a diesel engine cycle, yet the combustion occurs uniformly throughout the cavity like in an Otto engine. Modeling work performed by the group showed that a power output of 10 W could be achieved. In this design, the fuel

was assumed to be propane, mean piston speed 10 m/s, and mechanical efficiency of the parts 70%.

Using silicon microfabrication and MEMS technology, Frechette *et al.* proposed the development of an external micro-engine based on Rankine vapor power cycle [21-23]. The device consisted of a steam-driven turbine, generator, evaporator, and condenser. In addition, a heat source and a cooling mechanism were also needed. The working principle of the micro engine was similar to the macro Rankine vapor power cycle. The working fluid would be pressurized in the liquid state, evaporated, and then expanded through the turbine to provide mechanical power. Mechanical power would then be converted to electrical power using electrostatic or electromagnetic rotating machinery. The proposed micro engine was based on miniaturizing and integrating the Rankine device using lithography, DRIE, and wafer bonding. Frechette *et al.* proposed a planar form of the engine with dimensions of 1 cm^2x 3 mm. The predicted output electrical power, efficiency, and power density of this design were 1-12W, 1-11%, and 12kW/kg respectively. Quickly Frechette *et al.* realized the complexity and challenges toward the design and integration of the micro-engine parts. As a result, Frechette *et al.* started investigating the individual parts of the micro-engine separately. In 2004, Frechette *et al.* reported that work was in progress characterizing the thermal and rotary subsystem of the micro-engine. In this study, Frechette *et al.* was focused on the issues and challenges related to the design of micro-turbine, evaporator, and microchannels. Further work was needed to address other issues related to the micro-engine, including micro gas bearings, rotor dynamics, viscous flow, and heat transfer in the micro-engine.

Miniaturization of a Stirling engine was proposed by N. Nakajima *et al.* [24]. The Stirling engine was appealing because of the high thermal efficiency, low running noise compared to gasoline engines, and the adaptability to any heat source or type of fuel. The proposed miniature Stirling engine was a few cubic centimeters in size. The miniature Stirling engine consisted of a piston and a displacer connected together through a spring, a small magnet inside the displacer, and heating and cooling walls made of mild steel. The purpose of the spring-magnet arrangement was maintaining phase difference between piston and displacer (served as crank with flywheel mechanism). The displacer transferred gas from hot (or cold) space to cold (or hot) space and as a result the pressure of the gas decreased (increased) causing the movement of the piston (mechanical work). An engine with 0.05 cm^3 piston swept volume was realized by N. Nakajima *et al*. The output power from the engine was about 10 mW at 10 Hz when operated between hot and cooled walls temperatures of 373 K and 273 K, respectively. In 1989, N. Nakajima *et al.* reported that for application of the Stirling engine to areas like micro pumps, systems to be used inside blood vessels, and cryocoolers integrated with IC chips, further miniaturization down to the size of millimeter cubed was required. However, at that time micro-scale fabrication techniques of plastics, ceramics, and metals was not sufficiently advanced.

1.3.2 Resonant micro heat engines

Valveless Pulsejet engines with no moving parts at macro scales have been known since the early 1900. Pulsejet engines are based on the Humphery thermodynamic cycle where isobaric heat addition follows an isentropic compression and isobaric heat rejection follows an isentropic expansion [25]. Recently, there have been attempts to

fabricate MEMS-based valveless pulsejet engines. Herrault *et al.* recently built a self-resonant, MEMS-fabricated, air breathing pulsejet engine [5]. This valveless pulsejet engine converted chemical energy from fuel into oscillating thrust which may be converted into vibrational mechanical energy. The self-resonant, air breathing engine consisted of a combustion chamber with air and fuel inlets, and a resonant tailpipe. Two spark plugs, for initial ignition, were integrated with the combustion chamber. The major parts of the engine were fabricated using laser micromachining technology.

The operation of the engine starts with a single spark ignition accompanied by a mixture of air/fuel fed into the chamber. Once the air/fuel mixture is ignited the pressure rises inside the chamber, pushing exhaust gases out of inlet pipe and toward the end of exhaust pipe. After a small period of time, the pressure inside the chamber decays to below atmospheric level. As a result fresh air flows into the chamber from the air inlet and hot exhaust gases return to the chamber from the exhaust pipe. The gas mixture re-ignites and the process repeats itself. Two air-breathing engine designs were adapted. In the first generation of the air-breathing engine, the combustion chamber had a 7.5 mm diameter. The internal volume of the chamber was 0.8 cm^3. A 3.2 mm diameter resonant tailpipe was used. Hydrogen was used as the fuel source. For this specific design a pressure differential of 9 kPa was measured inside the combustion chamber. The resonant frequency of the engine was 1.38 kHz. Herrault *et al.* noted that the resonant frequency and pressure differential varied with hydrogen flow rate. The first generation of the air-breathing engine was operable in the range of hydrogen flow rate1-4 mL/min.

To obtain an accurate gas mixture, proper designs of the fuel and air inlets were adapted in the second generation of the air-breathing engine. Four inlets were located at

the periphery of the chamber, and the flow was directed toward the center of the chamber. The combustion chamber, and the resonant pipe used were the same as those used in the first generation. The functional range of operation was determined to be 1-3 mL/min. For the second generation of the air-breathing engine, both the resonant frequency and the pressure differential were unstable and varied from one pulse to another. This is presumably due to unequal mixing and ineffective mixture ratio from one pulse to another. To demonstrate the feasibility of electrical power generation, an electromagnetic generator was coupled to the oscillating thrust of the engine. An output voltage of 40 mV_{rms} peak to peak was measured across an 8Ω load at a frequency of 1.5 kHz. This voltage measurement corresponded to 2.5 μW_{rms}. No efficiency measurements were reported.

Geng *et al.* also developed a small scale valveless pulsejet engine [25]. The valveless pulsejet consisted of three parts: The inlet, the combustion chamber, and the exhaust duct. Five ports were added to allow for pressure and temperature measurements at various axial locations. A mass flow meter was used to measure the fuel flow rates. In his work Geng used both experimental and computational tools to investigate the operation of a 15 cm overall length valveless pulsejet engine. The numerical study modeled unsteady, three dimensional, compressible, viscous flow with heat transfer, combustion and radiation.

Two engine designs were adapted. Pressure, temperature, thrust, and frequency were measured. For the first engine design, the total length of the pulsejet was 22.5 cm. The mean temperature measured inside the combustion chamber was 1550 K. Chamber pressure and thrust remained in the range $\pm$0.02 MPa and $\pm$2.0 N, respectively. The

resonant frequency was measured to be 1010 Hz. In the second engine design, the total length of the pulsejet was increased to 34.3 cm. While the chamber pressure remained in the range ±0.02 MPa, thrust force decreased to ±1.2 N. The resonant frequency and mean temperature inside the chamber were 830 Hz and 1520 K, respectively. Model predictions for the same engine design were then compared to experimental data. A parametric study was then carried out to study the effect of area ratio, length, and fuel flow rate on the performance of the pulsejet engine.

Another type of resonant engine is a thermoacoustic engine. Thermoacoustic engines are basically operated in two modes, as a prime mover and as a heat pump (cooler). In a prime mover mode heat is converted into acoustic energy. Sound pumps heat up a temperature gradient in a heat pump mode. A thermoacoustic engine consists of a working fluid, a medium for thermal rectification called a stack, heat exchangers at each end of the stack, an acoustic resonator, and a loudspeaker when the engine is a heat pump or a temperature difference when it is a prime mover. Since thermoacoustic engines are usually operated at resonance, the size of the engine determines its operating frequency. A typical operating frequency of a macro thermoacoustic engine is around 500 Hz. A micro-scale thermoacoustic engine was proposed by Symko *et al.* [4]. The micro-scale thermoacoustic engine was built based on the idea of scaling down the macro size one. The operating frequency of this micro-scale thermoacoustic engine was in the rage of 4-24 kHz. In his work, Symko operated the engine in two modes, i.e. a cooler and a prime mover. As a cooler, the engine was operated at 4.5 kHz using a half-wave 4.0 cm long cylindrical resonator. The engine was operated at 1 atmosphere with air as a working gas. The engine was driven by a piezoelectric driver which was powered by an audio

amplifier hooked up to a signal generator. The driver produced a standing wave in the resonator. Heat was then pumped acoustically from the cold heat exchanger toward the hot one. Thus acoustic power was converted into heat. The temperatures of the hot and cold heat exchangers were monitored using a copper-constantan thermocouple. The sound level was also monitored by a piezoresistive pressure transducer. The measurements showed that when the driver was activated at resonance with 0.5 W electrical power, the cold heat exchanger temperature dropped by 4^{o}C. The hot heat exchanger temperature increased by 7^{o}C. Thus a temperature difference of 11^{o}C was observed when the engine was operated as a cooler. As a prime mover a ¼ wave resonator, 2 cm long was used. While the hot heat exchanger was coupled to a circuit, the cold exchanger was left at room temperature. A temperature difference was established as a result of heat flow from the circuit. Acoustic oscillation was then established as a result of the temperature difference. Thus heat was converted into acoustic power. The measurements showed that for 2W of heat input and 40^{o}C temperature difference across the stack, sound of 2 kHz was generated at an intensity of 10 mW/cm^2.

A resonant micro reciprocating engine based on the Otto cycle was proposed by Toriyama *et al.* [6, 26]. The proposed engine was composed of pistons supported by an elastic spring called "piston-spring system", a combustion chamber, a top glass plate, and an electromagnetic power generator. In this micro engine the periodic combustion pressure would resonate the piston-spring system. The piston-spring system was coupled to the electromagnetic generator so that electrical power would be generated due to electromagnetic induction at the generator. A finite element study of the resonant micro

engine was carried out by Toriyama *et al.* In this study Toriyama *et al.* investigated the working cycle of the engine, resonant modes, and stress and heat transfer inside the combustion chamber. In these computations the compression ratio was set to be 5, while the engine size was 15x10x1 mm. The results showed that the first mode resonant frequency of the elastic spring was 610 Hz. The maximum temperature inside the combustion chamber was 850 K. The maximum thermal stress was 24.3 MPa which was lower than the fracture strength of silicon. The thermal deformation along the transverse direction was 0.04 μm which was also lower than the design clearance between piston and cylinder case. Theoretical electrical power calculations showed that 40 mW was achievable under these conditions. Hydrogen was adapted as the fuel for the engine while silicon as a structural material. In 2003 Toriyama *et al.* reported that fabrication of engine's parts was started. Bulk micromachining, based on DRIE, was used to fabricate the individual parts of the engine. As a first demonstration the reciprocating motion of the piston-spring system was induced by alternation of intake and exhaust pulsed nitrogen at the combustion chamber. However, to date an actual fuel combustion and operation of the system as an engine have not been reported.

1.3.3 Thermoelectric engines

A thermoelectric generator consists of heat source, heat sink, and thermopile. The heat sink and source provide the needed energy to the thermopile to create a temperature gradient across it. The thermopile converts the thermal energy into electrical energy directly. The rate of energy conversion is directly proportional to a material property known as Seebeck coefficient, electrical conductivity, and thermal conductivity of the material. Thermoelectric generators are still heat engines and therefore bounded by the

Carnot efficiency. Conventional thermoelectric materials are PbTe and $Bi2Te_3$. Thermoelectric generators are characterized by simplicity and lack of moving parts.

Currently, there have been many efforts to fabricate MEMS-based thermoelectric generators [7, 27-31]. A group of researchers at MIT developed a thermoelectric generator with integrated catalytic combustion [7]. The thermoelectric generator directly converted heat from the catalytic combustion into electrical power. The device consisted of a channel etched through a silicon wafer and capped by a membrane and an aluminum plate to seal the channel. A thermopile extended from the center of the membrane (hot junction) to the edge (cold junction). A platinum catalyst was deposited on the channel side of the membrane and aligned with the hot end of the thermopile. The fabrication process started with patterning the backside of the wafer for later use as a KOH etch mask. Then two layers of silicon-germanium were deposited and patterned into thermopiles. The channels were etched using KOH, and the catalyst was e-beam deposited through shadow-mask. Once a mixture of fuel-air was allowed to flow through the channel toward the catalyst, the reaction took place on the catalyst and, as a result of reaction, heat was released. As a result, a temperature gradient between the thermopile junctions in the center of the membrane and silicon channel walls was created. Measurements showed that the generator was stable and operable up to $500^{o}C$, with thermopile voltage up to 7V and device thermal efficiency up to 0.02%.

A MEMS-based thermoelectric generator that uses the body temperature as the heat source was developed by V. Leonov *et al.* [28]. In this work, the group was aiming to develop a body area network consisting of a set of wireless sensors/actuators able to provide health, comfort, and safety monitoring functions of the user. V. Leonov *et al.*

developed a thermoelectric generator using poly-SiGe. The thermoelectric generator was 3x3x1cm^3 sized. The expected output power was a few microwatts. Fabrication and assembly processes, based on SiGe thermopiles, were also developed. The fabrication process consisted of several microfabrication steps including DRIE, thin film deposition, and patterning. The generator was used to transmit several measured quantities from the body to a PC with wireless module worked at 2.4 GHz.

Another group led by Norio Sato proposed the development of an integrated power generator chip that used both temperature difference and vibration as power sources [29]. The vibrational device had comb-shaped counter electrodes with one of the electrodes being movable and the other fixed. An external vibrational force would vary the capacitance between the plates, thus producing electrostatic energy. Another thermoelectric device on the chip was used to generate electrical power form a temperature difference. Thermoelectric and vibrational devices were fabricated on a silicon substrate. DRIE and electroplating of Au were used to build up the parts. Measurements showed that for a temperature difference about 75^{o}C, a maximum voltage of 2 mV was measured. The calculated Seebeck coefficient was about 0.2μV/K.

Several limitations on the design and operation of the aforementioned micro heat engines arise. For instance, most work to date has focused on demonstrating micro-scale versions of macro-scale engines, i.e. micro Rankine cycles [21], micro Otto cycles [3], and micro Brayton cycles [8]. First, as the dimensions of these engines shrink they become hard to fabricate and operate [5]. It is challenging to reproduce the complexity and three dimensionality of their macro-scale counterparts. Second, as the dimensions of these engines shrink, the operating frequency required to achieve an appreciable amount

of power increases, thus very high rotational speed is required. This implies that some parts of the micro engine will be highly stressed, adding restriction on the design process and material selection [1]. Third, friction becomes a dominant, limiting, factor in rotating and translating systems [1]. Moreover, the problem of flame quenching remains a common problem among the internal combustion cycles on the micro-scale. In addition, there are limitations on fuel type and rate used in the operation of micro pulsejet engines [5]. As noticed by Herrault *et al.* the micro pulsejet engine was operable in a certain range of fuel rate. As noted by Geng *et al.* [25] the operability of pulsejet engine is limited by chemical kinetic time of the fuel versus jet length, and inlet area to combustor area ratio. This factor becomes crucial in operation of small size pulsejet engine. That is, for small sized pulsejet engines, only fuels with short chemical times, such as hydrogen, will permit pulsejet operation. Moreover, since the pulsejet and thermoacoustic engines are resonant engines, the operating frequencies are determined by their sizes. As the dimensions of these engines are scaled down the resonant frequencies become higher. For the MEMS-based thermoacoustic and pulsejet engines [4-5] the operating frequencies were in the range 0.9-1.6 kHz and 4.0-24 kHz, respectively.

The MEMS-based resonant micro heat engine, presented in this work, overcomes most common obstacles associated with other micro-scale heat engines. First, the resonant micro heat engine is an external combustion engine that is operated from an external heat source; thereby issues related to micro-scale combustion quenching are eliminated. Second, unlike the aforementioned micro-scale heat engines, the resonant micro heat engine is built up starting from the micro-scale rather than scaling down from the macro-scale. The design is based on the stacking of 2D structures and thus eliminates

the fabrication challenge associated with complex 3D features. This is an advantageous point that eliminates the complexity and the 3D features reproducibility issues faced by other micro heat engines groups. Third, to avoid the presence of high stress components on some parts of the engine flexing components rather than rotary parts are implemented in the resonant micro heat engine. Moreover, despite the small size of this engine, compared to other micro heat engines, the resonant frequency of the engine is determined to be in the order of 100 Hz [32]. This relatively low resonant frequency of the engine has a major impact on the operation of the engine. First, the low resonant frequency of the engine makes it plausible to operate at resonance, i.e. a resonant micro heat engine. Second, lower operational frequency of the engine indicates less friction and viscous damping losses.

1.4 Objective of this work

The primary goals of this work are operating the engine at resonance, characterizing the thermodynamic cycle of the resonant micro heat engine, building a test setup that allows for better control over the experimental conditions of the engine-thermal switch configuration, and using modeling tools to understand the performance parameters of the micro heat engine.

Resonant operation of the engine is desirable. When the engine is excited at its resonant frequency, the pressure and volume changes inside the cavity are no longer coupled, thereby net mechanical work is observed. To operate the engine at resonance conditions, first the resonant frequency of the engine has to be reduced to the order of 100Hz where the thermal switch can operate effectively, and effective heat addition/removal would take place.

Characterization of the cycle of the micro heat engine is crucial to evaluate the performance of the engine and compare it to other thermodynamic cycles. To achieve that several steps need to be taken. The engine should be operated at resonance and the thermodynamic state of the vapor inside the cavity should be determined. The thermodynamic cycle of the engine is determined by constructing the pressure-volume and temperature-entropy diagrams.

The integration of the thermal switch with the engine has a major impact on the performance of the engine, as will be further discussed in section 2.4. To improve the micro heat engine operation a well-controlled experimental setup is to be built. As will be discussed in chapter 4, the main requirement of this setup is having better control over the environmental conditions of the experiments. For example, the thermal resistance

ratio R_{off}/R_{on} is improved when the thermal switch is operated in a low thermal conductivity gas environment, such as argon or xenon. The new experimental setup is built in a way that thermal switch-engine environment is well-controlled.

The last goal of this work is to use modeling tools to understand the parameters which determine performance of the micro heat engine. To do that a lumped parameter model of the engine is developed and validated against measured data.

Chapter 2

INTRODUCTION TO MICRO HEAT ENGINE

2.1 Introduction

This chapter deals with the micro heat engine operation. First, the micro heat engine is introduced. Fabrication and assembly of the major parts of the engine are discussed. Next, the working principle of the engine is presented. The thermal switch working principle and fabrication are introduced last.

2.2 Micro heat engine

The micro heat engine consists of a cavity, evaporator, expander, and thermal switch [33]. The cavity is filled with a two-phase fluid bounded by top (expander) and bottom (evaporator) membranes. The two membranes are separated by a thin gasket layer (semiconductor tape) that forms the cavity. On the bottom membrane are a resistance heater and wick structures. The capillary wick maintains a layer of liquid-phase working fluid on the bottom membrane and improves the evaporation process as a result. A thermal switch is used to add/remove the heat from the engine. The micro heat engine is shown in Figure 2.1.

The top membrane bounding the engine cavity is fabricated from a 3 inch diameter double-sided polished silicon wafer. A thin layer of silicon nitride is deposited on the wafer using a Low Pressure Chemical Vapor Deposition (LPCVD) process. The back side of the wafer is patterned into silicon nitride window membranes using a standard contact photolithography process. Deep Reactive Ion Etching (DRIE) is then used to etch the nitride layer followed by KOH wet-etching to define the silicon nitride membranes.

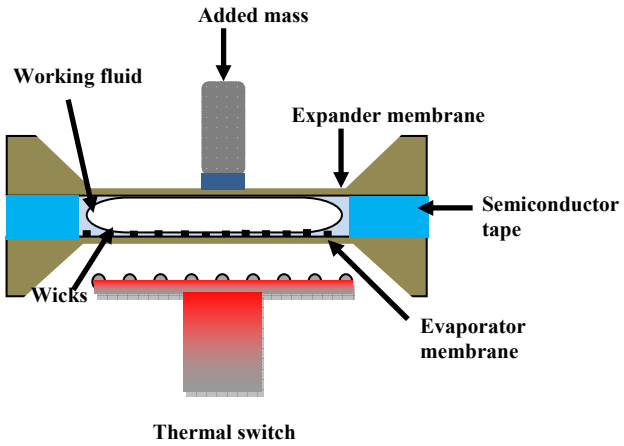

Figure 2.1: Schematic of micro heat engine.

The bottom membrane is also made of a 3 inch diameter silicon wafer. A 5nm adhesion layer of Ti/W followed by 300 and 500 nm gold layers are sputtered on the front and back side of the wafer, respectively. Both sides of the wafer are then patterned using a contact photolithography process. A resistance heater is patterned on the front side. The back side is patterned into silicon window membranes. Next, an SU-8 layer is spun and then patterned into wick structures on top of the resistance heater, using a standard photolithography process. The wick micro structure takes the shape of a rectangular wall, radially patterned toward the center of the membrane.

To assemble the engine, first the bottom membrane is fixed on a carrier plate. Next, layers of semi-conductor tape are bonded to the bottom membrane die to form the cavity walls. Each layer is approximately 75μm thick. The number of layers separating the two membranes determines the size of the cavity. The side length of each layer is the same as the side length of the top membrane. A heat sink compound may be used between the layers to ensure good sealing. Then the two-phase mixture of working fluid is injected into the cavity. The top membrane is then clamped on top of the cavity. During this

process, a vapor bubble is formed in the center of the engine and a liquid annulus surrounds the bubble. Carefully an upper carrier is then screwed to the lower one and the plates are tightened good enough to seal the engine. If the carriers are tightened too much the engine might crack. On the other hand, insufficient tightening might cause the engine to leak. Figure 2.2 shows an assembled engine in carrier plates. The engine is then placed on the test stand and ready for operation.

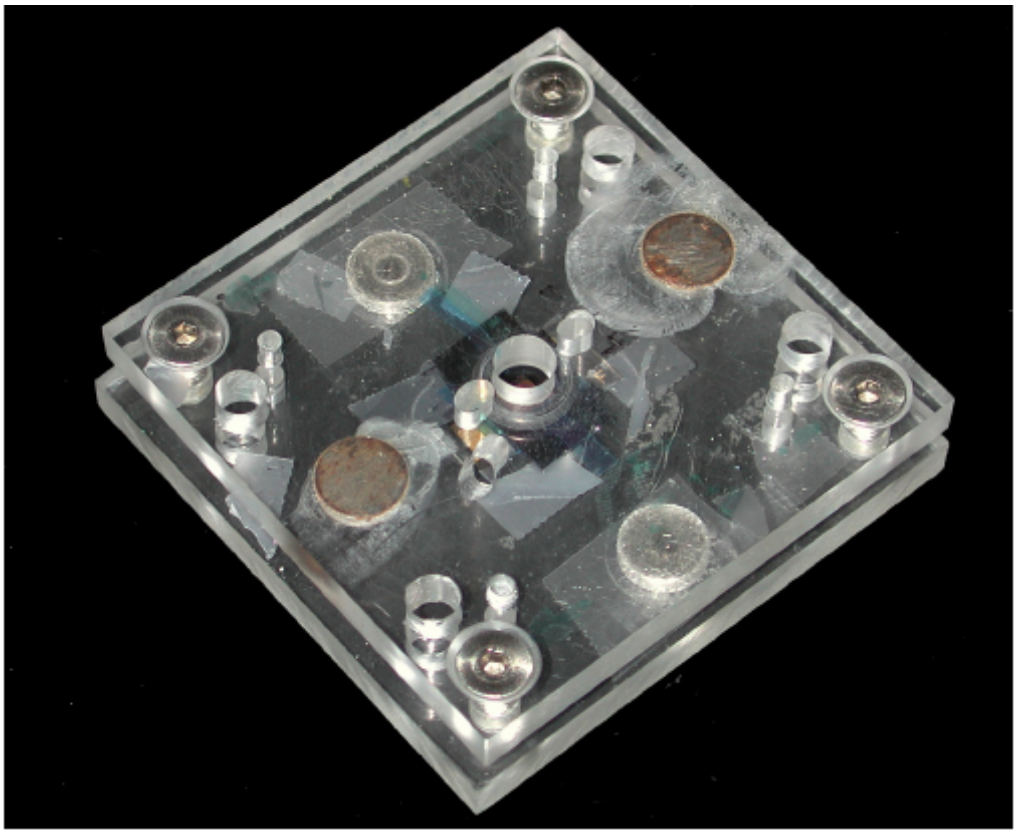

Figure 2.2: Assembled micro heat engine (courtesy L. Weiss).

To reduce the resonant frequency of the engine, to the order of 100Hz, a concentric mass is placed on top of the engine. Care must be taken when placing the "added mass"

on top of the engine. That is, the top membrane is very fragile and sensitive to point forces. To avoid shattering the top membrane, and to reduce thermal mass of the "added mass" a low thermal conductivity piece of plastic is used to separate the "added mass" from the engine. The "added mass" is first glued to the plastic piece and then placed on top of the engine using pairs of tweezers.

2.3 Micro heat engine operation

The operation of the micro heat engine is classified either as a resonant operation or off-resonant operation. When the micro heat engine is excited at resonant frequency, the operation is called resonant operation. For an off-resonant operation, the micro heat engine is excited at frequencies other than resonant frequency. Both operating modes involve heat addition and heat rejection processes. However, the response of the micro heat engine differs from one operation mode to another.

A schematic diagram of the cycle operation of the micro heat engine is shown in Figure 2.3. Once heat is applied through the bottom membrane (evaporator), it evaporates the layer of liquid working fluid held in the wicks. The evaporated mass enlarges the bubble, causing an increase in pressure inside the cavity. The resultant increase in pressure inside the cavity causes the top membrane (expander) to flex outward, thereby the volume of the cavity increases. In a similar manner, when heat is removed from the engine vapor condenses into liquid. The bubble shrinks down, causing the pressure inside the cavity to decrease. Thus the top membrane (expander) flexes in and the volume of the cavity decreases. Periodic heat addition/removal results in cyclic operation of the engine.

When operated at resonance volume and pressure changes inside the cavity are phase lagged. For a resonant operation, pressure changes are decoupled from volume changes. Thereby, mechanical power is produced as the top membrane (expander) alternately expands and compresses the working fluid. By contrast, far away from resonant once the heat is added, through the bottom membrane (evaporator), evaporation of working fluid is followed by simultaneous pressure and volume increase of the cavity. Thus, the pressure and volume rise and fall together, thereby no mechanical work is done by the engine for this condition of operation.

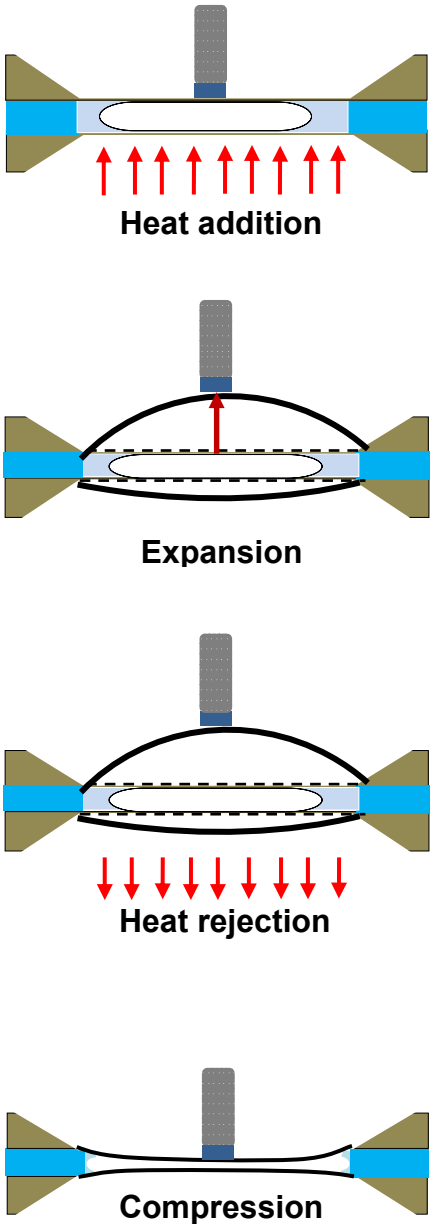

Figure 2.3: Working cycle of resonant heat engine.

2.4 Thermal switch

One of the major factors that determine the performance of the micro heat engine is the performance of the thermal switch. The thermal switch is responsible for two essential events in the cycle of the micro heat engine; adding heat and removing it [34]. The thermal switch consists of liquid-metal micro-droplet arrays deposited on a silicon die. The silicon die is bonded to a heat exchanger that maintains the thermal switch at a constant temperature (high temperature/low temperature reservoir). When the micro-droplet arrays contact the bottom membrane, heat is transferred from/to the thermal switch to/from the engine. Improving the actions of heat addition and removal would directly be reflected on the cycle of the engine. Because of that, assessment of the thermal switch performance is crucial for the engine operation.

The liquid-metal micro-droplet arrays making the thermal switch are fabricated by preferentially condensing mercury vapor on gold targets [35]. When the liquid-metal micro-droplet arrays make contact with the engine, the thermal switch is in its "on" position and heat is transferred between the micro-droplets and the engine. Likewise, when the micro-droplet arrays break contact with the engine, the thermal switch is in its "off" position and heat is transferred across the gas filling the gap between the micro-droplets and the engine. In both cases, i.e. "on" and "off" positions, heat is transferred by conduction. Figure 2.4 shows both the "on" and "off" positions of thermal switch.

The figure of merit for performance of the thermal switch is the ratio of the thermal resistance in the "off" and "on" positions, i.e. R_{off}/R_{on}, [36]. As a rule of thumb, the thermal switch is to be built such that a high R_{off}/R_{on} is achieved. A high thermal resistance in the "off" position, i.e. R_{off} is required so that the switch does not "leak" heat

to the surrounding. However, a low thermal resistance in the "on" position is desired so that heat transfer between the engine and thermal switch is maximized.

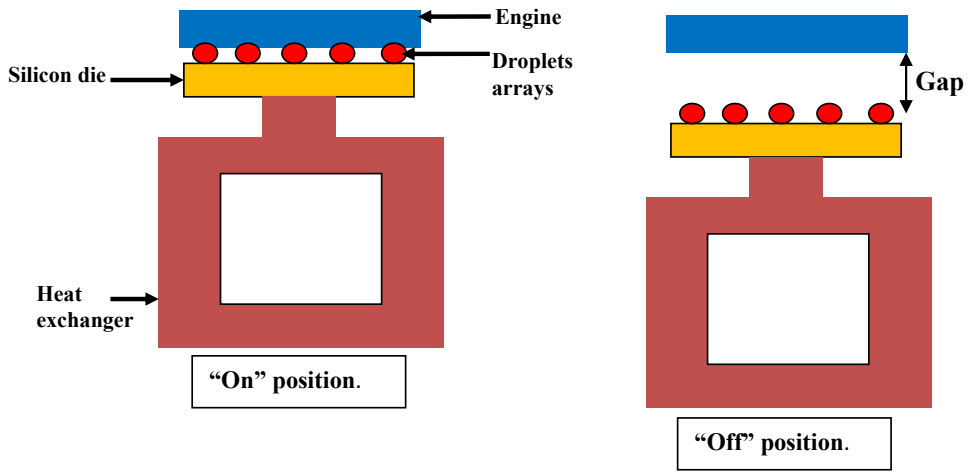

Figure 2.4: Thermal switch configuration "on" and "off" positions.

The thermal resistances R_{on} and R_{off} are determined by the thermal properties of the contact surfaces and the gas filling the gap, respectively. With the micro-droplet arrays, the high compliance of the droplets guarantees a good contact, thus lower thermal resistance when thermal switch is in "on" position. However, in the "off" position the thermal resistance, i.e. R_{off}, is determined by thermal properties of the gas filling the gap between thermal switch and engine. The thermal resistance of the gas layer, at ambient pressure, is given by $R_g=L/k*A$, where L is the gap thickness (also known as travel distance of thermal switch), k is thermal conductivity of the gas filling the gap, and A is the cross-sectional area of the gas layer. To reduce heat conduction through the gap in the "off" position, low thermal conductivity gas, small cross sectional area, and large gap thickness are required. However, the cross-sectional area of the gas layer is limited by

the specific geometry of the lower boundary of the engine. Also, the gap thickness (travel distance) between thermal switch and engine is constrained by the capabilities, such as speed and response time, of the actuator that moves the thermal switch up and down during the operation of the engine. Thus filling the gap with a low thermal conductivity gas, such as xenon or argon, is a direct way to achieve high R_{off}. Another factor that affects the heat transfer events in the "off position" is the pressure of the gas filling the gap. To reduce heat conduction, the pressure of the gas is to be reduced until the mean free molecular path length of the gas exceeds the gap thickness.

In the work presented here, due to experimental limitations and complexity, only one thermal switch is used at any given time. That is, the thermal switch is used to control heat transfer either to or from the engine. When the thermal switch is used to control heat addition, heat rejection occurs by passive conduction to the surroundings [37]. When the thermal switch is used to control heat rejection, heat addition occurs via a resistance heater [37]. In the work documented here heat was added to the engine through a gold resistance heater that was fabricated on the bottom membrane. The use of a resistance heater enabled precise control of the magnitude and duration of the heat addition process. This level of precision of control was required to effectively resolve the spectral behavior of the micro engine using the transfer function approach (section 6.3). Heat was removed from the engine via the thermal switch (low temperature reservoir).

Chapter 3

FABRICATION OF MICRO HEAT ENGINE AND THERMAL SWITCH

3.1 Overview

The micro heat engine components and the thermal switch are constructed using the microfabrication techniques of MEMS technology. All fabrication processes commence with a silicon substrate. The standard silicon wafer used to build up the parts is 3 inch diameter <100> wafer. The average thickness of a silicon wafer is 400 ± 25μm [38-39]. The major microfabrication techniques used in this work include thin film deposition, photolithography, and etching. Those techniques are employed to make the major parts of the engine, namely: top membrane (expander), bottom membrane (evaporator), thermal switch, and wick structure. However, the specific function of each part requires the development of specific recipe for each individual part. In the following sections, detailed descriptions of the fabrication techniques of the individual parts of the engine and thermal switch are discussed in details. All microfabrication processes are performed in the clean room facility at Washington State University.

3.2 Silicon wafer preparation

The preparation of the silicon wafer includes several major steps. First the wafer is placed in a furnace at 1050^{o}C for 120min to grow 500nm thick oxide layers on both front and backside of the wafer. To speed up the High Temperature Oxidation process (HTO), wet oxidation is used [40]. Next, the backside of the wafer is masked, with a semiconductor tape, and the wafer is submersed in Buffered Oxide Etch (BOE) for 15 min. This step is important to remove the oxide layer on the front side of the wafer and prepares it for boron diffusion. Once the oxide layer is removed from the front side, the

wafer is placed in a furnace such that the front side is facing a boron disk. Boron is then diffused at 1125^{o}C for 110min. After 110min a layer of boron is grown on the front side of the wafer. The layer of boron provides an etch stop for wet etching processes used later in the fabrication of micro heat engine components. Boron doping slows down the etch rate of the anisotropic etching process by factor of 50 if the concentration of the boron is more than $5 \times 10^{19} cm^{-3}$ [41]. This is important to define the thickness of the membrane when etched. Subsequent minor steps are carried out to remove the borosilicate glass layer formed as a result of boron doping. Removal of this film includes full immersion of the wafer in BOE for 15min. The BOE step is followed by growing Low Temperature Oxide (LTO) layer on both sides of the wafer. This step includes placing the wafer in the furnace, while oxygen and water vapor flows into the chamber of the furnace, at 850^{o}C for 60min. Lastly, a second BOE immersion of the wafer is carried out for 10 min.

3.3 Fabrication of bottom membrane (evaporator)

Several microfabrication steps are involved in making bottom membranes (evaporator) including gold sputtering, spinning, patterning, photolithography, and Buffered Oxide Etch (BOE) and Potassium-Hydroxide (KOH) etching. In this work, the side length of each squared bottom membrane is 8mm. The bottom membrane is 2.2μm thick. To fabricate the bottom membrane (evaporator), we start with a standard substrate wafer described in section 3.2. First, a 5nm adhesion layer of Ti/W is deposited on the silicon wafer followed by 300 and 500nm gold layers deposited on the front and backside of the wafer, respectively. Next, HMDS solution and AZ5214-EIR photoresist are, respectively, spun on the front side of the wafer at 3000rpm for 30sec. After spinning,

the wafer is baked on a hot plate at 110^{o}C for 1min. The spinning and baking processes are then repeated for the backside of the wafer. At this point, both sides of the wafer are covered with photoresist. It is important to keep the photoresist, patterned or un-patterned, on both sides of the wafer until all gold processing steps are completed. That is the photoresist protects the removal of deposited gold during the subsequent fabrication steps. The un-patterned part of the gold layer on the back side of the wafer serves as an etch mask during the wet etching process. Next, the backside of the wafer is patterned using an 8mm oxide mask, shown in Figure 3.1. To achieve the desired pattern, the wafer is exposed to UV light for 12sec. Then, the wafer is fully immersed in a 1:4 solution of AZ400K developer and DI water. To completely pattern the photoresist, the wafer is agitated in the solution for 45sec. Once the photoresist is patterned, the wafer is immersed into gold etchant for approximately 2min, followed by 40sec full immersion in 35% hydrogen peroxide solution with strong agitation. To completely remove the exposed oxide layer on the backside, the wafer is immersed in BOE for 10min. At this point, the backside of the wafer is patterned into silicon windows and ready for KOH.

Next, the front side of the wafer is patterned using the same procedure. The front side is patterned, with the desired mask, into electrical heaters. The patterned heaters facilitate heat transfer into the engine electrically. The photoresist is developed using the same manner described above, the gold and Ti/W are, also, etched consequently in the same aforementioned manner. When patterning the heaters on the front side, it should be made sure that the front side patterns are accurately aligned with the backside window patterns. This way, the silicon windows are precisely located underneath the electrical heaters. Figure 3.2 shows 8mm resistance heaters mask. The combination of the electrical heater

and silicon window forms the bottom evaporator membrane. Next, the patterned gold is annealed at 650^{o}C for 10min. Figure 3.3 shows the major steps in the fabrication of an evaporator membrane. Before the wafer is etched in KOH, wick micro channels are fabricated on top of the electrical heaters. The description of wick fabrication is discussed next.

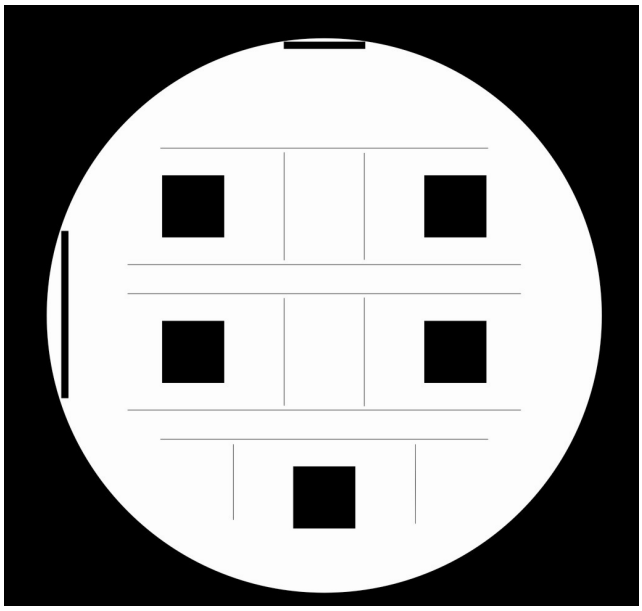

Figure 3.1: 8mm membrane mask (backside)

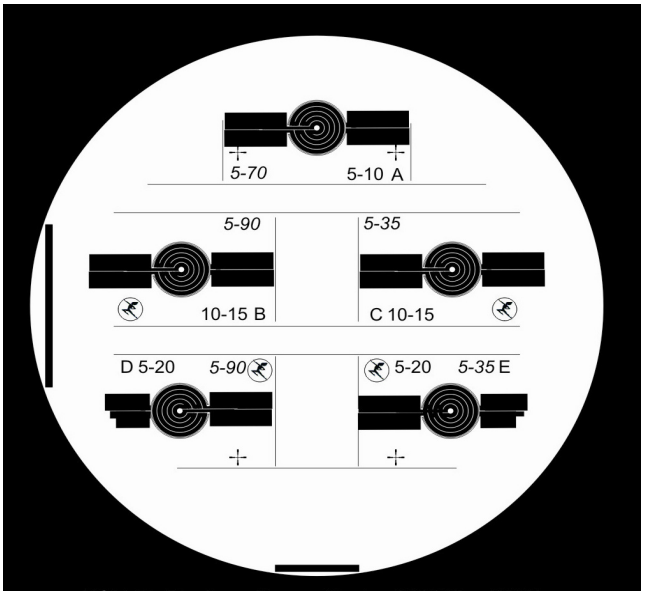

Figure 3.2: 8mm heater resistance mask (front side)

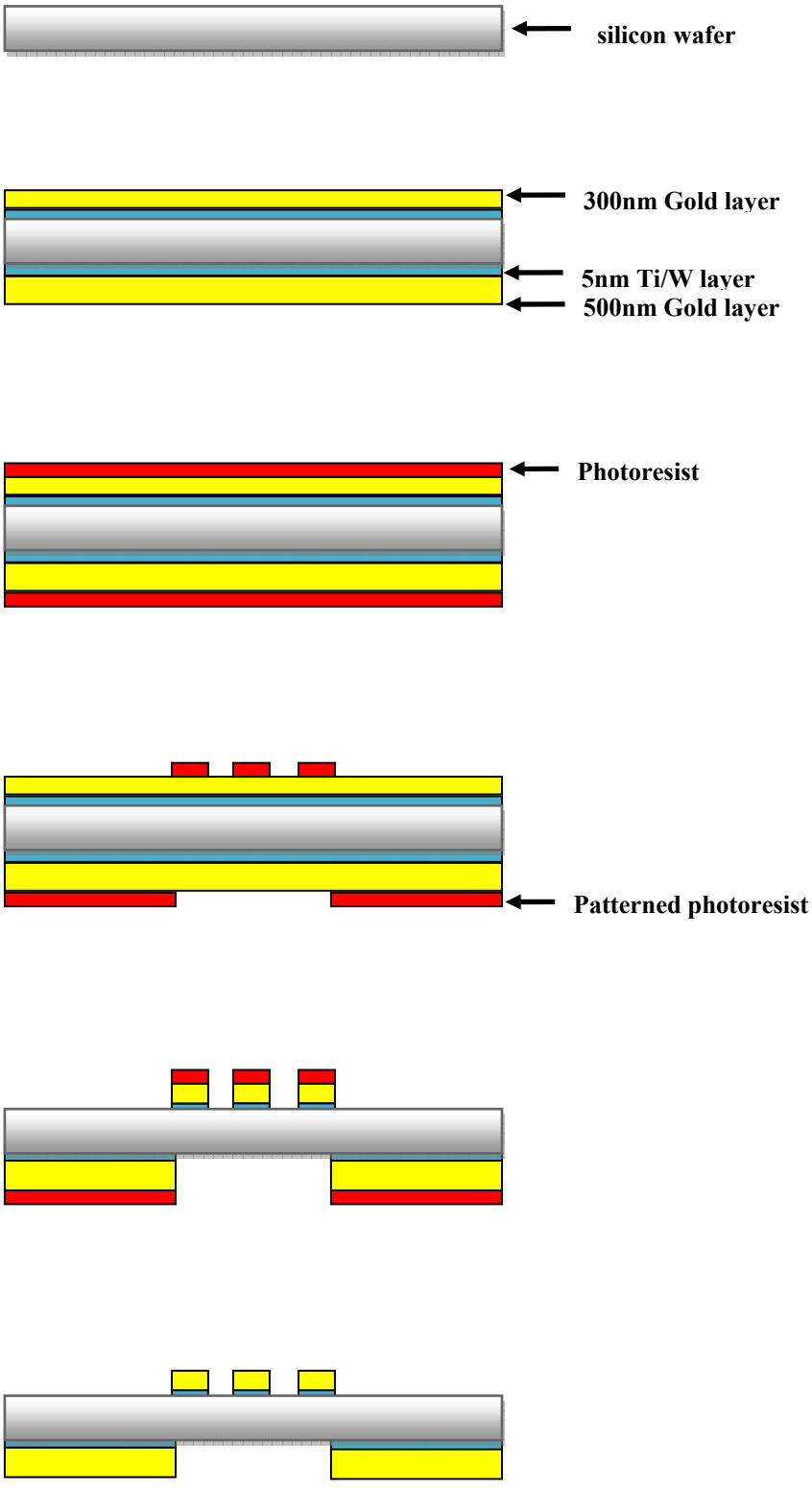

Figure 3.3: Fabrication of evaporator membrane.

3.4 Fabrication of wick micro channels

The primary goal of the wick structure is maintaining a thin layer of liquid atop above the electrical heater, i.e. point where heat is added to guarantee the evaporation process during the operation of the engine. The wicks are fabricated using SU-8 polymer. The SU-8 polymer is characterized by its ability to withstand high temperatures, and capability of forming high aspect ratio structures up to 14:1 [40]. The wicks are radially patterned toward the center of the heater. The wick walls are 5μm thick and 90μm apart.

To fabricate 10μm high wicks, Omnicoat is spun on top of the patterned heaters at 3000rpm for 30 sec. Following the spinning, the wafer is baked at 200^{o}C for 1 min and then allowed to cool down to room temperature. Next, SU-8 2010 is spun at 2000rpm for 30 sec. The wafer is then baked at 65^{o}C and 95^{o}C for 1min and 2min, respectively. The wafer is then exposed to UV light for 15 sec, followed by post exposure baking for 2min at 65^{o}C and 95^{o}C and then again for 1min at 65^{o}C. After letting wafer cooling down to room temperature, the wafer is developed in SU-8 developer for 3min with constant strong agitation.

The Fabrication procedure of 40μm high wicks is a little different. After spinning and baking the Omnicoat layers, SU-8 2025 is spun on top of the wafer at 500rpm for 7sec with acceleration about 100rpm/s. Next, the wafer is spun for another 30sec at 2000rpm with acceleration of 300rpm/s. The wafer is then baked for 2 ½ min at 65^{o}C, followed by 1 hour in convection oven at 95^{o}C. Next, the wafer is exposed to UV light for 55sec, followed by post exposure baking at 65^{o}C and 95^{o}C for 1min and 4min, respectively. After letting wafer cooling down to room temperature, the wafer is fully immersed in SU-8 developer for 5 ½ min with strong agitation. At this point, the heater resistances,

silicon windows, and wicks are all patterned and developed. The final process before using the evaporator membranes is wet etching in KOH solution. More Details on SU-8 and wick fabrication are found in [42]. Figure 3.4 shows a 40μm high wick structure.

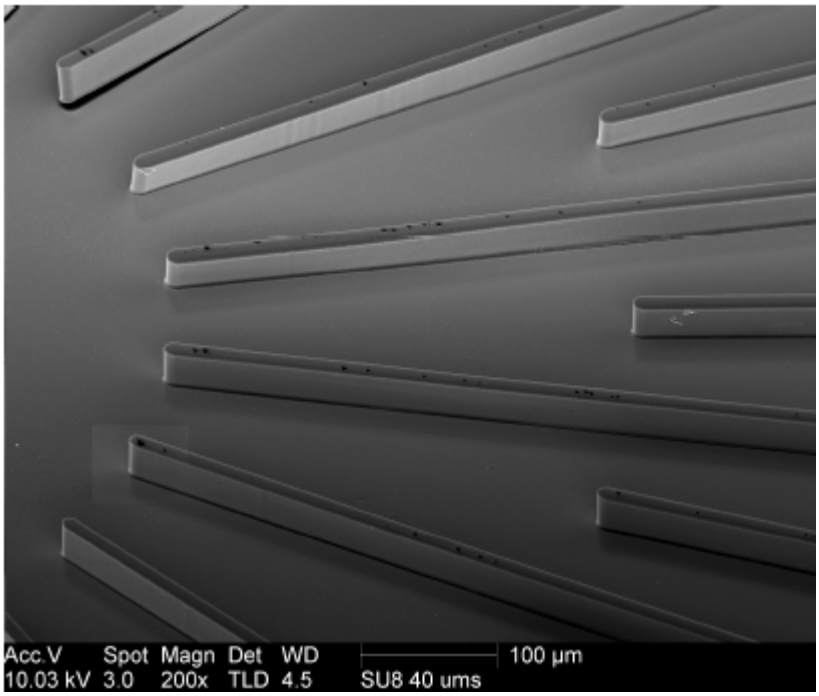

Figure 3.4: SU-8 wicks structure (Courtesy T. Quy).

3.5 Fabrication of top membrane (expander)

The fabrication of silicon nitride membranes starts with depositing a 300nm layer of silicon nitride on both sides of a double polished <100> wafer using Low Pressure Chemical Vapor Deposition (LPCVD) technique [40]. Photoresist is then spun on the backside of the wafer and patterned in the same procedure detailed in section 3.3. Once the photoresist is patterned, the backside of the wafer is etched using Deep Reactive Ion Etching (DRIE) technique. The backside is etched until the bare silicon is exposed as

defined by the photoresist pattern, making the etching time approximately 2min. Lastly, the patterned silicon nitride wafer is etched in KOH to define the micro structure of the membranes. The obtained membranes are approximately 300nm thick.

3.6 KOH etching

The last step to completely define the shape of the bottom membranes (evaporators) and top membranes (expanders) is Potassium Hydroxide etching (KOH). KOH etching is an anisotropic wet etching technique. To prepare the KOH mixture, 250g of KOH dry pellets are mixed with 400ml of DI water. The mixture is then heated up to 75-80^{o}C. The wafer is then placed in a holder and fully immersed into the KOH mixture for 6-8 hours. When etching the bottom membranes (evaporators), the gold layer on the backside of the silicon wafer serves as an etch mask against KOH. That is KOH will only etch the uncovered area of silicon. When etching top membranes (expanders), the unexposed silicon nitride layer on the backside of the wafer serves as an etch mask against KOH. Figure 3.5 shows a fully etched 8mm silicon bottom membrane (evaporator) with electrical resistance and wicks micro-channels on top of it.

3.7 Fabrication of thermal switch

The fabrication of liquid-metal droplet arrays requires the deposition of mercury vapor on gold targets patterned on silicon die. The mercury vapor condenses preferentially on gold targets to form amalgam [43]. The fabrication process starts with a basic silicon substrate. First, a 5nm layer of Ti/W followed by 300nm layer of gold is sputtered on the front side of the wafer. Then, the front side is patterned to create 30μm diameter gold targets using the standard photolithography technique described in section 3.3. The gold pattern is then annealed at 650^{o}C for 10 min. Next, photoresist is spun on

the gold targets and patterned such that small holes in the photoresist are opened around the gold targets. This way, mercury is only deposited on gold targets, resulting in liquid-metal droplet arrays. Figure 3.6 shows the photoresist pattern around gold targets before mercury deposition takes place. Next, the wafer is diced into the desired thermal switch die size. The rest of fabrication steps is carried on the die level.

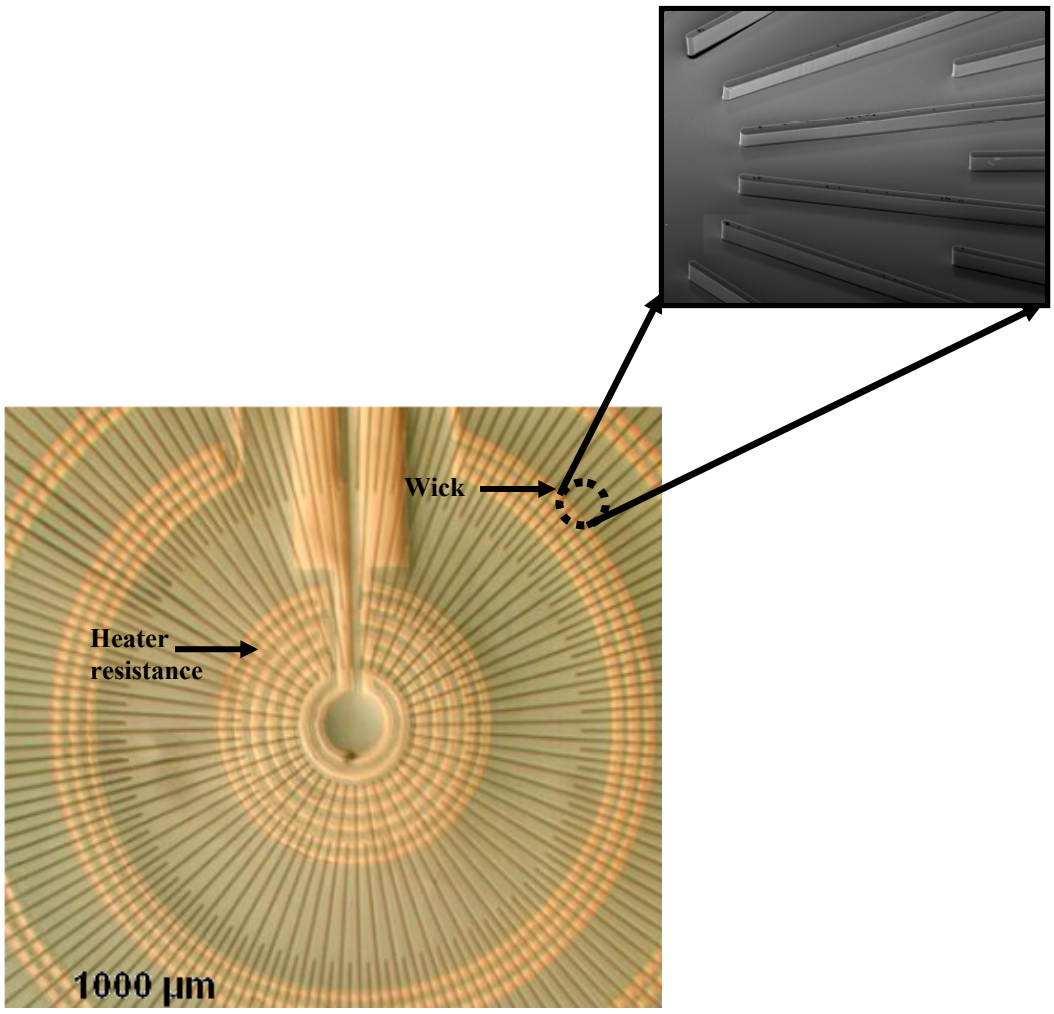

Figure 3.5: Fully fabricated evaporator

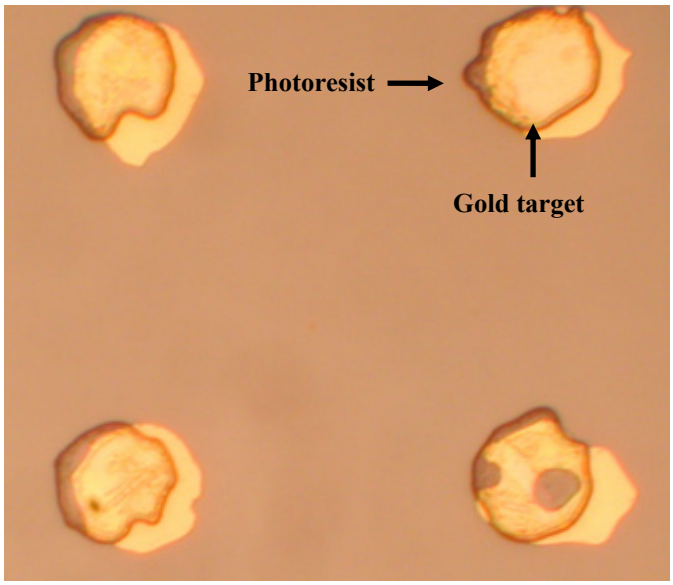

Figure 3.6: Gold targets-thermal switch

To successfully deposit mercury vapor on gold targets, the die is exposed to mercury vapor in a deposition chamber at temperature 180-190^{o}C. The size of mercury droplets depends on the total exposure time. For an average of 30μm diameter mercury droplets, the mercury vapor allowed to condense on the gold targets for 2 ¼ hours. A fully fabricated thermal switch is shown in Figure 3.7. Detailed description of thermal switch fabrication is found in [44].

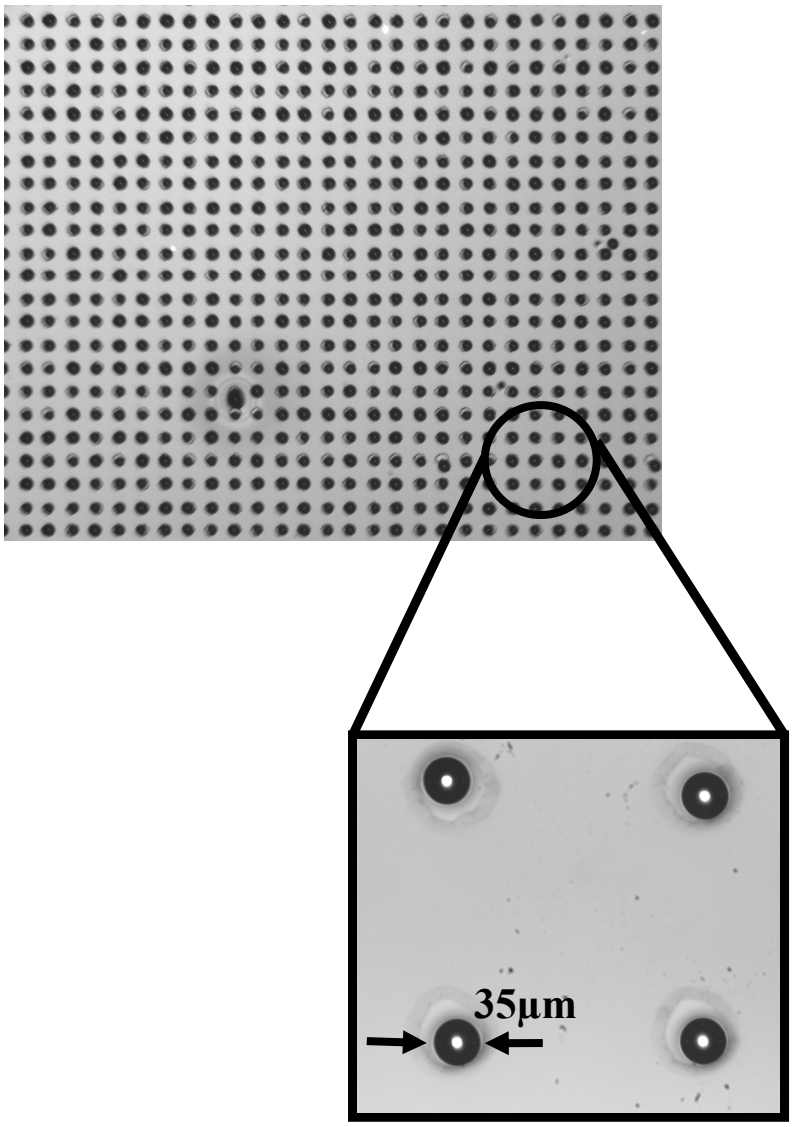

Figure 3.7: Micro droplet arrays.

Chapter 4

EXPERIMENTAL SETUP AND PROCEDURE

4.1 Introduction

Building up a robust experimental setup that can be used to investigate the dynamic and thermal behavior of the micro heat engine is identified as a primary objective of this work. One of the main requirements of this experimental setup is improving the thermal switch-engine integration. For instance, to reduce heat leakage from the engine, when the thermal switch is in the "off" position, the gap between the thermal switch and the engine is filled with a low thermal conductivity gas. Also, improving the alignment between the thermal switch and the engine would guarantee a good contact. A good contact would improve heat transfer between the thermal switch and the engine in the "on" position. In addition, the vibration transmitted from the thermal switch to the engine should be reduced. Such vibration may result from the motion of the thermal switch during the operation of the engine. In this chapter, the experimental setup used to operate the engine is presented. The experimental procedure followed to operate the engine at resonance and off-resonance is then documented.

4. 2 Experimental setup

Figure 4.1 illustrates the experimental apparatus used to characterize the dynamic behavior of the micro heat engine. The engine is mounted on top of an acrylic chamber. The acrylic chamber (ID= $4.0^{"}$, OD= $4.5^{"}$) is transparent to allow optical access. The chamber also provides a seal to maintain a rough vacuum. The ability of the acrylic chamber to seal against vacuum provides flexibility in the operating conditions. That is, the air inside the chamber may be replaced with a gas with low thermal conductivity. A

low thermal conductivity gas, such as argon or xenon, helps reduce heat leakage from the engine to the surroundings during the "off" state [36].

A Labview program is used to control the timing and frequency of heat addition to the engine, through a resistance heater, and the motion of the thermal switch. The Labview program is used to deliver two signals, a square wave at predetermined frequency to the resistance heater, and a modified sine wave that controls the motion of the thermal switch. Based on these signals, the resistance heater is activated via a TTL circuit. The TTL circuit requires a voltage of 4.5V from Labview to initiate an electrical pulse to the bottom evaporator membrane. A power supply is used to control the amount of electrical power delivered to the resistance heater. Figure 4.1, also, shows the connection from the Labview interface board to the piezo-amplifier. The amplifier is a combined PI-501 and PI-505 model that provides a 10x amplification of the incoming modified sine wave before sending it to a piezo-stack actuator. The piezo-stack actuator moves a micro heat exchanger, back and forth, thereby making and breaking contact between the thermal switch and the engine. A push-pull device is used to linearly transmit the motion of the piezo-stack actuator through the chamber to the micro heat exchanger. Because of the physical contact between the push-pull device and the chamber, vibration is transmitted into the engine. To eliminate the vibration transmitted to the engine a stainless steel edge welded bellows are used. A two 9.00" ASA flanges are welded to the ends of the bellows to ensure sealing against vacuum.

To guarantee a better alignment between the thermal switch and the engine, four vertical translation stages are used. At each edge of the chamber, a vertical transition stage is placed. The resolution of each stage is 3μm. A stainless steel shutter is used to

open/close the gap underneath the engine. When the shutter is opened the thermal switch gains access to the engine and the operation of the engine can be carried out. When the shutter is closed the whole chamber is now sealed and the thermal switch is completely isolated from the engine, thereby the initially air-filled chamber can be evacuated and refilled with low thermal conductivity gas. A pressure gauge is used to monitor the pressure inside the chamber.

In Figure 4.1 is also shown the laser vibrometer that is used to measure the displacement of both top and bottom membranes. Both displacements of the top and bottom membranes are sampled with a digital oscilloscope (Tektronix TDS5034B) and stored on a personal computer for later analysis. Details on the individual parts and equipments used to build up the experimental setup are documented in the next few sub-sections.

4.2.1 Laser vibrometer

Membrane deflections are measured with a Polytec OFV-5000 laser vibrometer with DD-200 displacement decoding software. The operating principle of the laser vibrometer is based on the Doppler shift of the laser light being reflected off the object. A helium neon laser beam is directed at the vibrating object and reflected back from it. The phase $\Delta\varnothing$ and frequency Δf information of the reflected beam are then recovered in signal processing unit using velocity and displacement decoders. The displacement signal is reconstructed from the phase information $\Delta\varnothing$ while the velocity is recovered from the frequency information Δf. Figure 4.2 shows the working principle of Polytec OFV-5000 laser vibrometer.

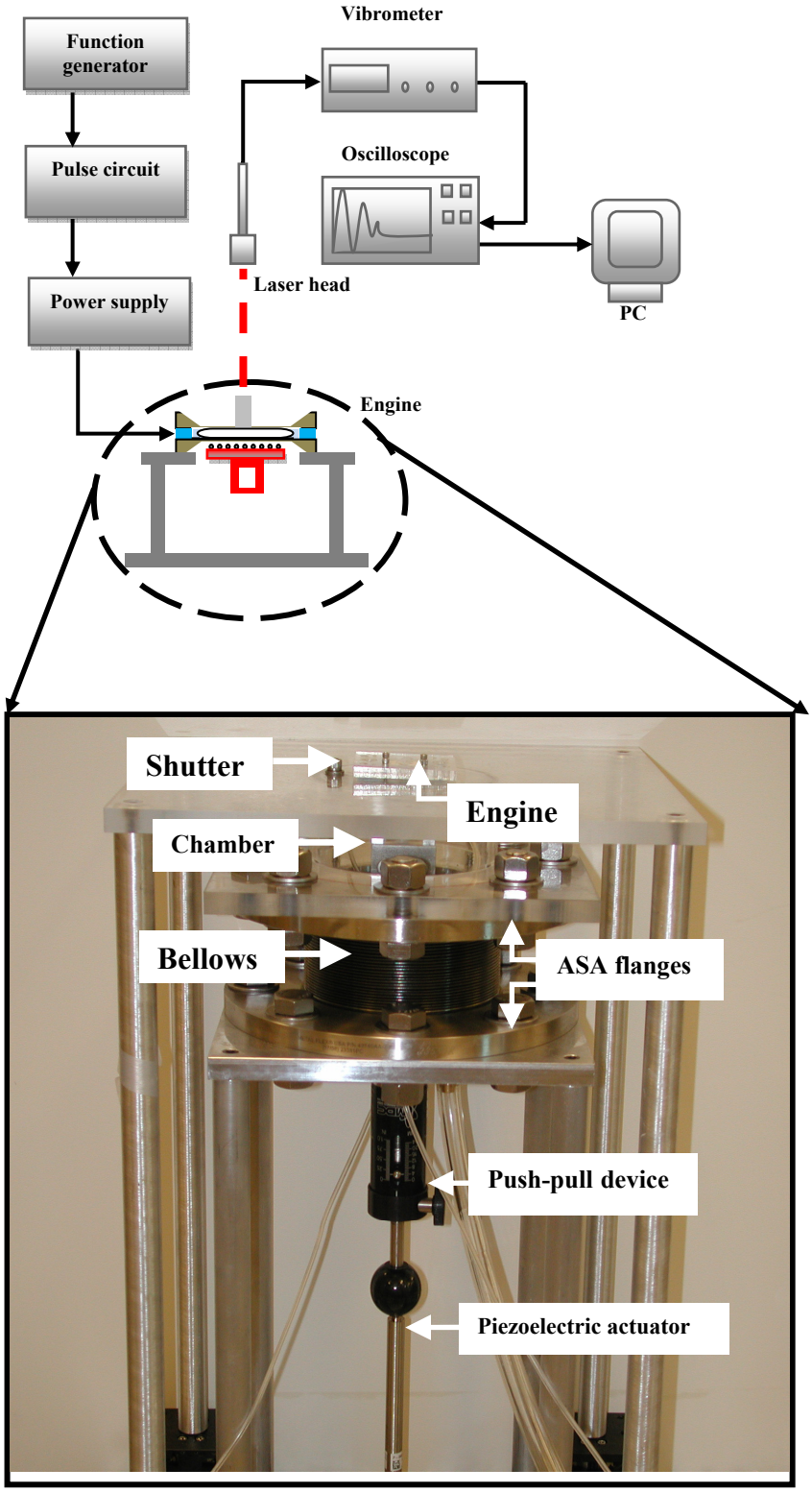

Figure 4.1: Experimental setup.

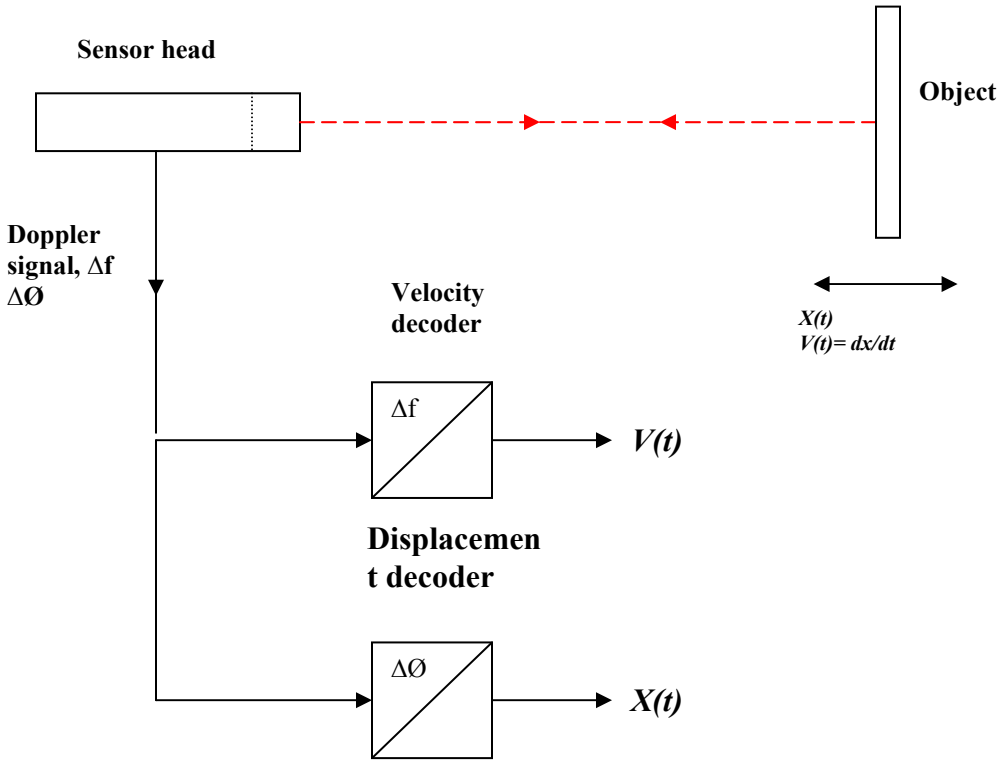

Figure 4.2: Working principle of Polytec OFV-5000 laser vibrometer.

4.2.2 TTL circuit

The Transistor-Transistor Logic (TTL) circuit provides a square wave to the resistance heater. The amount of electrical power delivered to the resistance heater is then controlled by varying the voltage amplitude of the power supply attached to the TTL circuit. A schematic diagram of the TTL circuit is shown in Figure 4.3. Detailed description of the TTL circuit is found in [39].

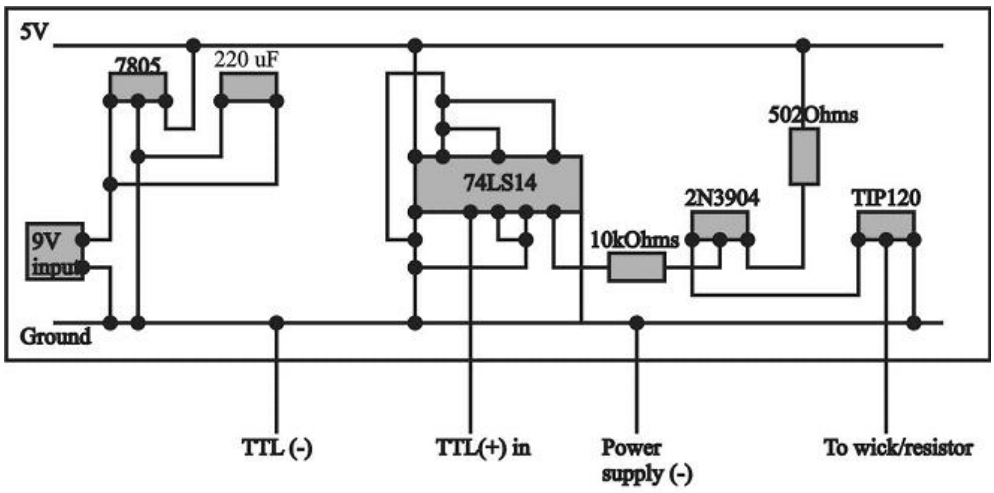

Figure 4.3: TTL circuit [39].

4.2.3 Digital Oscilloscope

The digital oscilloscope is used to trace the time history of the deflection measurements, as well as, the voltage difference across the resistance heater. Once the desired signal is captured on the oscilloscope, it is saved on the oscilloscope hard disk to be used later in the analysis. The Tektronix oscilloscope (TDS5034B model) has an 8 bit vertical resolution, a maximum sampling rate of 50 GS/s, and a 350MHz/s bandwidth.

4.2.4 Push-pull device

The MDC push-pull device is a linear motion feed-through. The push-pull device seals against Ultra High Vacuum (UHV) conditions. It is operated by observing the motion process through the vacuum viewport. It provides a linear motion through a stainless steel hand-held actuator shaft. To ensure sealing against vacuum, the push-pull is equipped with a 1.33" anodized aluminum flange. The scale on the push-pull is marked in increments of 0.025". The maximum travel distance of the push-pull linear

motion feed-through is 1.0". The model used in this work is SBLM-133-1 push-pull model. Figure 4.4 shows the push-pull device used in this work.

Figure 4.4: Push-pull linear motion feed-through.

4.2.5 Piezo-stack actuator

The piezo-stack actuator used in this work is a *Physik Instrumente* (PI) model P-840.60. The actuator used is a high resolution linear actuator for static and dynamic applications. The response time and resolution of the actuator are on the order of sub-milliseconds and sub-nanometers, respectively. The resonant frequency of the actuator is 6 kHz. The high resonant frequency of the actuator, relative to the operating frequency of the engine, makes it ideal for translating the motion to the thermal switch with minimum vibration. The travel distance of the actuator is about 80µm. The actuator is equipped with multilayer PZT ceramic stacks protected by a nonmagnetic stainless steel case, with internal spring preload. The maximum pushing and pulling forces of the actuator are 1000 and 50N, respectively. The maximum torque limit on the tip of the actuator is 0.35N.m. It is noteworthy to mention that such an actuator is very sensitive for lateral forces, as well as pulling forces. Because of that care must be taken when

handling and mounting the actuator. The piezoelectric actuator may be stressed in the axial direction only. Tilting and shearing forces should be avoided.

4.2.6 Edge welded bellows

The edge welded bellows function as a vibration isolator in the experimental setup shown in Figure 4.1. That is the bellows help reduce the vibration transmitted to the acrylic chamber as a result of the movement of the piezo-stack actuator. The bellows are made of AMS-5512 alloy. The inner and outer diameters of the bellows are I.D=4.00" and O.D=4.970", respectively. The free length of the bellows is 3". An important characteristic of the edge welded bellows is their compatibility with vacuum environment. To ensure sealing against vacuum the bellows are welded to 9.00" ASA flanges on both ends. Both flanges are integrated with O-rings. Also, vacuum grease is used upon assembly to ensure good sealing between the flanges and the acrylic chamber.

4.3 Experimental procedure

Next, the dynamic operation of the micro heat engine is examined. First, the engine is assembled on top of the chamber as detailed in section 2.2. In the setup shown in Figure 4.1, the upper surface of the chamber serves as the lower carrier plate of the engine. Because the next few steps in setting up the experiment require moving parts around, the engine is assembled without placing the mass on top of it at this point. The mass is added in later steps. Next, the shutter is opened and the thermal switch is aligned with the engine. To do that the coordinates of the four vertical transition stages that will result in best alignment between the thermal switch and the engine are determined. Once the coordinates of the vertical transition stages are determined, the thermal switch is lowered to its initial position and the chamber is sealed by closing the shutter. At this

point the chamber is filled with air at atmospheric pressure. To replace the air with a different gas the chamber is pumped down to vacuum and refilled with the desired gas until the pressure inside the chamber is atmospheric again. The mass is then carefully placed on top of the engine using a pair of tweezers. Lastly, the shutter is opened and the thermal switch is allowed to gain access to the engine.

At this point, one can start operating the engine. To operate the engine, the Labview program is started and signals to the resistance heater and the thermal switch are defined. To define the two signals, frequency, amplitude, and phase between the two signals are input to the Labview program. A periodic voltage $V_h(t)$ consisting of a uni-polar square wave is applied across the resistance heater. Each time the voltage is applied electrical power is dissipated as heat and transferred into the bottom membrane. The two signals from the Labview program are fed continuously to the engine and thermal switch. Thereby a cyclic operation of the engine is achieved.

Chapter 5

MATHEMATICAL MODELING

5.1 Introduction

When building a device with complicated geometry, like the micro heat engine, a mathematical modeling of the device is crucial. The mathematical model helps in understanding the interaction between different design parameters, predicting the performance of the device for certain geometry, and optimizing the device geometry. The mathematical model is built using the fundamental laws and principles, with proper assumptions.

In this work, a mathematical model of the micro heat engine is developed. A mathematical model of the engine is obtained by applying conservation of mass and energy. Newton's laws are applied to the motion of the top and bottom membranes. The model in its most general form is nonlinear. A linearized version of the model is obtained by making the proper assumptions. A transfer-function approach is then used to analyze the performance of the engine, and to interpret experimental measurements. In this analysis the engine is viewed as a system with input and outputs. The rate of heat, $q(t)$ delivered to the heater resistance is chosen to be the input to the system. The output from the system is chosen to be the velocity of the top membrane, $u(t)$. Complex exponential method is used upon solving the model. A MATLAB code is used to implement the system of linear equations. Details about model development and validation are found in [32, 45-46].

First, the governing equations of the engine are developed. Next, the linearized version of the model is obtained. Throughout the analysis it is assumed that departures Δ

from the static positions are very small; the liquid-vapor mixture inside the cavity of the engine is saturated, the vapor inside the bubble behaves according to the ideal gas law; and the natural frequency of the bottom membrane is much higher than the natural frequency of the top membrane. In the following sections the preceding assumptions are discussed in more details.

5.2 Geometry

A model schematic of the engine is shown in Figure 5.1. The cavity of the engine is cylindrical in shape with radius r_o and nominal thickness h. In the cavity there is a central vapor bubble of radius r_i. Liquid occupies the remaining annulus. There is a liquid film of small thickness underneath the bottom of the bubble. The top of the cavity is bounded by the top membrane (expander) of mass m, constrained to move by a spring of stiffness s and two dampers with coefficients b_f and b respectively. The damper b_f is included to account for frictional losses in the engine. The damper b is used to model the useful work harvested by an energy convertor that converts the mechanical power into electrical power. From the bottom, the bubble is bounded by a movable membrane (evaporator) constrained by the spring s_h. The motions of the top and bottom membranes are measured by the displacement x and x_h, respectively. $T_o+\Delta T$, $P_o+\Delta P$, and $\rho_o+\Delta\rho$ are the instantaneous temperature, pressure and density of the bubble. The instantaneous temperature of the liquid layer is given by $T_o+\Delta T_l$. The subscript "o" indicates an ambient and/or static component, while Δ indicates a departure from the ambient value.

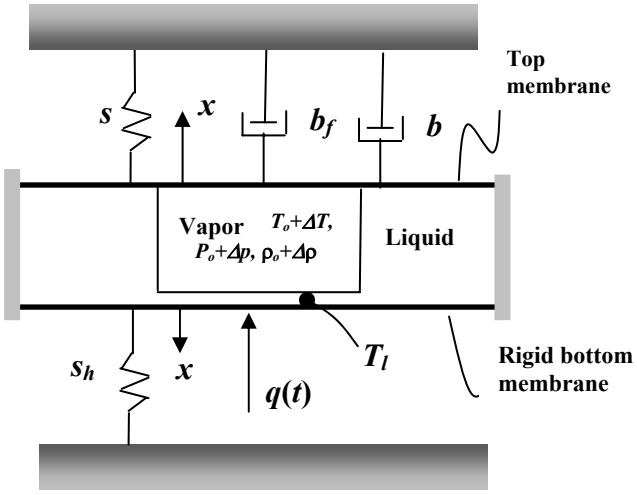

Figure 5.1: Engine model schematic.

5.3 Governing equations

For a control volume bounding the bubble, the rate of mass transfer to the bubble requires

$$\frac{d}{dt}\left[(\rho_o+\Delta\rho)(V_o+\Delta V_g+\Delta V_h)\right]=\dot{m}, \tag{5.1}$$

where $\dot{m}$ is the rate of mass transfer to the vapor bubble caused by evaporation and condensation of the liquid. The instantaneous volume of the bubble is described by $V_o+\Delta V_g+\Delta V_h$, where the static volume V_o is $V_o=\pi r_i^2 h$, and ΔV_g and ΔV_h are contributions to the bubble volume caused by the motions of top and bottom membranes, respectively. To model evaporation and condensation of the vapor the Langmuir-Knudsen model is used [47]

$$\dot{m}= S\sqrt{\frac{M}{2\pi R_u}}\left[\frac{p_l(T_o+\Delta T_l)}{\sqrt{T_o+\Delta T_l}}-\frac{P_o+\Delta p}{\sqrt{T_o+\Delta T}}\right], \tag{5.2}$$

where M is the molecular weight of the vapor, R_u=8.31 J/mol•K is the universal gas constant, $T_o + \Delta T_l$ is the temperature of the liquid, p_l is the saturation pressure of the liquid, and $S=\pi r_i^2$ is the area of the bottom surface of the vapor bubble.

For a control volume bounding the bubble, conservation of energy requires

$$\frac{d}{dt}\left[(\rho_o + \Delta\rho)c_v\left(V_o + \Delta V_g + \Delta V_h\right)(T_o + \Delta T)\right] = \dot{m}\left(u + \frac{P_o + \Delta p}{\rho_o + \Delta\rho}\right) - (P_o + \Delta p)\frac{d\left(V_o + \Delta V_g + \Delta V_h\right)}{dt} - U_B \Delta T \quad , \tag{5.3}$$

where u is the internal energy of mass transport associated with evaporation and condensation, and U_B is an overall heat transfer coefficient intended to account for heat transfer from the bubble to its surroundings. In (5.3), the internal energy flows into the bubble due to mass transfer is given by $\dot{m}u$. The flow work to account for transport of vapor into the bubble is given by $\dot{m}\,\frac{P_o + \Delta p}{\rho_o + \Delta\rho}$, and denoted by W1 in Figure 5.2. The boundary work done by the upper membrane i.e. $(P_o + \Delta p)\frac{d\left(V_o + \Delta V_g + \Delta V_h\right)}{dt}$ is denoted by W2 in Figure 5.2. The heat lost by bubble to the environment is given by $U_B \Delta T$. It is assumed that all of the latent heat of evaporation and condensation was expended in the liquid. The vapor in the bubble is assumed to be governed by the ideal gas law

$$\rho_o + \Delta\rho = \frac{P_o + \Delta p}{R(T_o + \Delta T)} \quad , \tag{5.4}$$

where $R=R_u/M$ is the mass-specific gas constant.

Conservation of energy for the liquid layer beneath the bubble is given by

$$C_T \Delta \dot{T}_l = q(t) - U\Delta T_l - h_{fg}\dot{m} \quad , \tag{5.5}$$

where C_T is the thermal inertia of the liquid layer, U is the overall heat transfer coefficient intended to account for heat conduction loss from the liquid above the evaporator membrane to its immediate surroundings, and h_{fg} is the latent heat of the liquid.

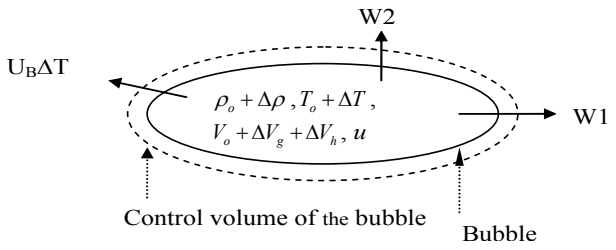

Figure 5.2: Conservation of energy in the bubble.

Newton's laws are used to model the motion of the top and bottom membranes

$$\frac{(m+\overline{m})}{(\pi r_o^2)^2}\Delta\ddot{V}_g + \frac{(b+b_f)}{(\pi r_o^2)^2}\Delta\dot{V}_g + \frac{s}{(\pi r_o^2)^2}\Delta V_g = \Delta p \quad , \tag{5.6}$$

$$\frac{s_h}{(\pi r_i^2)^2}\Delta V_h = \Delta p \, , \tag{5.7}$$

where $\overline{m}$ is the effective mass added to the top membrane caused by liquid movements. The displacement of the top membrane x is related to radial and linear expansions of the bubble through $\Delta V_g = \pi r_o^2 x$, and a similar expression relates the displacement of the evaporator x_h and ΔV_h. An Antoine correlation given by [48]

$$\log(p_l) = \hat{A} - \frac{\hat{B}}{T_l + \hat{C}}, \tag{5.8}$$

is used to model the saturation behavior of the working medium, where $\hat{A}$, $\hat{B}$, and $\hat{C}$ are constants for the particular working medium. The set (5.1-5.8) represents a nonlinear model. To allow an analysis, the set (5.1-5.8) is linearized as discussed in the next section.

5.4 Linearization of the model

The measurements, presented in the subsequent chapters, indicate that a linearized model is appropriate for conditions observed. For this reason, a linearized version of the model is extracted from the nonlinear model. The importance of nonlinearity would manifest itself on a case by case basis. If nonlinearity were important, the non-linear model for the engine would be used. A linear version of the model is obtained if the departures Δ of each quantity from their static values are very small.

A linearized form of the Langmuir evaporation condensation model in (5.2) is obtained using Taylor series expansion, and applying Antoine correlation (5.8). The linearized form of Langmuir evaporation condensation model in (5.2) is given by

$$\dot{m} = S\sqrt{\frac{M}{2\pi R_u}}\left[\frac{p_l(T_o + \Delta T_l)}{\sqrt{T_o + \Delta T_l}} - \frac{P_o + \Delta p}{\sqrt{T_o + \Delta T}}\right] \approx$$

$$B\,\Delta T_l - S\sqrt{\frac{M}{2\pi R_u}}\,\frac{1}{\sqrt{T_o}}\,\Delta p + S\sqrt{\frac{M}{2\pi R_u}}\,\frac{\rho_o R}{2\sqrt{T_o}}\,\Delta T \quad , \tag{5.9}$$

where B is given by

$$B = \frac{10^{\hat{A} - \frac{\hat{B}}{T_o + \hat{C}}}}{\sqrt{T_o}} \left[\frac{\bar{B} \ln 10}{(T_o + \bar{C})} - \frac{1}{2 T_o} \right] \quad . \tag{5.10}$$

A linearized version of (5.1) is:

$$\dot{m} = \frac{d}{dt}\left[(\rho_o + \Delta\rho)(V_o + \Delta V_g + \Delta V_h) \right] \approx (\rho_o) \left(\Delta \dot{V}_g + \frac{(\pi r_i^2)^2}{s_h} \Delta \dot{p} \right) + \Delta \dot{\rho} V_o \quad . \tag{5.11}$$

For the ideal gas (5.4) a linear approximation is given by

$$\Delta\rho = \frac{P_o}{R(T_o^2)} \Delta T + \frac{1}{R T_o} \Delta p \quad . \tag{5.12}$$

Substitution of (5.9) in (5.11) and using the linearized version of the ideal gas (5.12) results in a linearized version of the mass conservation of the bubble given by

$$\begin{aligned} &\Delta \dot{V}_g + \left(\frac{V_o}{\rho_o R T_o} + \frac{(\pi r_i^2)^2}{s_h} \right) \Delta \dot{p} - \frac{V_o}{T_o} \Delta \dot{T} = \\ &B \Delta T_l - \frac{S}{\rho_o} \sqrt{\frac{M}{2\pi R_u}} \frac{1}{\sqrt{T_o}} \Delta p + \frac{S}{\rho_o} \sqrt{\frac{M}{2\pi R_u}} \frac{\rho_o R}{2\sqrt{T_o}} \Delta T \end{aligned} \quad . \tag{5.13}$$

A linearized version of energy conservation for the liquid layer is give by

$$C_T \Delta \dot{T}_l = q(t) - U \Delta T_l - h_{fg} B S \sqrt{\frac{M}{2\pi R_u}} \Delta T_l + h_{fg} S \sqrt{\frac{M}{2\pi R_u}} \frac{\gamma + 1}{2\gamma\sqrt{T_o}} \Delta p \quad , \tag{5.14}$$

where γ is the isentropic compression ratio of the vapor, i.e. $\gamma = \frac{C_P}{C_v}$. A linearized version of the energy conservation for the bubble is given by

$$\frac{V_o}{T_o} \Delta \dot{T} - \frac{V_o}{\rho_o c_p T_o} \Delta \dot{p} = -\frac{U_B}{\rho_o c_p T_o} \Delta T \quad . \tag{5.15}$$

The set (5.6, & 5.13-5.15) represents a linear set of four equations with four unknowns (ΔV_g, Δp, ΔT, and ΔT_l). The state variable representation of the linearized model is given by:

$$\begin{bmatrix} 1 & 0 & 0 & 0 & 0 \\ \dfrac{(b+b_f)}{(\pi r_o^2)^2} & \dfrac{(m+\overline{m})}{(\pi r_o^2)^2} & 0 & 0 & 0 \\ 0 & 0 & 0 & 0 & C_T \\ 1 & 0 & \left(\dfrac{V_o}{\rho_o R T_o} + \dfrac{(\pi r_i^2)^2}{s_h}\right) & \dfrac{V_o}{T_o} & 0 \\ 0 & 0 & -\dfrac{V_o}{\rho_o C_p T_o} & \dfrac{V_o}{T_o} & 0 \end{bmatrix} \begin{Bmatrix} \Delta \dot{V}_g \\ \Delta \ddot{V}_g \\ \Delta \dot{p} \\ \Delta \dot{T} \\ \Delta \dot{T}_l \end{Bmatrix} =$$

$$\begin{bmatrix} 0 & 1 & 0 & 0 & 0 \\ -\dfrac{s}{(\pi r_o^2)^2} & 0 & 1 & 0 & 0 \\ 0 & 0 & h_{fg} S \sqrt{\dfrac{M}{2\pi R_u}} \dfrac{\gamma+1}{2\gamma\sqrt{T_o}} & 0 & -\left(U + h_{fg} B S \sqrt{\dfrac{M}{2\pi R_u}}\right) \\ 0 & 0 & -\dfrac{S}{\rho_o}\sqrt{\dfrac{M}{2\pi R_u}}\dfrac{1}{\sqrt{T_o}} & \dfrac{S}{\rho_o}\sqrt{\dfrac{M}{2\pi R_u}}\dfrac{\rho R}{2\sqrt{T_o}} & B \\ 0 & 0 & 0 & -\dfrac{U_B}{\rho_o c_p T_o} & 0 \end{bmatrix} \begin{Bmatrix} \Delta V_g \\ \Delta \dot{V}_g \\ \Delta p \\ \Delta T \\ \Delta T_l \end{Bmatrix} + \begin{Bmatrix} 0 \\ 0 \\ 1 \\ 0 \\ 0 \end{Bmatrix} q(t)$$

(5.16)

5.5 Reduced linearized model, no heat transfer from the bubble (U_B=0)

The linearized model can be further reduced if the heat transfer from the bubble is neglected, i.e. U_B=0. Computations showed that setting U_B=0, did not alter the model predictions significantly. Because of that it can be assumed that heat loss from the bubble to the surrounding is negligible, i.e. U_B=0. Under this assumption, the linear model (5.16) is simplified to

$$\begin{bmatrix} 1 & 0 & 0 & 0 \\ \dfrac{(b + b_f)}{(\pi\ r_o^{\,2})^2} & \dfrac{(m + \overline{m})}{(\pi\ r_o^{\,2})^2} & 0 & 0 \\ 0 & 0 & 0 & C_T \\ 1 & 0 & \left(\dfrac{V_o}{\rho_o R T_o} + \dfrac{(\pi r_i^{\,2})^2}{s_h} \right) & 0 \end{bmatrix} \begin{Bmatrix} \Delta \dot{V}_g \\ \Delta \ddot{V}_g \\ \Delta \dot{p} \\ \Delta \dot{T}_l \end{Bmatrix} =$$

$$\begin{bmatrix} 0 & 1 & 0 & 0 \\ \dfrac{-s}{(\pi r_o^2)^2} & 0 & 1 & 0 \\ 0 & 0 & h_{fg} S \sqrt{\dfrac{M}{2\pi R_u}} \dfrac{\gamma+1}{2\gamma\sqrt{T_o}} & -\left(U + h_{fg} B S \sqrt{\dfrac{M}{2\pi R_u}} \right) \\ 0 & 0 & \dfrac{S}{\rho_o} \sqrt{\dfrac{M}{2\pi R_u}} \dfrac{\gamma+1}{2\gamma\sqrt{T_o}} & \dfrac{BS}{\rho_o} \sqrt{\dfrac{M}{2\pi R_u}} \end{bmatrix} \begin{Bmatrix} \Delta V_g \\ \Delta \dot{V}_g \\ \Delta p \\ \Delta T_l \end{Bmatrix} + \begin{Bmatrix} 0 \\ 0 \\ 1 \\ 0 \end{Bmatrix} q(t)$$

. (5.17)

5.6 Solution of the linear system of equations

The complex exponential method is used to obtain the solution of the linear set (5.16) [49-50]. In this method the solution of the linear model, is assumed to take the exponential form $\Delta Y = Ae^{\pm j 2\pi f_o t}$, where ΔY is the state variable to be determined, t is time in sec, and f_o is the fundamental frequency in Hertz (Hz) at which the engine is operated. Details on the solution of the linear systems are found in Appendix A.

Chapter 6

DATA ANALYSIS AND PERFORMANCE MEASUREMENTS

6.1 Overview

In this chapter methods used for data analysis are presented. When the micro heat engine is operated at resonance, coupling between thermodynamics, heat transfer, and dynamics plays a strong role in defining the overall behavior of the micro heat engine. In the subsequent sections techniques used to interpret the behavior of the micro heat engine are presented.

On the one hand the micro heat engine is viewed as a linear system consisting of several subsystems. The input to the system is the heat rate $q(t)$ delivered to the engine. The output from the system is the velocity of top membrane $u(t)$. Fourier series are used to represent the input and output from the system. A transfer function analysis is then used to look at the behavior of the engine over a frequency spectrum. A least squares method is then used to compare the modeled transfer function to the measured one. On the other hand the micro heat engine performance is interpreted by looking at the thermodynamic state of the engine cavity. Pressure, volume, temperature, and entropy changes inside the cavity of the engine are used to build pressure-volume and temperature-entropy diagrams. The mechanical work, thermal efficiency, and Carnot efficiency are then extracted from these diagrams. In the following subsequent sections, various analysis methods are presented in more details.

6.2 Fast Fourier transformation (FFT)

The Fourier transform is a mathematical tool used extensively to represent a periodic function by decomposing the function into a weighted sum of a sinusoidal component functions referred to as modes [49-50]. For a continuous signal, one form of Fourier transform is given by

$$\hat{X}(f) = \int_{-\infty}^{+\infty} x(t) \exp(-j2\pi ft)\ dt \tag{6.1}$$

where *x(t)* is a continuous-time signal and *f* is the transform variable with the units of Hz. In most modern signal processing systems, the signal of interest is sampled at discrete times. The discrete signal is then analyzed at a discrete number of points *N* instead of as a continuous function. This analysis is called a discrete Fourier transform (DFT). For discrete signal sampled by x_n DFT is given by [49]

$$\hat{X}_k = \sum_{n=0}^{N-1} x_n . \exp(-\frac{j2\pi kn}{N}) \quad , \text{n , } k\text{=0,1,2,…….,N-1 ,} \tag{6.2}$$

the coefficients $\hat{X}_k$ are in general complex valued, and known as the DTF coefficients, x_n are the sampled data points, i.e. $x_n = x(n\Delta t)$. The fundamental period $T_o = N\Delta t$ is the reciprocal of the fundamental frequency f_o with units of sec, and Δt is the sampling interval. If the number of the data points, *N* is an even power of 2^P, *P* is an integer, the DFT coefficients are then determined using algorithm known as a Fast Fourier Transform (FFT). The coefficients $\hat{X}_{(N/2)+1}$ through $\hat{X}_{(N-1)}$ are complex conjugates of the coefficients $\hat{X}_0$ through $\hat{X}_{(N/2)}$, only the coefficients $\hat{X}_0$ through

$\hat{X}_{N/2}$ are needed to represent the real data. Once the DFT coefficients are determined, the signal *x(t)* can be expressed in terms of a sum of sinusoidal components given by

$$x(t) = \frac{1}{N}\hat{X}_o + \frac{1}{N}\hat{X}_{\frac{N}{2}}\cos(2.\pi.f_{\frac{N}{2}}.t + \Phi_{\frac{N}{2}}) + \sum_{k=1}^{\frac{N}{2}-1}\frac{2}{N}\left|\hat{X}_k\right|\cos(2\pi f_k.t + \Phi_k)\ , \tag{6.3}$$

where $\hat{X}_k$ are the amplitudes, and Φ_k are the phases i.e. $\Phi_k = \arg(\hat{X}_k)$. The harmonic frequencies f_k are given by $f_k = \frac{k}{T_o} = \frac{k}{N.\Delta t} = k.f_o$. FFT analysis is used in the following chapters to compare model predictions to measured data. An FFT algorithm was implemented using MATLAB software. The detailed MATLAB coding of the FFT algorithm is given in appendix B.

6.3 Transfer function analysis

A transfer function is defined as a mathematical representation of the relation between input and output of a linear time invariant system [51]. For a continuous- time input *x(t)* and output *y(t),* the transfer function is the linear mapping of the Laplace transform of the input *X(s)* , to the output *Y(s)* , given by

$$H(s) = \frac{Y(s)}{X(s)} = \frac{L\big(y(t)\big)}{L\big(x(t)\big)}, \tag{6.4}$$

where *H(s)* is the transfer function of the linear system. For a discrete-time system, the transfer function *H(z)* is give by $H(z) = \frac{Y(z)}{X(z)}$, where *Y(z)* and *X(z)* are obtained by converting the time domain signal into a complex frequency domain representation, i.e. *Z*-transform.

In the transfer function approach, a periodic voltage $V_h(t)$ consisting of unipolar square wave is applied across the resistance heater. Each time the voltage is applied electrical power is dissipated as heat and transferred into the bottom evaporator membrane. This heat transfer evaporates the layer of liquid working fluid held in the wick on the bottom evaporator membrane. The resultant increase in pressure inside the cavity, Δp causes the top membrane (expander) to flex outward. A periodic voltage $V_h(t)$ applied across the resistance heater thus results in a periodic displacement of the top expander membrane, $x(t)$.

A linear-system transfer-function approach is used to interpret the experimental data. In this approach, the input to the system is taken to be the rate of heat input to the engine, $q(t)$ computed from the measured heater resistance voltage i.e. $q(t)=V_h^2(t)/R_h$, where R_h is the resistance across the heater. The output from the system is taken to be the velocity of the top membrane, $u(t)$ computed from the measured displacement of the membrane, $u(t) = x^{\bullet}(t)$. The experimentally determined periodic heat input is represented by a Fourier series

$$q(t) = Q_o + \sum_k Q_k \cos\left(2\pi f_k t + \theta_k\right), \tag{6.5}$$

where Q_k and θ_k are the amplitudes and phases, respectively. The k^{th} amplitudes Q_k and phases θ_k are extracted from the heat input $q(t)$ using an FFT algorithm. The number of k components is determined by the number of sampled points in a measured waveform. Likewise the experimentally determined periodic velocity of the top membrane is represented by the Fourier series

$$u(t) = U_0 + \sum_k U_k \cos\left(2\pi f_k t + \gamma_k\right) \quad , \tag{6.6}$$

As before, amplitudes, U_k and phases, γ_k are extracted from the velocity of the top membrane, $u(t)$, using the FFT algorithm. Interpretation of the performance of the engine is then reduced to predicting the system transfer function $\Gamma(f_K)$ between the coefficients Q_k and U_k at each of the k frequencies f_k, i.e. $\Gamma(f_k) = \frac{U_k}{Q_k}$.

6.4 Least squares method

The set (5.16) represents a linear model of the micro heat engine. The bottom membrane diameter $2r_o$, bubble diameter $2r_i$, cavity thickness h, upper membrane stiffness s, lower evaporator stiffness s_h, PF-*5060* working fluid properties, and environmental conditions are predetermined parameters in the model. Table 6.1 shows an example of the predetermined parameters of a modeled 10x10mm micro heat engine. The thermal inertia of the liquid layer C_T, coefficient of heat transfer losses from liquid layer to the surrounding U, coefficient of heat transfer losses from bubble to the surrounding U_B, frictional damping b_f, and total mass of upper membrane $(m \mid \bar{m})$ are floating parameters in the model. Since no energy conversion device is attached to the engine, the damping coefficient was set zero, i.e. b=0 N.s/m. Independent measurement of the floating parameters was not feasible. Because of that, the floating parameters C_T, U, U_B, b_f, and $(m + \bar{m})$ are set to be the free parameters that are determined using the least squares method.

In the least squares method, the goal is to adjust a model function to best fit the data points obtained experimentally. This is done by adjusting the floating parameters in the model to minimize the squares of the error. For example, let the model function be $Y = F(x,c)$, where Y is the dependent variable, x is the independent variable, and c are

the free parameters in the model. The least squares method minimizes the sum of the squares of the error equation described by $S(c) = \sum_{k=1}^{k=n} (Y_i. - F(x_i, c))^2$, by adjusting the free parameters *c*, where the measured data are given by Y_i. MATLAB software was used to implement the least squares method in this work. The detailed MATLAB code for the least squares method is given in appendix C.

Evaporator diameter (mm), $2r_o$	8.0
Bubble diameter (mm), $2r_i$	7.2
Cavity thickness (μm), *h*	150
Upper membrane stiffness (N/m), *s*	2435
Lower membrane stiffness (N/m), s_h	5600
Room temperature (K), *To*	294
Liquid density(kg/m^3) , ρ	1775
Vapor density(kg/m^3) , ρ_o	3.53
Molecular weight(kg/mol), *M*	0.338
Saturated pressure(kPa), P_o	25.097
Specific heat (J/kg.K), C_p	755
Gas constant(J /kg.K), *R*	24.18
Isentropic compression ratio, γ	1.033
Enthalpy(kJ/kg) , h_{fg}	94.0
$\hat{A}$	9.73
$\hat{B}$	1562
$\hat{C}$	0

Table 6.1: Example of predetermined parameters used in linearized model computations (10x10 mm engine).

6.5 Parseval's theorem

Parseval's theorem is often written as

$$\int_{-\infty}^{+\infty} |x(t)|^2 \, dt = \int_{-\infty}^{+\infty} \left| \hat{X}(f) \right|^2 df \,, \tag{6.7}$$

where $\hat{X}(f)$ represents the continuous Fourier transform of *x(t)*, and *f* represents the frequency component. The interpretation of Parseval's theorem is that the sum of the total energy contained in a waveform *x(t)* over all the time interval *t* equals the total

energy of the waveform's Fourier transform $\hat{X}(f)$ summed across the continuous spectrum. For a discrete Fourier transform, the relation becomes

$$\int_0^{T_P}\left(x(t)-\bar{x}\right)^2 dt = \frac{1}{2}\sum_{k=1}^{\frac{N}{2}-1}\left|\frac{2}{N}\hat{X}_k\right|^2 + \frac{1}{2}\left|\frac{\sqrt{2}}{N}\hat{X}_{\frac{N}{2}}\right|^2, \tag{6.8}$$

where $\hat{X}_k$ are the discrete Fourier transform of x_n, and $\bar{x} = \frac{1}{T}\int_0^T x^2(t)dt$. Using Parseval's theorem, a prediction of the effect of heat pulse duration on the micro heat engine performance is possible. Consider a heat rate $q(t)$, delivered to the engine. Subject the heat rate $q(t)$ to the constraint that there is a fixed energy E delivered to the engine per cycle, and $q(t)$ is a unipolar pulse, given by

$$q(t) = \left\{ \begin{array}{l} \overset{o}{Q}, \quad t < T \\ 0, T < t < T_o \end{array} \right\}, \tag{6.9}$$

where T is the duration of the pulse, and $\overset{o}{Q}$ is the magnitude of the pulse. The energy delivered to the engine per cycle is given by $E = \overset{o}{Q}T$. The Fourier coefficients Q_k of the heat rate $q(t)$ are then given by

$$Q_k = \frac{E}{T}\sqrt{\left[\frac{2}{k\pi}\sin\left(k\pi\frac{T}{T_o}\right)\cos\left(k\pi\frac{T}{T_o}\right)\right]^2 + \left[2\frac{\cos^2\left(k\pi\frac{T}{T_o}\right)-1}{k\pi}\right]^2}. \quad k > 0 \tag{6.10}$$

Using Parseval's theorem, the energy delivered to the engine per cycle is rewritten in terms of E, T, and T_o given by

$$E = E\left(\frac{T}{T_o}\right)^2 + \sum_{k=1}^{\frac{N}{2}-1} \frac{T^2}{2E} Q_k^2 \quad . \tag{6.11}$$

Equation 6.11 shows that for a fixed amount of energy E delivered to the engine, the DC energy component, i.e. $E\left(\frac{T}{T_o}\right)^2$ in (6.11) depends on the ratio $\left(\frac{T}{T_o}\right)$. For example, if the ratio $\frac{T}{T_o} = 0.5$ then the DC component, $E\left(\frac{T}{T_o}\right)^2$ represents 25% of the total energy delivered to the engine. Meanwhile, if the ratio $\frac{T}{T_o} = 0.01$, then the DC component represents only 1x 10^{-4}E. Based on this argument, a short heat rate pulse $\left(\frac{T}{T_o}\right)$ is optimal for transfer of energy to the engine. Given that a short heat rate impulse is desirable, one can determine other properties in the limit $T/T_o \to 0$. In this limit for a finite frequency bandwidth the heat rate coefficients Q_k become

$$\lim_{T/T_o \to 0} Q_k \approx 2 f_o E \left[1 - \left(k\pi \frac{T}{T_o}\right)^2\right] \approx 2 f_o E \,. \tag{6.12}$$

Thus in the limit $T/T_o \to 0$ the heat rate amplitudes Q_k are proportional to the fundamental frequency f_o . That means running the engine at higher frequencies is desirable. However, increasing the operating frequency f_o will place fewer components of the heat rate spectrum Q_k in the frequency bandwidth with large $\Gamma(kf_o)$.

6.6 Performance measurements

As the micro heat engine undergoes the cyclic operation established in section 2.3, the thermodynamic state of the vapor changes continuously. Determining the

thermodynamic state of the vapor is crucial to define the thermodynamic cycle of the engine. To completely define the cycle of the engine, both pressure-volume and temperature-entropy diagrams are needed. Pressure and volume changes inside the cavity are tracked by measuring the deflection of the bottom evaporator membrane and top expander membrane, respectively. Changes in temperature and entropy of the cavity are then mapped directly from pressure measurements.

6.6.1 Pressure and volume measurements:

The volume and pressure are obtained from measurements of the top expander membrane and bottom evaporator membrane deflections, respectively. The volume under a square membrane is determined by performing a double integral on the membrane deflection profile equation given by [52]

$$\Delta V(\delta) = \frac{\delta}{a^4}\int_{-a}^{a}\int_{-a}^{a}(a^2 - x^2)(a^2 - y^2)\left[1 + \frac{R}{a^2}(x^2 + y^2)\right]dxdy \quad , \tag{6.13}$$

where δ is the center deflection, a is ½ the edge length, x and y are coordinates on the membrane, and R=0.34 is a constant determined by matching the deflection profile of the equation to experimental data. For a 10x10 mm top membrane, the integral (6.13) is simplified to

$$\Delta V(\delta) = \delta\frac{16}{45}a^2(2R + 5). \tag{6.14}$$

Pressure is inferred from top or bottom membrane center deflection using a pressure-deflection curve fit. The pressure-deflection curve is determined experimentally using a bulge tester. The procedure and apparatus of correlating pressure-underneath a membrane to center deflection of membrane are described in [53]. Because the pressure-

deflection relation is a function of side length of the membrane, residual stresses, thickness, and material properties of membrane, a separate pressure-deflection curve should be generated for each type of membrane. A general form of the pressure-deflection curve is given by [52]

$$\Delta P = C_1\delta + C_2\delta^3 \quad , \tag{6.15}$$

where δ is the midpoint deflection in micrometers and ΔP is the pressure change in kPa, C_1 and C_2 are constants determined by matching the deflection profile of the equation to experimental data. For 2μm thick, 64mm^2 silicon bottom membrane (evaporator) constants C_1 and C_2 are $1.4197\ \text{X}10^{-2}$ and $8.4\ \text{X}10^{-6}$, respectively.

Far away from resonance, the deflection of either the top or bottom membranes is used to determine the pressure. However, for a resonant operation, the pressure is inferred from measurements of bottom membrane (evaporator) deflection because the natural frequency of the bottom membrane is much higher than any frequency contained in the experimental measurements.

6.6.2 Correction of the stiffness of top membrane

In the mathematical modeling described in sections 5.3-5.4, the average deflection of the top membrane, x_b is used in model development. Experimentally, the deflection of the midpoint of the top membrane, δ is measured. A correlation between the midpoint deflection δ, and the average deflection x_b was established and used in the model. Figure 6.1 shows the volume under the top expander membrane. In Figure 6.1, *2a* is the side length of the top membrane and F_b is the force distributed over the membrane area. The volume under the membrane, $\forall_{mem,1}$ based on the midpoint deflection δ is determined

(6.13-6.14). The virtual volume under the top membrane based on the corrected value x_b is given by $\forall_{mem,2} = (2a)^2 x_b$. If the volume is constrained to be constant in both cases, i.e. $\forall_{mem,2} = \forall_{mem,1}$ then solving for x_b results in

$$x_b = 0.505\ \delta, \tag{6.16}$$

assuming the stiffness of the membrane is linear, $s = 1.98 s_o$, where s_o and s are the stiffness of the top membrane based on δ and x_b, respectively.

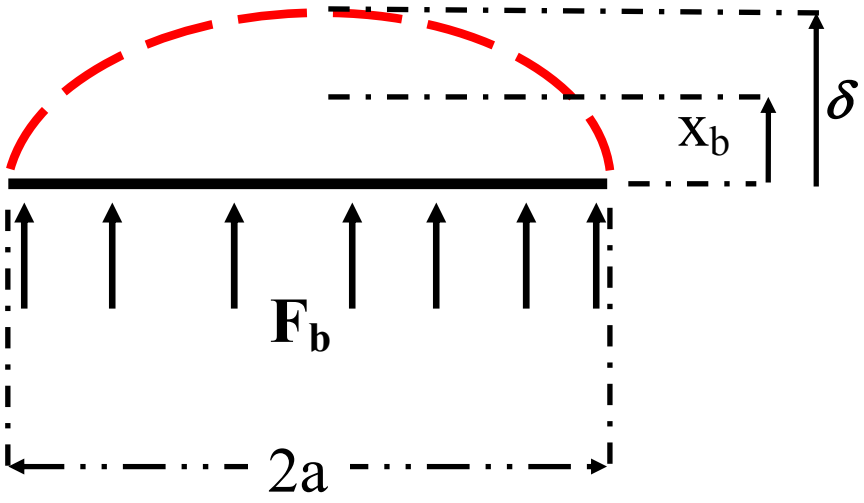

Figure 6.1: Volume under top membrane.

6.6.3 Temperature and entropy

Vapor temperature and entropy variation inside the cavity could not be specified from direct measurements. The liquid-vapor mixture inside the cavity is assumed to be saturated. The temperature inside the cavity is determined using vapor pressure measurements outlined in the previous section. To specify vapor entropy changes inside the cavity, two independent intensive properties are needed [54]. The quality of liquid-

vapor mixture, $\overline{Q}$ along with vapor pressure serve as the two intensive properties needed. The quality of liquid-vapor mixture is calculated based on volume and density changes of vapor. The quality $\overline{Q}$ is given by

$$\overline{Q} = \frac{V_{inst} \bullet \rho_{inst}}{m_{total}} . \tag{6.17}$$

$$V_{inst} = V_{initial} + \Delta V(\delta) . \tag{6.18}$$

In (6.17-6.18) V_{inst} is the instantaneous volume of vapor inside the cavity, calculated based on initial volume, $V_{initial}$ and volume changes $\Delta V(\delta)$ from (6.13). The product $(V_{inst} * \rho_{inst})$ represents the instantaneous mass of vapor inside the cavity. The total mass of liquid-vapor mixture is given by m_{total}. The instantaneous density of vapor ρ_{inst} is interpolated using saturation tables of PF5060 working fluid. Entropy is then given by

$$s = \overline{Q} \bullet s_{fg} , \tag{6.19}$$

$$s_{fg} = s_g - s_f . \tag{6.20}$$

where S_g and S_f are entropies of saturated vapor and saturated liquid, respectively.

6.6.4 Pressure-volume and temperature-entropy diagrams

The behavior of the micro heat engine is better understood by looking at pressure-volume and temperature-entropy diagrams. Figure 6.2 and 6.3 show a representative measured pressure-volume and temperature-entropy diagrams, respectively. The area inside either diagram represents mechanical work done by the engine, W_{mech}. Numerical integration is used to calculate the mechanical work W_{mech} of the engine. For the work presented in the subsequent chapters, trapezoidal rule is used to approximate the area

inside the diagrams [55]. Thermal efficiency of the engine η_{therm} is calculated based on the correlation given by (6.21). Energy dissipated into the heater per cycle is given by Q_{in}.

$$\eta_{therm} = \frac{W_{mech}}{Q_{in}} * 100\% \quad . \tag{6.21}$$

The temperature-entropy diagram is crucial to understanding heat addition/rejection events during the cycle. If the process moves to a greater entropy state, the area under the curve will be the amount of heat absorbed by the system in that process, i.e. Q_H. If the process moves towards a less entropy state, it will be the amount of heat removed from the system, i.e. Q_C. For any cyclic process, there will be an upper portion of the cycle and a lower portion. The area inside the cycle will then be the amount of work done by the system over the cycle:

$$W_{mech} = Q_H - Q_C \ . \tag{6.22}$$

The upper bound on the performance of any heat engine is set by the Carnot efficiency. For any engine operating between two reservoirs, the maximum efficiency is set by Carnot efficiency, η_{Carnot}. Carnot efficiency is given as by

$$\eta_{Carnot} = 1 - \frac{T_L}{T_H}, \tag{6.23}$$

where T_L and T_H are low temperature and high temperature reservoir, respectively.

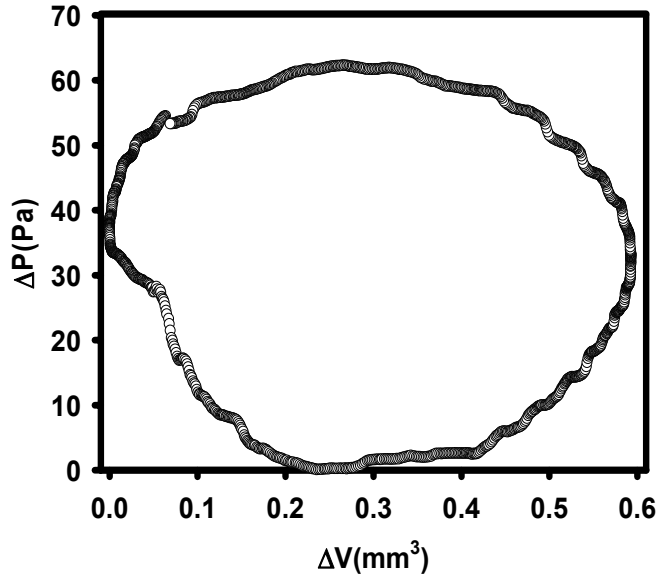

Figure 6.2: A representative pressure-volume diagram at resonance,

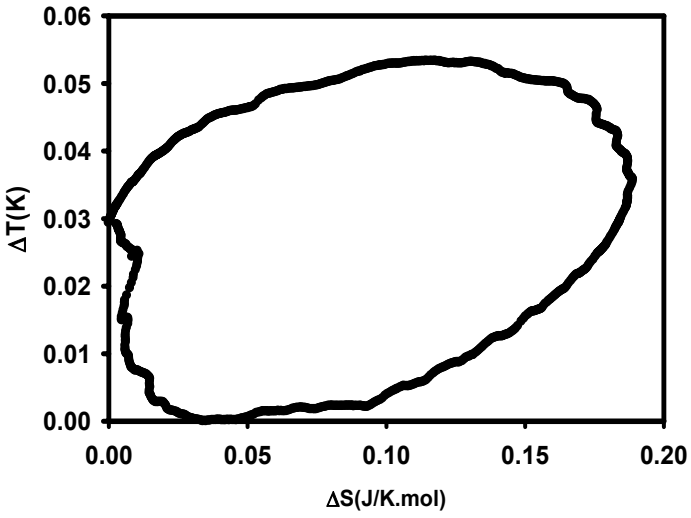

Figure 6.3: A representative temperature-entropy diagram at resonance,

Chapter 7

EXPERIMENTAL VALIDATION OF MATHEMATICAL MODEL

7.1 Overview

The mathematical model of the engine (5.1-5.8) is a nonlinear set of equations. A linearized version of the model (5.16) is extracted from the nonlinear model. The first part of this chapter focuses on experimental verification of the model. First, the linear behavior of the engine is examined. Next, the mathematical model is verified experimentally. That is, model prediction of velocity transfer function $\Gamma(f_k)$ is compared to the experimentally determined transfer function U_k/Q_k. Validation of the mathematical model is performed for both resonant and non-resonant engines.

In the second part of the chapter, preliminary measurements and tests are presented. The effects of duration of heat addition, mass of the top expander membrane, and thermal storage or thermal inertia associated with the engine cavity on the dynamic behavior of the engine are investigated using a combination of experiments and model. Two engine geometries are used: engines with 5mm by 5mm square top membranes and engines with 10mm by 10mm square top membranes. Pertinent engine parameters for both geometries are summarized in Table 7.1. The 5mm engine is used to validate the model and to investigate the effect of the duration of heat addition. The 10mm engine is used to investigate the effects of the mass of top membrane and thermal storage / inertia.

It is noteworthy to mention that in linearity tests of model validation, effect of heat duration, and effect of mass of the top membrane the thermal switch was not used and heat was rejected from the engine to the surrounding by passive conduction. Since

estimation of the heat rejection profile through the thermal switch was not possible, the input to the engines was taken to be the heat rate delivered to the heater resistance, *q(t)*. For the effect of thermal storage or thermal inertia test, the thermal switch was used for cooling the engine. The gap between the thermal switch and engine was filled with air.

Table 7.1. Engine parameters.

Parameter	Engine A	Engine B
Expander Side length, mm	5	10
Expander material	Silicon nitride	Silicon nitride
Evaporator side length, mm	4	8
Cavity thickness, μm	75	150

7.2 Linearity test

To demonstrate the linear behavior of the engine, a separate experiment was conducted. In this experiment the input energy to the engine was varied gradually. This was accomplished by changing the voltage amplitude V_o of the heat pulse delivered to the engine. The linearity test was performed on engine A in Table. 7.1. The cavity was filled with PF-5060 3M working fluid. The bubble covered 90% of the electrical heater size. To capture the behavior of the engine over a wide range of frequencies, the engine was operated at two different cycle frequencies f_o =2.0 and 10.0Hz. The heat pulse durations were chosen to be T = 5.0 and 1.0ms, respectively. The choice of these frequencies f_o and the pulse duration T allowed the collection of data down to 2.0Hz and up to 1000Hz. The engine was then operated and the displacement of the upper

membrane *x(t)* was measured using the laser vibrometer. The transfer function $\Gamma(kf_o)$ was then computed as the ratio between the velocity amplitudes U_k and the heat rate amplitudes Q_k at frequencies f_k., i.e., $\Gamma(kf_o) = \frac{U_k}{Q_k}$.

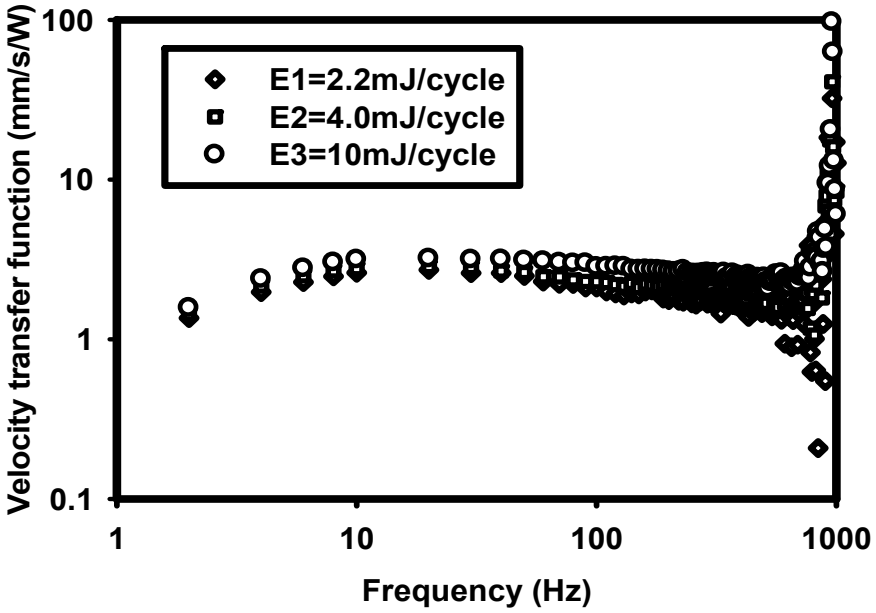

Figure 7.1 : Linearity test-velocity amplitude transfer function.

Figure 7.1 shows measured velocity transfer functions U_k/Q_k versus frequency. In Figure 7.1, the engine was operated at three different energy levels per cycle, E=2.2, 4.0 and 10.0mJ. Figure 7.1 shows that as the energy per cycle E delivered to the engine is increased from 2.2mJ, 4.0 mJ, and finally to 10 mJ, the linearity approximation is valid for low frequencies. A departure from linearity starts appearing at higher frequencies where growth in the transfer functions appear at energy levels of E=4.2 and 10mJ. However, the observed nonlinear behavior of the engine at higher frequencies is quite small and does not appear to compromise the overall success of the model.

7.3 Experimental validation of the model

The mathematical model of the engine was validated experimentally using engine A in Table.7.1. Model predictions of velocity transfer function $\Gamma(f_k)$ and phase $\phi(f_k)$ from (5.16) were compared to the experimentally determined transfer function U_k/Q_k and phase γ_k-θ_k. Figure 7.2 shows the result, a plot of the velocity transfer function magnitude versus frequency. The engine was operated at frequencies f_o =0.2, 1 and 10.0 Hz, respectively. The heat pulses were chosen to be T = 50, 10 and 1.0 ms, respectively. The choice of these frequencies f_o and heat pulses T, allowed the collection of data in frequency bandwidth of 0.2- 1000 Hz. The amount of energy delivered to the engine per cycle was fixed, E=10 mJ. Experimentally determined values of the velocity transfer function magnitude U_k/Q are shown as square symbols. The solid line indicates the model prediction of $\Gamma(kf_o)$. A least squares procedure was used to determine the values for the conduction loss coefficients U and U_B, the thermal storage coefficient C_T, and the frictional damping coefficient b_f in (5.16). Since no resonant peak appeared up to 1000 Hz, the ($m + \overline{m}$) was set equal zero. In this comparison, the parameters U =0.0346 W/K, U_B=0.064 J/K, C_T=0.00196J/K, and b_f=0.656 N.s/m, were found to minimize the squares error between the model prediction $\Gamma(f_k)$ and experimental measurements of velocity transfer function U_k/Q_k.

Fig 7.3 shows a plot of the phase of the velocity transfer function versus frequency. Experimentally determined values of phase γ_k-θ_k, are shown as square symbols. Model predictions are indicated with a solid line. Although no phase measurements were used to determine the floating parameters U , U_B, C_T, and b_f the plot shows good agreement between model predictions and experimental measurements. The model's accurate

prediction of the phase data is strong evidence of the validity of the dynamic structure of the lumped-parameter engine model (5.16).

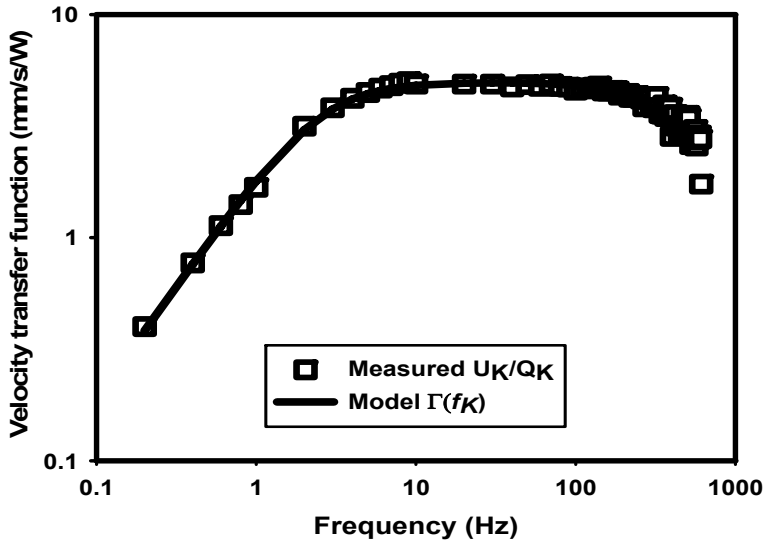

Figure 7.2: Model validation: Velocity transfer function.

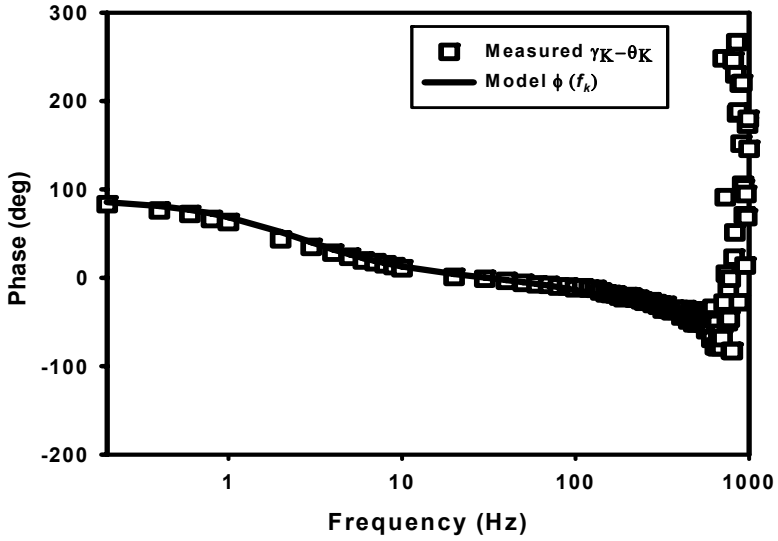

Figure 7.3: Model validation: Phase of the velocity transfer function.

7.4 Additional tests and measurements

In the following sections the effect of mass of the top membrane, the effect of thermal storage or thermal inertia associated with the cavity, and the effect of heat pulse duration on the dynamic behavior of the engine are presented.

7.4.1 Effect of mass of top membrane on the dynamic behavior of the engine

The effect of top membrane mass is examined next. The test was performed on engine B in Table. 7.1. The results are shown in Figure 7.4. The measured velocity transfer functions are indicated by symbols. The model predictions of velocity transfer functions are indicated by a solid line. First the engine was operated with no mass added to the top membrane, i.e., m_{added} =0g. Experimental results for m_{added}=0g are shown with squares symbols. Next, the engine was operated with a mass of m_{added} = 3.67g added to the top membrane. Experimental results for m_{added} = 3.67g are shown with circle symbols. In both cases, the amount of energy per cycle delivered to the engine was fixed at E=10mJ.

The effect of mass on the dynamic behavior of the engine is apparent. For the case with no mass added to the top membrane m_{added} = 0g, the velocity transfer function $U_{1\,k}$ /$Q_{1\,k}$ shows a broad plateau with a maximum value of $U_{1\,k}$ /$Q_{1\,k}$ = 2.5mm/s/W. No resonant peak is observed over the frequency range f =0.1-1000Hz. In contrast, for the case with mass m_{added} = 3.67g added to the top membrane, the velocity transfer functionU_{2k}/Q_{2k} does show a resonant peak, at the frequency f_n =130Hz. At that frequency, the amplitude of velocity transfer function U_{2k} /Q_{2k} reaches a maximum value of U_{k} /Q_{2k} =10mm/s/W. At the resonant frequency, adding mass increases the amplitude of the velocity transfer function by a factor of four. Away from the resonant frequency,

i.e. f_n=130Hz, adding mass to the expander membrane decreases the amplitude of the velocity transfer function. This decrease in amplitude is a consequence of the thermal inertia /storage associated with the mass added to the expander membrane.

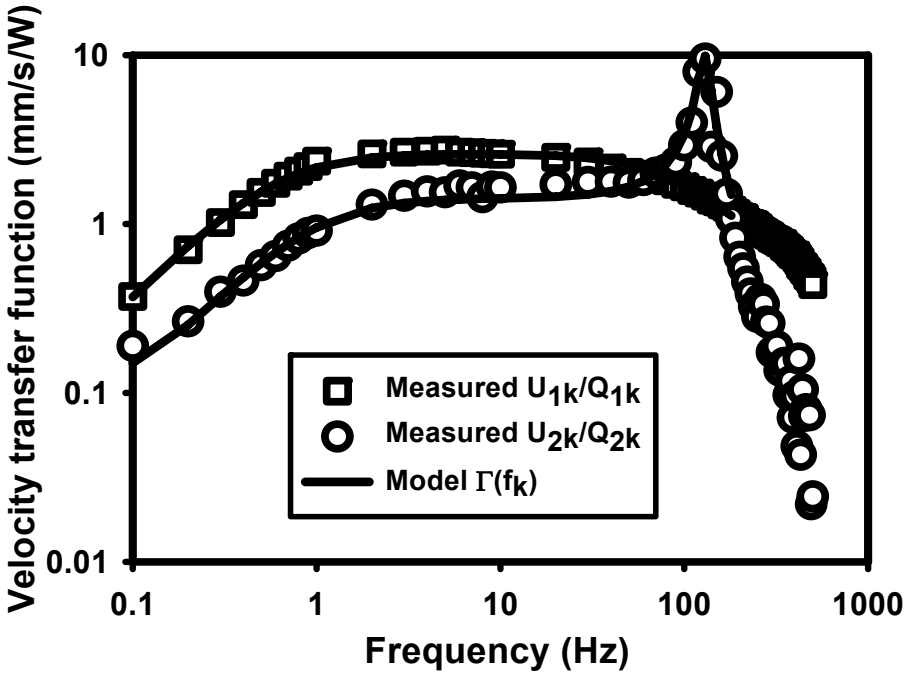

Figure 7.4: Effect of mass of top membrane on transfer function.

7.4.2 Effect of thermal storage on the dynamic behavior of the engine

The effect of thermal storage or thermal inertia associated with the engine cavity on the dynamic behavior of the engine is illustrated in Figure 7.5. The effect of the thermal inertia was varied by changing the contact area between the top membrane and the mass placed on top of it. Engine B in Table.7.1 was used to run the test. In one case, the high thermal inertia configuration, the mass added to the top membrane was in intimate contact with the membrane. In the second case, the low thermal inertia configuration, the mass added to the top membrane was thermally isolated from the membrane. Heat

(E=10mJ/cycle) was added to the engine for a duration T=1ms at a cycle frequency of f_o=10Hz. During these experiments, the thermal switch was used to control heat rejection from the engine. Due to the complexity of the heat rejection profile, formulation of the velocity transfer function was not possible. However, since heat addition and heat rejection processes were identical for both cases, engine performance in both cases may be compared on the basis of normalized transfer functions. This comparison was made by calculating the ratio between the outputs $U_1(f_k)/U_2(f_k)$, where $U_1(f_k)$ and $U_2(f_k)$ are the velocity spectra of the low thermal inertia and the high thermal inertia configurations, respectively.

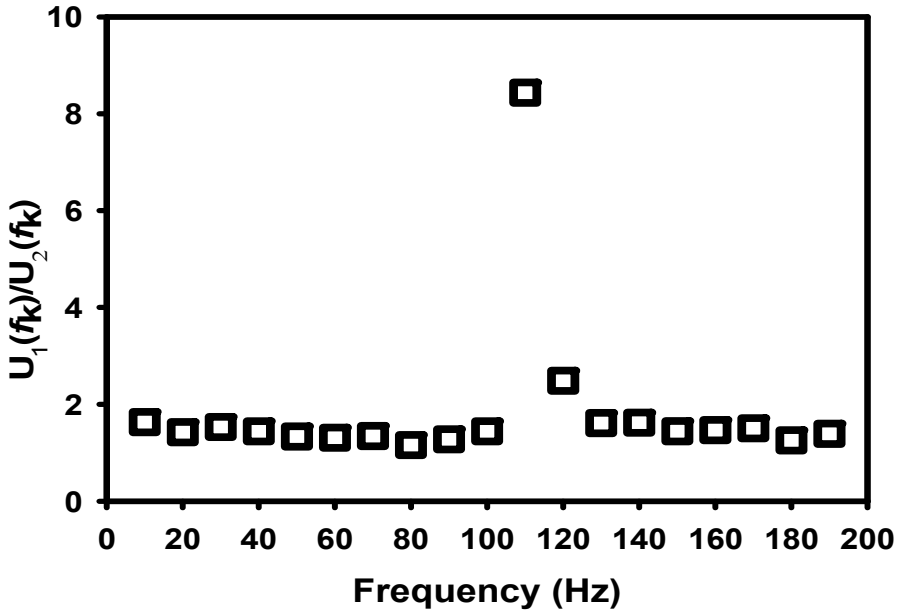

Figure 7.5: Effect of thermal inertia on velocity transfer function.

Figure 7.5 shows the output ratio $U_1(f_k)/U_2(f_k)$ for the low thermal inertia and the high thermal inertia configurations of the micro heat engine. The output ratio $U_1(f_k)/U_2(f_k)$) is seen to vary from approximately 1.5 away from the resonant frequency to 8.5 at the

resonant frequency. Thus, the amplitude of velocity transfer function increases by a factor of 1.5-8.5 when the mass added to the top membrane is thermally isolated from the engine.

7.4.3 Effect of duration of heat addition on the dynamic behavior of the engine

The duration of heat addition process is an important parameter in engine operation. Figure 7.6 shows the heat rate spectrum Q_K obtained from the FFT analysis of the heat rate $q(t)$ delivered to the engine, for heat addition processes of duration T =1 ms (circles), 10ms (squares) and 50ms (triangles). The overall period T_o for the heat rate $q(t)$ was T_o=100ms, giving duty cycles of 1%, 10%, and 50% corresponding to the durations of T=1, 10, and 50ms, respectively. The amount of heat delivered to the engine per cycle was fixed at E=10mJ.

Figure 7.6 reveals the existence of nonzero heat rate components Q_k at odd multiples of the engine cycle frequency f_o=1/T_o=10Hz for the heat addition process of duration T=50ms. The largest nonzero heat rate component Q_k occurs at a frequency f_1=10Hz and has an amplitude of Q_1=0.0771W. The amplitude of the components Q_k then declines rapidly as frequency increases. Likewise, for the heat addition process of duration T=10ms, the first component Q_1 has a magnitude of Q_1=0.147W. The magnitudes of the components at higher frequencies also decline but more slowly. Finally for the heat addition process of duration T=1ms, the amplitude of the components at higher frequencies decline very little from the amplitude of the first heat rate component Q_1=0.147W. The plot illustrates how, as the heat addition process duration lengthens, the amplitude of the heat rate components Q_k declines faster.

For appreciable power output, the heat rate spectrum Q_k must have significant magnitude within the bandwidth of the transfer function $\Gamma(f_k)$ of the engine. That is, the time-averaged power Π generated by the damper b can be computed with

$$\Pi = \frac{1}{2}\sum_k b|Q_k\Gamma(f_k)|^2 \quad . \tag{7.1}$$

The time-averaged power Π delivered to the load b is proportional to the square of the product of the heat rate and velocity transfer function $Q_k\Gamma(f_k)$ summed over the frequency spectrum. Thus, the nature of the heat rate spectrum Q_k will affect the power Π delivered to the load b. Thus, Figure 7.6 reveals that pulse duration less than 10% of the total engine cycle period T_o, is desirable.

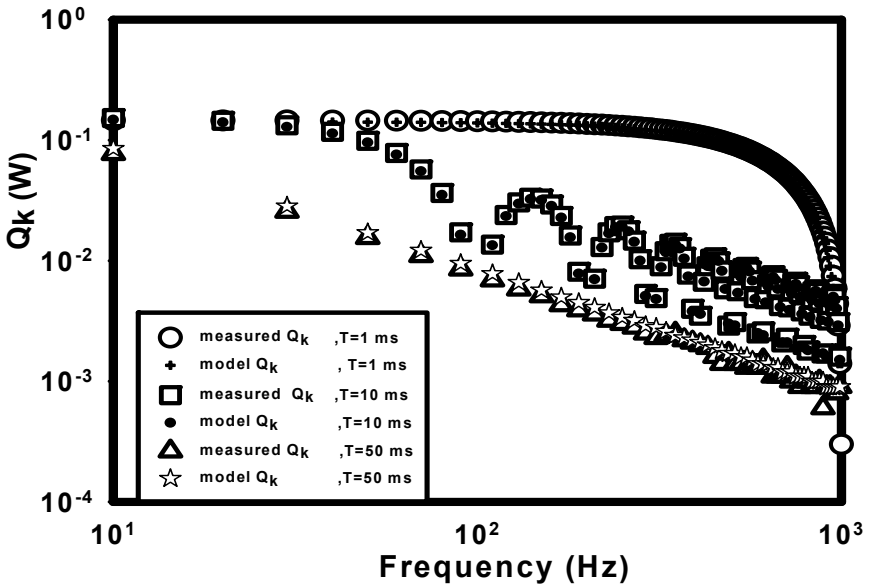

Figure 7.6. Effect of duration of heat addition process on the heat rate spectrum.

The effect of the duration of the heat addition process on engine A in Table 7.1 performance is also shown in Figure 7.7. In the figure, measured engine power output is

plotted versus heat addition duration. The figure shows results for an engine operated at f_o=10Hz with heat addition process durations of T=1ms to 50ms or duty cycles of 1% to 50%. The energy input per cycle was held constant at E=8mJ. The plot shows that shorter heat addition processes lead to greater engine power output. Thus, heat addition processes of 1ms to 10ms, or duty cycles of 1 to 10% lead to the highest engine power output.

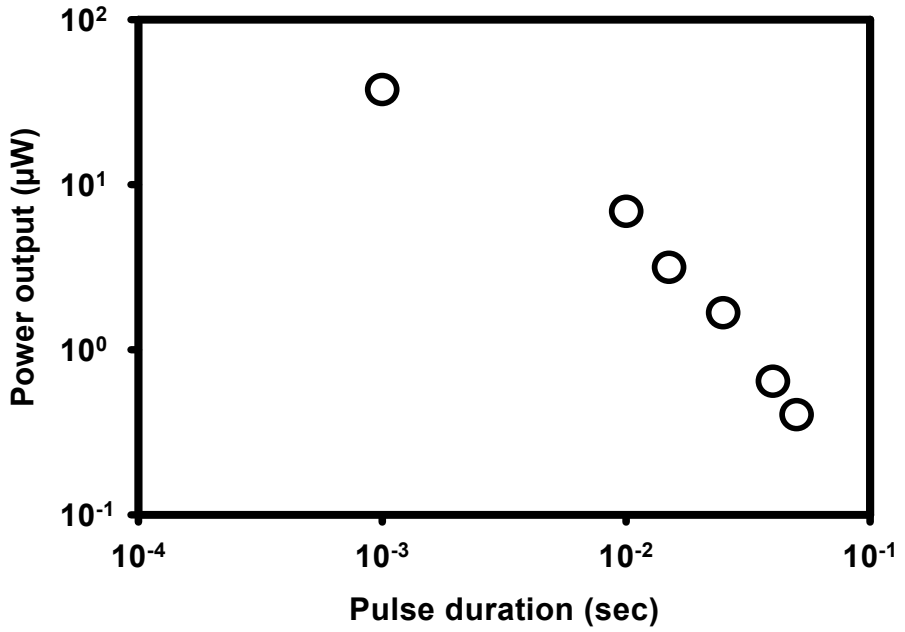

Figure 7.7: Effect of duration of heat addition process on power output.

Chapter 8

CYCLIC OPERATION OF THE MICRO HEAT ENGINE

8.1 Introduction

In this chapter, the operation of the micro heat engine through range of frequencies is presented. Similar geometry to engine B in Table 7.1 was used. The micro heat engine was integrated with the experimental setup shown in Figure 4.1. The chamber was filled with argon gas (thermal conductivity 17.7×10^{-3} W/m.K). The thermal switch was used for cooling the engine.

First, determining the resonant frequency of the micro heat engines is discussed. Next, the cyclic operation of the micro heat engine through a frequency spectrum is presented. Three operating frequencies were chosen. First, the operating frequency was set equal to the resonant frequency of the engine, i.e. resonant operation. Second, the operating frequency was set lower than the resonant frequency of the engine, i.e. sub-resonant operation. Lastly, the engine was operated at a super-resonant condition where the operating frequency of the engine was set to be higher than resonant frequency. In each test, deflections of both top and bottom membranes were measured. Pressure and volume changes inside the cavity are obtained using the techniques outlined in section 6.6. In addition to measured data, model predictions of pressure and volume changes inside the cavity of the engine are also presented. The pressure and volume changes are obtained by solving the linear set (5.16). The detailed MATLAB code used to generate the pressure-volume diagram for a specified heat input, $q(t)$ is in appendix D.

8.2 Determining resonant frequency of the engine

Although a similar geometry to engine B in Table 7.1 was used, the resonant frequency of an assembled engine may vary, even slightly, from one engine to another. That is for different engines with same geometry the initial deflection of the top membrane, the force exerted on top and bottom membranes upon assembly, and the size of the bubble inside the cavity may alter the resonant frequency of the engine. Because of this it is important to determine the resonant frequency of each individual engine separately before running a test. For the engine tested here, the size of the saturated-vapor bubble was $2r_i$=9mm. The cavity of the engine was filled with PF5060 working fluid. The wick structures on top of the bottom membrane were 5μm thick, 10μm high, and spaced 90μm apart. Once the engine was assembled a small mass was placed on top of the engine, m_{added} = 3.8g.

To examine the dynamic operation of the engine, the resonant frequency of the assembled engine was determined first. The engine was operated at frequencies f_o =0.1, 1.0 and 10.0Hz, respectively. The heat pulses were chosen to be T = 100, 10 and 1.0ms, respectively. The choice of these frequencies f_o and heat pulses T, allowed the collection of data in a frequency bandwidth of 0.1- 1000Hz. The amount of energy delivered to the engine through the resistance heater was E= 1.0mJ/cycle. In this test, care was taken to prevent the engine from heating up during the operation. Preventing the engine from heating up was crucial for this test. That is, when the engine heats up, the average temperature and pressure inside the cavity of the engine increase, thereby the top membrane bulges out and the neutral position of the top membrane shifts up. As a result, the top membrane stiffens up and the resonant frequency of the engine is altered. To

capture the exact resonant frequency of the engine, the engine must be protected from heating up. The choice of low input energy to the engine, i.e. E=1.0mJ/cycle, was meant to prevent the engine from heating up. In addition, the thermal switch was used for cooling of the engine constantly, thereby preventing the engine from heating up. The use of the thermal switch as a constant cooling source to the engine enabled direct comparison between the measured velocity transfer function and the modeled one. The resonant frequency of the engine was then determined by examining the velocity transfer function. Figure 8.1 shows both measured and modeled velocity transfer function of the engine. Velocity amplitude, in mm/s/W, is shown on the vertical axis while the frequency spectrum, in Hz, is shown on the horizontal axis. At resonant frequency, the velocity amplitude peaks at10mm/s/W. The resonant frequency of the engine was determined to be 110Hz. For this engine the quality factor was Q=8.5.

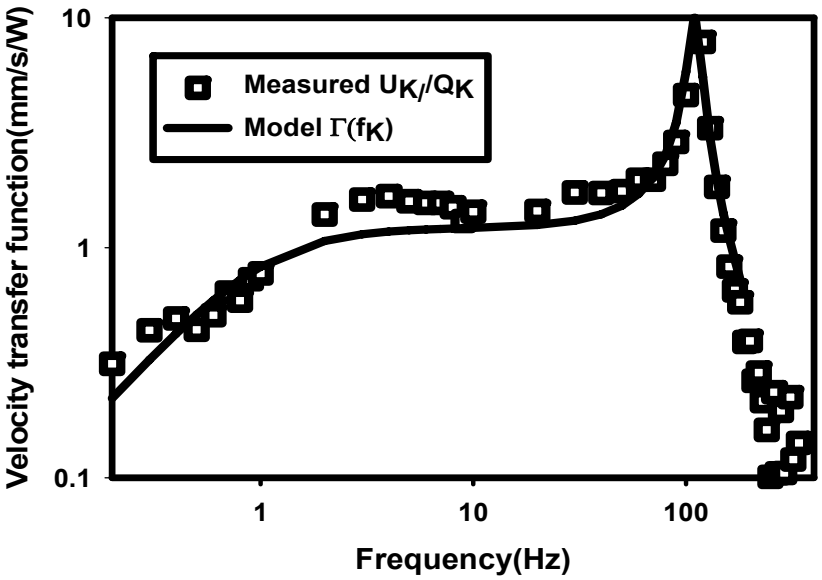

Figure 8.1: Velocity transfer function of micro heat engine, f_n=110 Hz.

8.3 Resonant, sub-resonant, and super-resonant operation of the engine

Once the resonant frequency of the engine was determined the engine was then operated at sub-resonant, i.e. f_o=90Hz, super resonant, i.e. f_o=130Hz and resonant frequency, i.e. f_o.= f_n =110Hz. For the resonant operation, the heat was input over 1% duty cycle. The amount of energy delivered to the engine per cycle was fixed at E=1.0 mJ. The voltage across the resistance heater, and the deflections of the top and bottom membranes were measured during the test. Figure 8.2 shows the deflection of top and bottom membranes, in micrometers, on the vertical axis versus time, in sec, on the horizontal axis. For the specified operating conditions, Figure 8.2 shows that the peak-peak deflections of the top and bottom membranes were 12 and 4μm respectively.

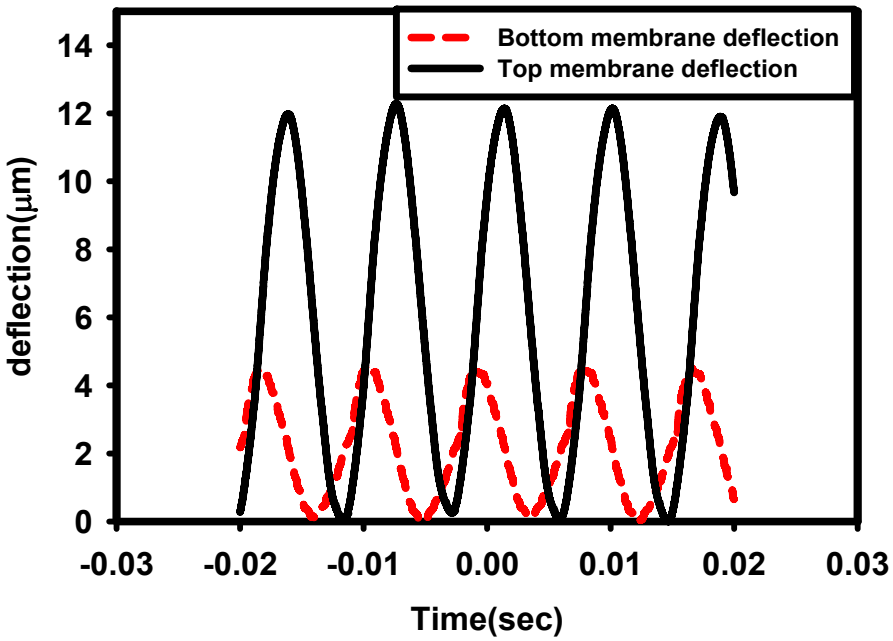

Figure 8.2: Deflection of top and bottom membranes at resonance, f_o=f_n=110 Hz.

Figure 8.3 shows measured pressure and volume changes inside the cavity versus time. Volume and pressure changes are obtained from the deflections of the top and the bottom membranes using (6.14) and (6.15), respectively. The volume and pressure changes are indicated by the solid heavy line and the dashed line, respectively. The maximum pressure rise and volume change inside the cavity were 62Pa and 0.59mm^3, respectively. At resonance, the pressure and volume in the engine cavity cyclically rose and fell 90 degrees out of phase.

Figure 8.4 plots the PV diagram of the engine operated at 110Hz. In Figure 8.4 volume changes and pressure changes inside the engine cavity are plotted on the horizontal axis and vertical axis, respectively. Both measured and modeled PV diagrams are shown. Table 8.1 summarizes the floating parameters used to fit the model to experimental PV diagram. Experimental measurements are indicated by the dashed line while the predictions are shown with a solid line. The engine cycle describes a closed loop. The PV diagram is bounded by two constant pressure and volume processes. The pressure and volume changes inside the cavity are decoupled. Fair agreement between model prediction and measured data is observed.

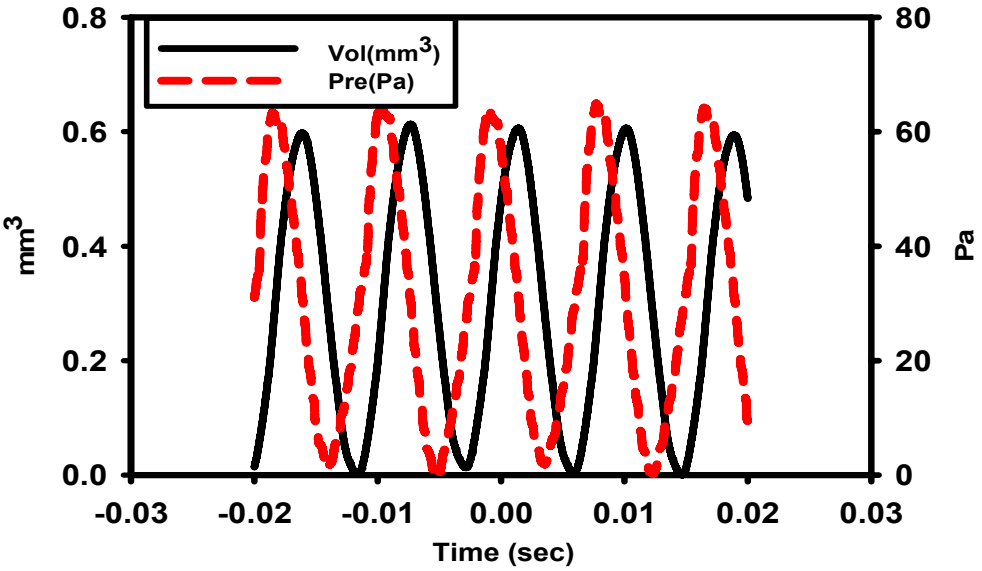

Figure 8.3: Pressure and volume at resonance, $f_o = f_n$=110 Hz.

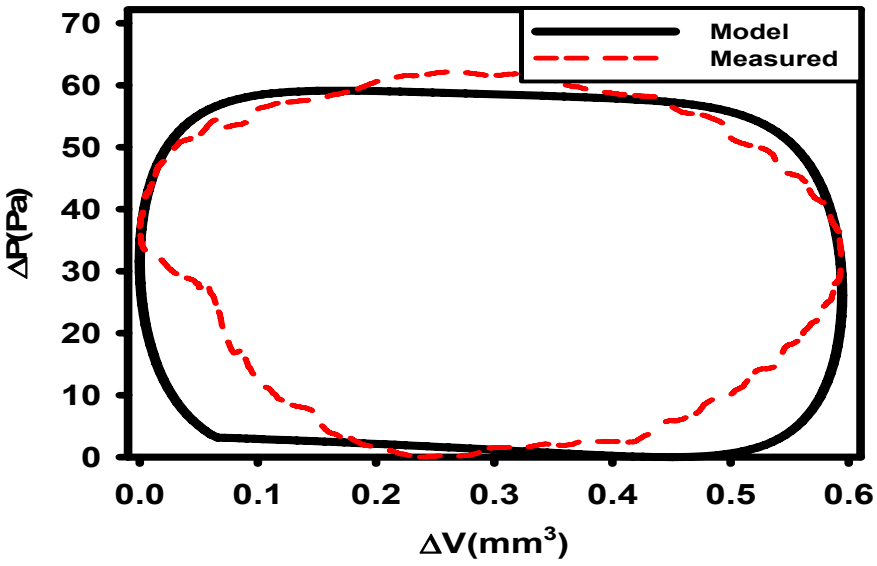

Figure 8.4: PV diagram at resonance, $f_o = f_n$=110 Hz.

Table 8.1. Floating parameters used in the model.

C_T(J/k)	0.026
b_f(N.s/m)	0.8
U_B(W/K)	1.87×10^{-4}
$m + \overline{m}$ (kg)	4.8×10^{-3}
U_c(W/K)	0.16

The operation of the micro heat engine at sub-resonant condition, i.e. f_o= 90Hz is examined in Figures 8.5, 8.6 and 8.7. The heat was input over a 1% duty cycle, i.e T=0.11ms. The amount of energy delivered to the engine per cycle was fixed at E=1.0mJ. Figure 8.5 shows the deflections of the top and bottom membranes, in micrometer, versus time, in sec. The peak-peak deflections of the top and bottom membranes were 2.5 and 1.5μm, respectively.

Figure 8.6 shows the pressure and volume changes inside the cavity of the engine versus time. The maximum pressure rise and volume change inside the cavity were 27Pa and 0.28mm^3, respectively. Unlike resonant operation, pressure and volume changes inside the cavity were coupled. Figure 8.7 plots the pressure changes, in Pa, on the vertical axis versus the volume changes inside the cavity, in mm^3, on the horizontal axis. Both measured and modeled pressure and volume changes are shown in Figure 8.7. Experimental measurements are indicated by the dashed line while the model predictions are shown with a solid line. The PV diagram describes a sigmoidal shape in contrast to the elliptical PV diagram shape at the resonant condition.

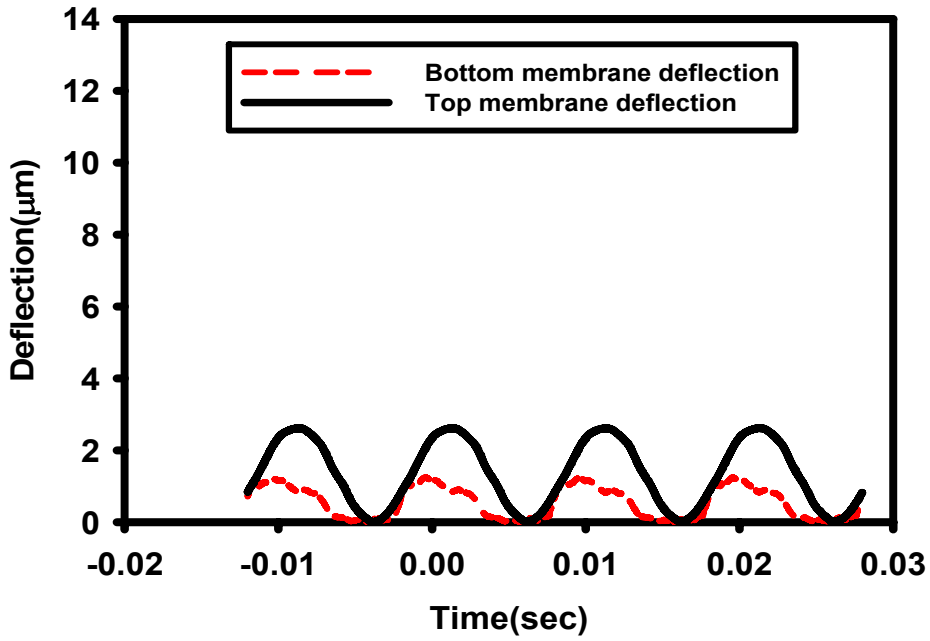

Figure 8.5: Deflection of top and bottom membranes, f_o=90Hz.

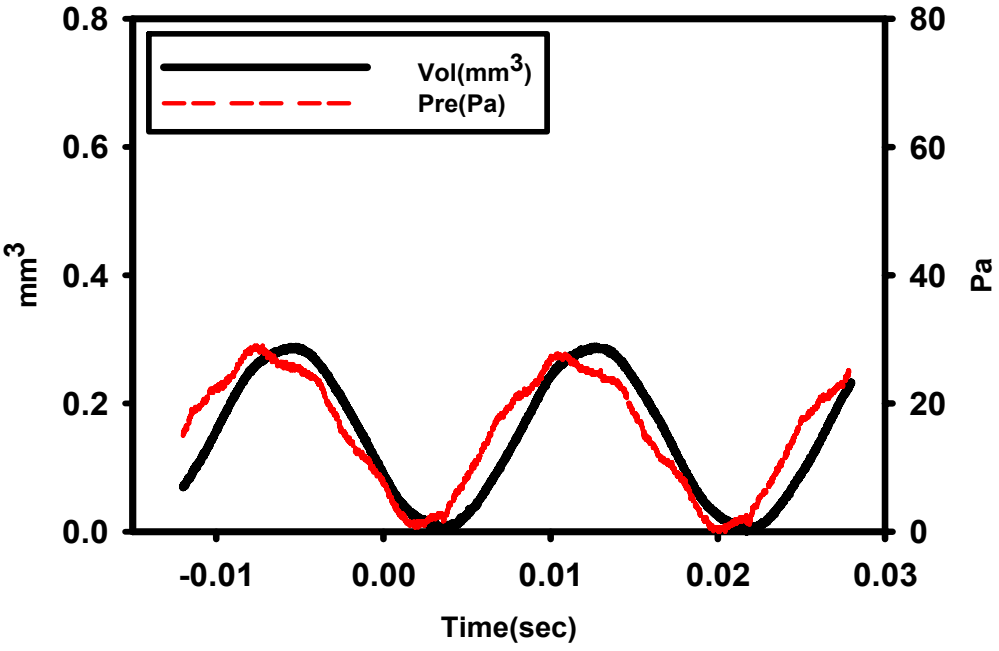

Figure 8.6: Pressure and volume time history at sub-resonance, f_o= 90 Hz.

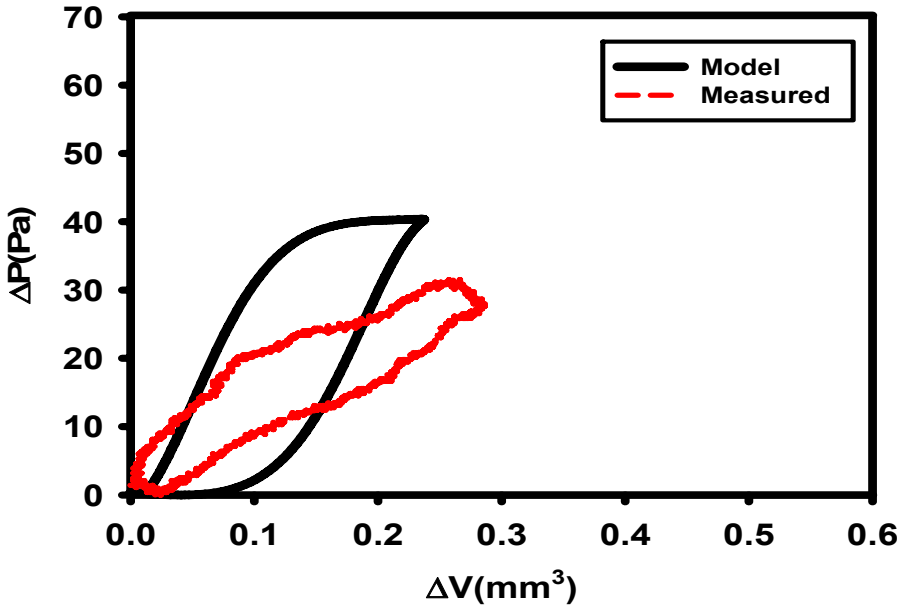

Figure 8.7: PV diagram at sub-resonance f_o =90 Hz.

Next, the engine was operated at super-resonant condition, i.e. f_o=130Hz. Figure 8.8 plots the time history of the deflections of the top and bottom membranes. The peak-peak deflections of the top and bottom membranes were 5 and 1.2 μm, respectively. Figures 8.9 shows pressure, in Pa, and volume changes, in mm^3, versus time. The heat was input over a 1% duty cycle,. The amount of energy delivered to the engine per cycle was fixed at E=1.0mJ. The maximum pressure rise and volume change inside the cavity were 19Pa and 0.29mm^3, respectively. Figure 8.10 shows the PV diagram of the engine operated at the super-resonant condition, i.e. f_o=130 Hz. Experimental measurements are indicated by the dashed line while the model predictions are shown with a solid line. Like the sub-resonant operation, pressure and volume changes inside the cavity are coupled. The shape of the PV diagram describes a sigmoidal curve. However, unlike the sub-resonant PV diagram, the sigmoidal PV diagram is reversed. That is for a super-

resonant operation, the maximum pressure is observed when the volume is minimum. However, the maximum volume and pressure are both observed at the same point when the engine is operated at sub-resonant conditions.

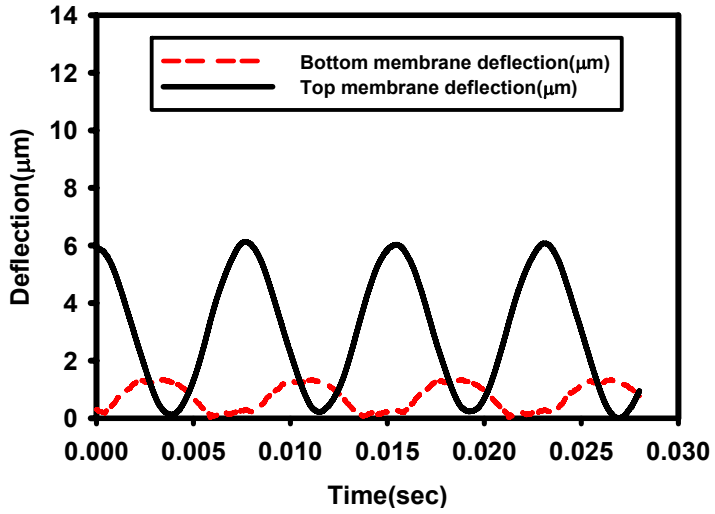

Figure 8.8: Deflections of top and bottom membranes at super-resonance, f_o=130Hz.

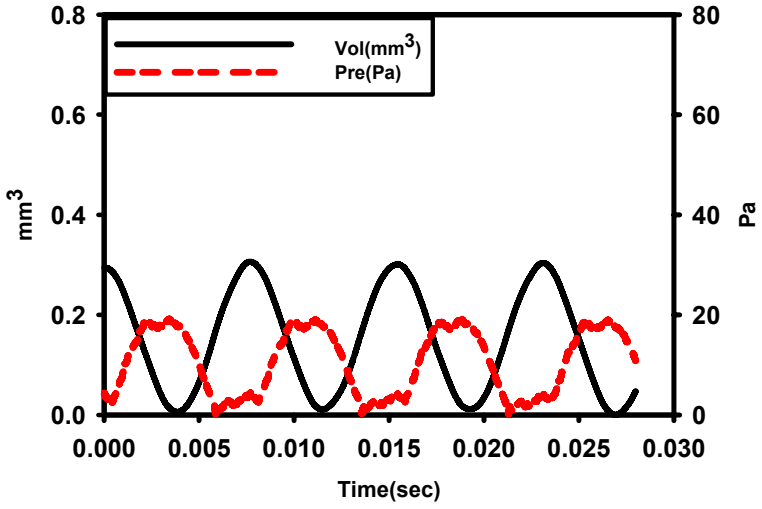

Figure 8.9: Pressure and volume time history at super-resonance, f_o =130Hz.

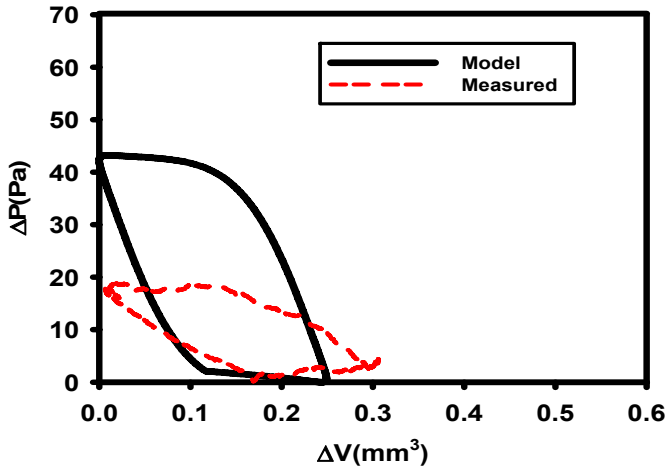

Figure 8.10: PV diagram at super-resonance, f_o =130Hz.

In Figures 8.7 and 8.10 some discrepancy between model predictions and measured data was observed. That is, the model over-predicted the PV diagrams at 90 and 130 Hz operations. A plausible explanation is that the engine parameters, and engine natural frequency and resonance quality factor may drift slightly between measurements, perhaps due to accumulated heating. Even though there was some discrepancy between model and measured data, a general agreement between model predictions of PV diagrams and measured data, at 90 and 130 Hz, was observed. The model PV diagrams show the same characteristics as the measured ones. The shapes of the model PV diagrams are in favorable agreement with the shapes of measured PV diagrams. That is, the model predicted sigmoidal PV diagrams for a sub-resonant and a super-resonant operation, i.e. 90 and 130Hz respectively, which is consistent with what is observed experimentally. Moreover, the model PV diagram "flips over" when the condition was changed from a

sub-resonant operation to a super-resonant operation, i.e. 90 and 130 Hz respectively. The same characteristic was observed experimentally.

Figures 8.2-8.10 reveal that resonant operation of the engine is beneficial. The mechanical work of the engine, represented by the area inside the curve, is maximized at resonant frequency, i.e. $f_{o=}$. f_n =110Hz. The PV diagram opens up as we move toward resonance. The engine cycle describes a closed loop. Pressure and volume changes inside the cavity are decoupled. When the engine is operated at off-resonant conditions, i.e. f_o =90 and f_o =130Hz, the pressure and volume changes are significantly reduced. The area inside PV diagram becomes smaller and less mechanical work is observed. For any off-resonant operation, the shape of the PV diagram reveals that variation in volume is accompanied by pressure variation.

To shed more light on both off-resonant and resonant operation of the engine, the mechanical work done by the engine is next examined. Figure 8.11 plots the mechanical work, in Pa.mm^3, on the vertical axis versus the operating frequency, in Hz, on the horizontal axis. Both measured and model predictions of mechanical work are shown for the operating frequencies f_o =90, 110, and 130Hz. The mechanical work at 90, 110 and 130Hz is estimated by numerically integrating the area inside the PV diagrams. The model is then used to predict the PV diagram at a wider range of frequencies, i.e. 10-200Hz.

Figure 8.11 reveals the importance of matching the operating frequency of the engine to the resonant frequency. The mechanical work of the engine is maximized when the operating frequency is set equal to the resonant frequency of the engine. As the operating frequency of the engine is moved away from the resonant frequency, the mechanical

work becomes less. More specifically, the mechanical work done by the engine was reduced by a factor of 10 when the operating frequency was 20Hz off-resonance i.e. f_o=90 and f_o =130Hz respectively. This observation emphasizes the importance of matching the operating frequency to the resonant frequency of the engine. Special attention is paid for characterization of resonant cycle of the micro heat engine in chapter 9.

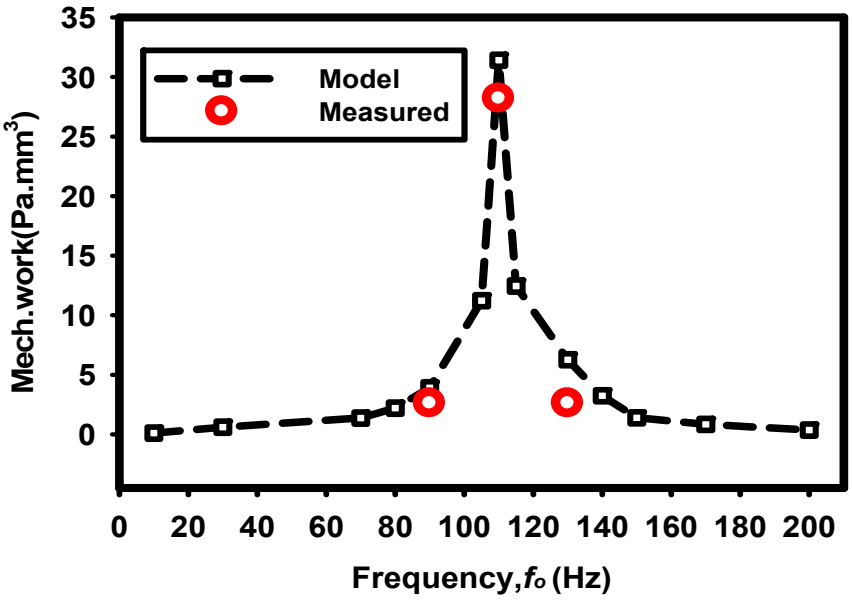

Figure 8.11: Mechanical work done by the micro engine.

Chapter 9

RESONANT CYCLE OF THE MICRO HEAT ENGINE

9.1 Introduction

It is concluded from the discussion in the previous chapters that resonant operation of the micro heat engine is desirable and beneficial. Characterizing the resonant cycle of the micro heat engine was identified as a primary goal of this work. The focus of this chapter, then, is the resonant operation of the micro heat engine. In this chapter, the thermodynamic cycle of the engine is discussed in detail. Resonant operation of the engine in air, argon, and xenon mediums is discussed next. Then, the effect of input energy per cycle, E delivered to the engine, on its performance is detailed. The performance of the micro heat engine is also documented. For performance measurements, the mechanical work done by the engine and thermal efficiency are presented and compared to the Carnot efficiency. The cycle of the engine is investigated in terms of vapor pressure, vapor volume, vapor temperature, and vapor entropy variation inside the cavity of the engine. Pressure and volume changes inside the cavity are calculated using the procedure outlined in section 6.6.1. Temperature and entropy changes are calculated using the methodology discussed in section 6.6.3. The pressure-volume and temperature-entropy diagrams of the micro heat engine are then constructed.

9.2 Resonant operation of the micro heat engine

The engine used in this test had similar geometry to engine B in Table 7.1. The vapor bubble covered 90% of the bottom membrane size. The cavity of the engine was filled

with PF5060 working fluid. The wick structure, on top of the bottom membrane was 5μm thick, 10μm high, and spaced 90μm apart. A small mass was placed on top of the engine, m_{added}= 3.67g. The resonant frequency of the engine was determined to be f_n=130Hz. The engine was operated at frequency f_n= f_o=130Hz. The thermal switch was used to remove heat from the engine. The energy was delivered to the engine, electrically, through a resistance heater. The energy input to the engine was, E=1.0mJ/cycle. The gap between thermal switch and bottom membrane was filled with air at atmospheric pressure.

Figure 9.1 shows both transient and steady state deflections of the top membrane. The transient response of the engine was recorded right after the heat was input into the engine. The engine was then kept running, while the energy was constantly going into the engine, until steady state conditions were reached. As shown in the figure, the measured peak-peak deflection went down from 18μm right after the heat was input into the engine to 4μm at steady state conditions. This observation reflects the poor performance of the thermal switch in this experiment. As the operation of the engine continued, less energy was rejected from the engine and heat was accumulated inside the engine. That is, the thermal switch was not capable of rejecting the same amount of energy that was input to the engine. Thereby, the average temperature and pressure inside the cavity of the engine increased and the engine heated up.

Figure 9.2 shows the deflection of the bottom membrane at transient conditions. For this experiment, the deflection of the bottom membrane at steady state conditions was not measured. From the deflections of the top and bottom membranes, volume and pressure changes were obtained, respectively. Figure 9.3 shows pressure-volume diagram of the

engine at transient condition. The maximum pressure rise and volume changes inside the cavity were ΔP=40Pa and ΔV =0.9 mm^3, respectively.

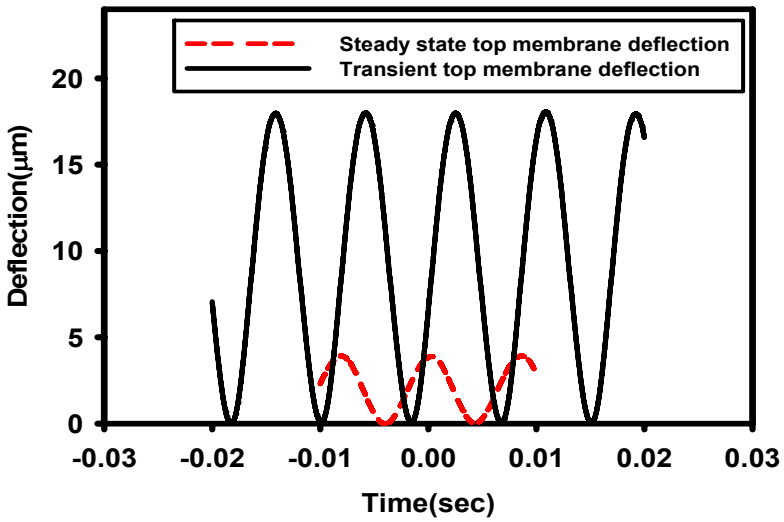

Figure 9.1: Transient versus steady state top membrane deflection f_n=130Hz.

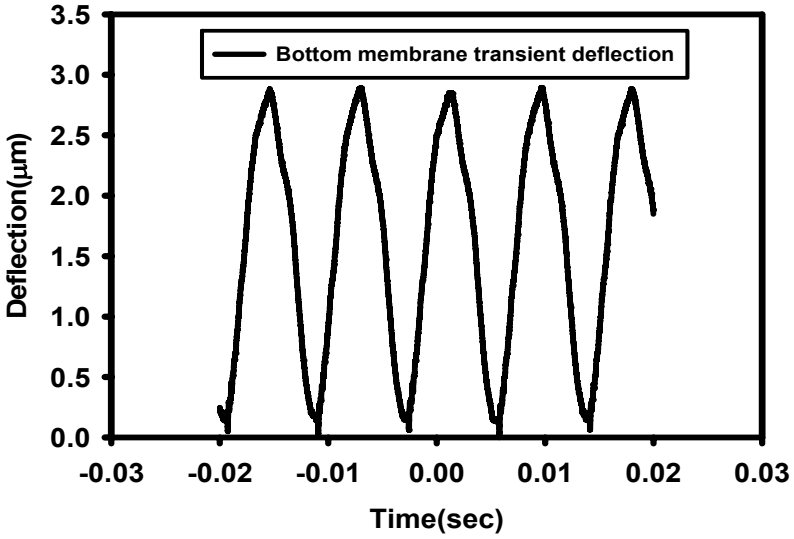

Figure 9.2: Bottom membrane transient deflection, f_n=130Hz.

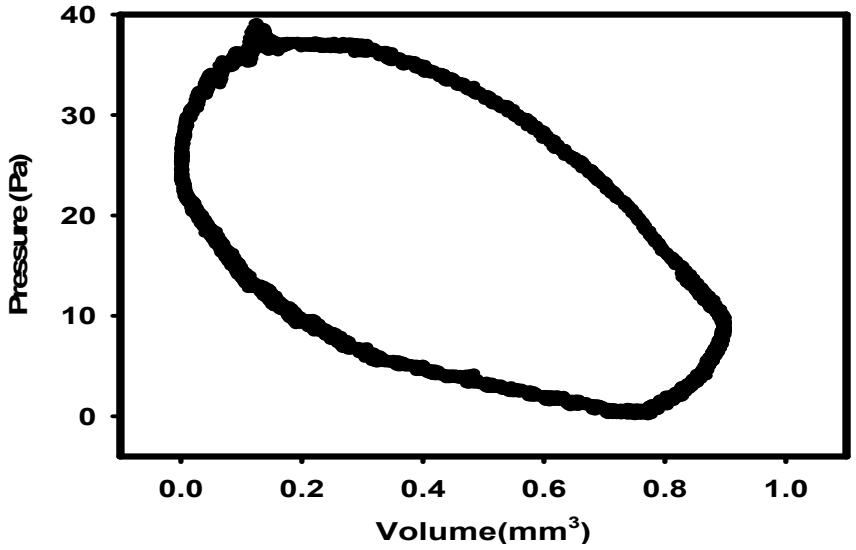

Figure 9.3: PV diagram at transient condition, f_n =130 Hz.

9.3 Characterization of the thermodynamic cycle of the resonant micro heat engine

The cycle of the micro heat engine is examined next. In the experiment, the resonant frequency of the engine was determined to be, f_n=115Hz. Input energy per cycle, delivered to the bottom membrane, was E=1.0mJ and it was delivered with a 1% duty cycle. The thermal switch, controlling heat rejection, was maintained at 4^{o}C during the operation of the engine. The experiment was carried out at room temperature, T_o=294K. Upon operation of the engine, air inside the chamber was replaced with argon gas. The cavity of the engine was filled with PF5060 working fluid. The wick structure, on top of the bottom membrane, was 5μm thick, 10μm high, and spaced 90μm apart. The bubble covered 90% of the heater size. A small mass was placed on top of the engine, m_{added} = 3.9g. The energy was delivered to the engine, electrically, through a resistance heater.

The saturation pressure of the two-phase mixture inside engine cavity is P_{sat}=25351Pa gage at room temperature T_o=294K.

Figure 9.4 shows the time history of pressure and volume inside the engine cavity. Also, shown in Figure 9.5 is the time history of both power input to the engine and displacement of the thermal switch. In Figure 9.5 the input power, in Watts, delivered to the bottom membrane (through the electrical resistance) is plotted on the left vertical axis. The displacement of the thermal switch is plotted on the right vertical axis. As the thermal switch moves from its initial position (0μm) to its final position (80μm) it closes the gap between the liquid-metal micro-droplet array and bottom membrane and thus heat rejection takes place. As a result, heat is conducted away from the engine (higher temperature) to the thermal switch (lower temperature). Figures 9.4 reveals that pressure and volume in the engine cavity are decoupled and true cycle work is produced.

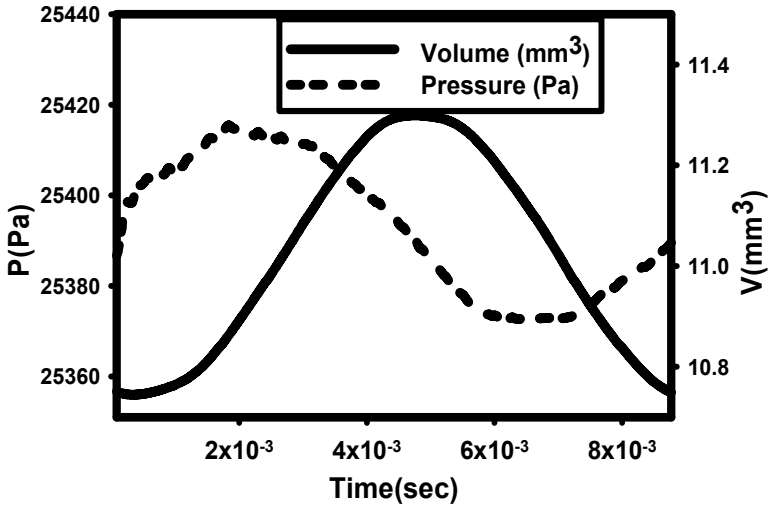

Figure 9.4. Pressure and volume- time history at resonance, f_n=115Hz.

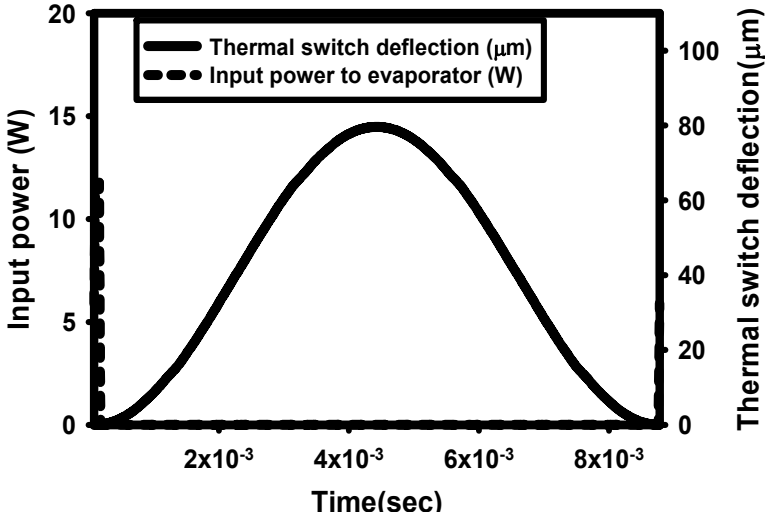

Figure 9. 5. Power input to the engine and deflection of the thermal switch-time history.

Pressure-volume and temperature-entropy diagrams are shown in Figure 9.6 and 9.7, respectively. First, heat is added, through the bottom membrane, to the engine. Heat addition causes the layer of liquid held in the wicks to evaporate. The evaporated mass enlarges the bubble, causing a pressure and temperature rise inside the cavity. Pressure rise inside the cavity causes the bubble to push against the top membrane. Consequently, the top membrane flexes out and the expansion process takes place. Once expansion is complete and the top membrane reaches its maximum deflection point, the thermal switch makes contact with the bottom membrane enabling heat to be conducted away from the engine. That is, when heat is removed from the engine, through the cold thermal switch, vapor condenses back onto the bottom membrane. During resonant operation of the engine, energy is stored in the flexing top membrane as a result of the expansion process. Next, this energy stored in the top membrane causes the membrane to

flex in, compressing the working fluid. At the end of the compression process the working fluid returns to its initial state and the cycle is repeated.

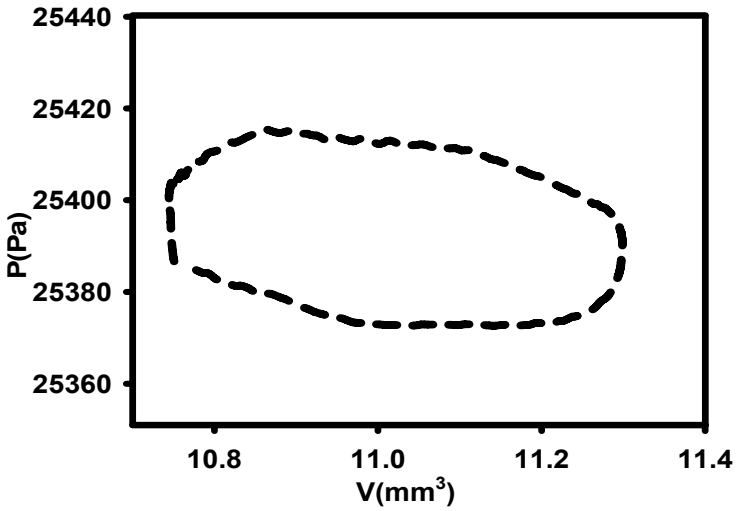

Figure 9. 6. Pressure-volume diagram at resonance, f_n =115Hz.

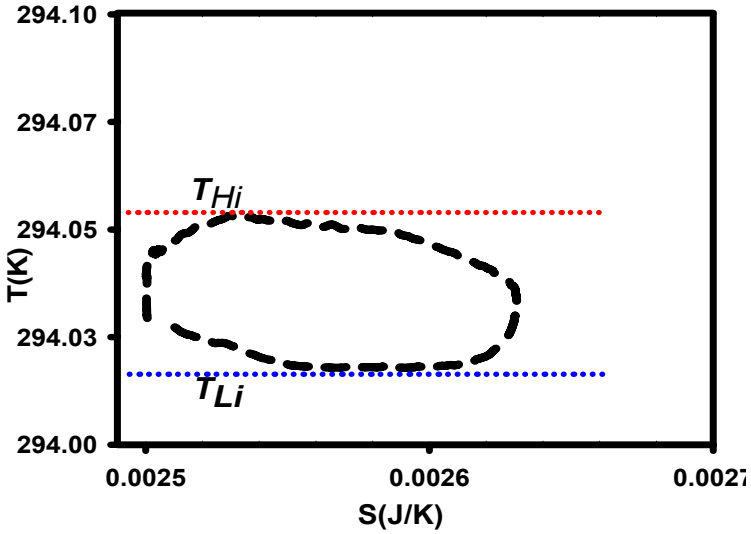

Figure 9.7. Temperature-entropy diagram at resonance, f_n =115Hz.

Engine irreversibility is thought to come from three major sources: (1) Entropy production due to the finite temperature differences required to drive heat transfer during heat addition and rejection (2) Entropy production due to heat transfer into and out of thermal storage in the engine, and (3) Entropy production due to viscous losses in the liquid working fluid surrounding the vapor bubble. The first mechanism, entropy production due to heat transfer into and out of the engine, is a consequence of the fact that the engine is an external combustion device. The second mechanism, entropy production due to heat transfer into and out of thermal storage is a consequence of the resonant operation of the engine with its periodic heat addition and rejection processes. Finally, the third mechanism, entropy production due to viscous losses is a consequence of the motion of the liquid working fluid as the membrane flexes in and out. Thus, heat transfer between engine components and external heat source/sinks contribute to the external irreversibility of the engine, while viscous effects contribute to the internal irreversibility of the engine. Both external and internal irreversibility lower the performance of the engine and cause loss in the available work.

The cycle mechanical work is represented by the area inside pressure-volume and temperature-entropy diagrams. The maximum pressure rise and volume change inside the cavity were 45Pa and 0.55mm^3, respectively. For these conditions the engine was operating over a very small temperature difference, on the order of 1K. The mechanical work produced by the micro engine in one cycle was 0.018μJ. The first law efficiency of the micro heat engine was very small 0.0018%. However, the second law efficiency of the micro heat engine was about 16%.

9.4 Variation of input energy delivered to the micro heat engine

The goal of this test was to operate the micro heat engine at optimum condition and thereby maximize the output mechanical work of the engine. The engine used in this test had a similar geometry to engine B in Table 7.1. Because of its low thermal conductivity (5.65×10^{-3}W/m.K), xenon was used to fill up the gap between thermal switch and engine. The vapor bubble covered 95% of the bottom membrane size. The cavity of the engine was filled with PF5060 working fluid. The wick structure, on top of the bottom membrane was 5μm thick, 40μm high, and spaced 70μm apart. This wick design was shown to be the optimum design for the micro-channels [42]. A concentric mass was placed on top of the engine, m_{added}= 3.9g. The resonant frequency of the engine was determined to be, f_n=83Hz.

To determine the optimum input energy level, the energy per cycle delivered to the engine, E was varied gradually while the engine was operated at resonance, i.e. f_o=f_n=83Hz. Figure 9.8 shows the deflection of the top membrane measured at different energy levels, E. The maximum pea-peak deflection of the top membrane was 15μm, occurred at E=4.2mJ/cycle. Thus, the optimum energy is determined to be E=4.2mJ/cycle. When optimum energy is delivered to the micro heat engine, enough energy is available to evaporate the liquid layer in the micro-channels before drying out. For energy levels E=1.0 and 3.4mJ/cycle, the peak-peak deflections were 7.74μm and 14.1μm, respectively. Increasing the energy level from E=4.2mJ/cycle to E=6.0mJ/cycle did not increase the peak-peak deflection of the top membrane. That is, the peak-peak deflection at E=6.0mJ/cycle was 13.7μm.

Figures 9.9 shows pressure-volume diagrams of the engine. The figure compares the diagrams obtained at two different energy levels i.e. E=3.4 and 4.2mJ/cycle. The peak-peak pressure variations inside the cavity were ΔP=93Pa and 71Pa at energy levels E=4.2mJ/cycle and 3.4mJ/cycle, respectively. The peak-peak volume variations inside the cavity were ΔV=0.75mm^{3}and 0.703mm^{3}at energy levels E=4.2mJ/cycle and 3.4mJ/cycle, respectively. The maximum temperature variations inside the cavity were ΔT=0.078^{o}C and 0.06^{o}C at energy levels E=4.2mJ/cycle and 3.4mJ/cycle, respectively. The thermal efficiencies achieved were 0.00105% and 0.00101% at energy levels E=4.2mJ/cycle and 3.4mJ/cycle, respectively. Those thermal efficiencies represented 4% and 5% of Carnot efficiencies at energy levels E=4.2mJ/cycle and 3.4mJ/cycle, respectively.

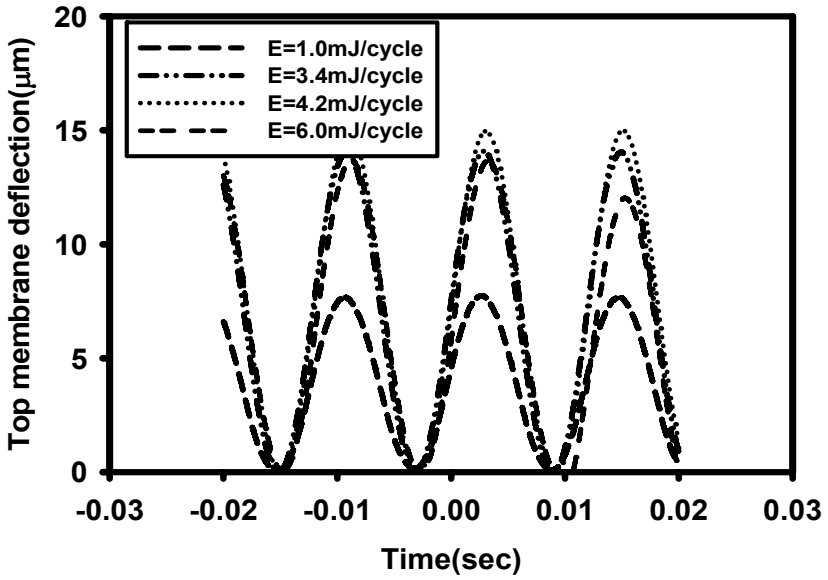

Figure 9.8: Deflection of top membrane at different energy levels, E, f_o=f_n=83Hz.

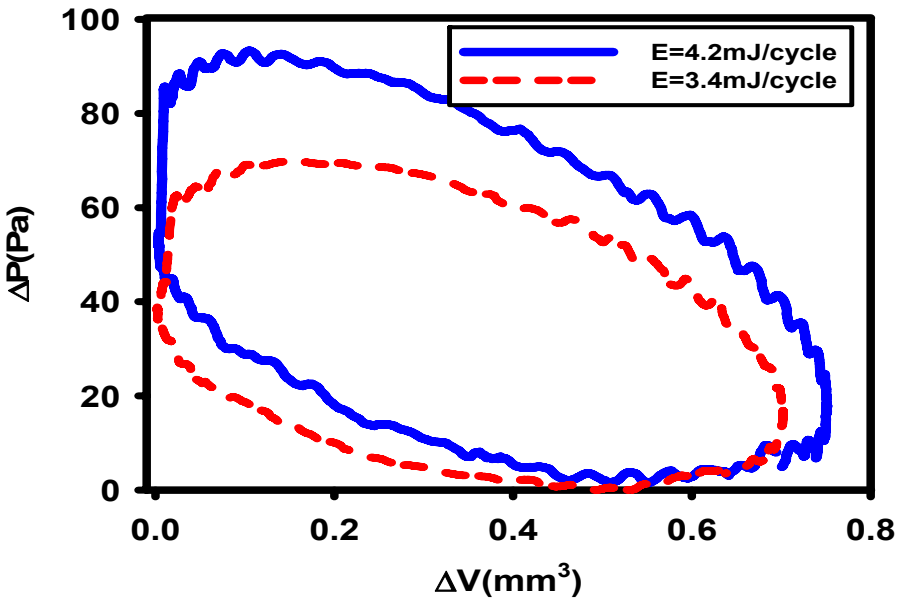

Figure 9.9: PV diagram at resonance, $f_o = f_n$ =83Hz.

Chapter 10

CONCLUSIONS

The operation of the MEMS-based resonant micro heat engine has been investigated. Both model and experiment were used to investigate the operation of the micro heat engine. In the experiment, heat was added to the engine using electrical resistance. Heat was conducted away from the engine using the thermal switch. Integration between the thermal switch and engine directly affects the overall performance of the engine. To improve the action of the thermal switch, a new experimental setup was built. The new setup allowed replacing the air, filling the gap between thermal switch and engine, with low thermal conductivity gas. A low thermal conductivity gas reduced heat leakage from the engine to the surroundings when thermal switch was in "off "position. Also, the new setup improved alignment between thermal switch and engine. Improved alignment enhanced heat transfer from the engine to the thermal switch during heat rejection event. The setup also reduced the vibration transmitted from the thermal switch to the engine. Thereby, deflection measurements of the top and bottom membranes were more robust.

A mathematical model of the engine was obtained by applying conservation laws, for both mass and energy, to the vapor bubble and liquid film above the bottom evaporator membrane. Newton's laws were applied to the motion of the top and bottom membranes. The model of the engine was validated against experimental data.

The effect of mass of the top expander membrane was investigated using a combination of experiments and model. The engine was operated in two modes. First, it was operated with no mass, and then a concentric mass was placed on top of the expander

membrane. The effect of mass on the dynamic behavior of the engine was apparent. For the case with no mass added to the expander membrane, the velocity transfer function showed a broad plateau with a maximum value of 2.5mm/s/W. No resonant peak was observed over the frequency range f =0.1-1000Hz. In contrast, for the case with mass added to the expander membrane the velocity transfer function showed a resonant peak in the order of 100Hz. At that frequency, the amplitude of velocity transfer function reached a maximum value 10mm/s/W. At the resonant frequency, adding mass to the top expander membrane increased the amplitude of the velocity transfer function by a factor of four. The effect of duration of heat addition, and thermal storage associated with the engine cavity on the dynamic behavior of the engine were also examined. The results show that the optimal heat addition pulse was less than 10% of the engine cycle period. Also, the results showed that thermal storage in the engine was detrimental to performance and should be minimized.

The operation of the micro heat engine at resonant conditions was investigated. Both pressure-volume and temperature-entropy diagrams have been used to characterize the thermodynamic cycle of the engine. First, heat is added, through the bottom membrane, to the engine. Heat addition causes the layer of liquid held in the wicks to evaporate. The evaporated mass enlarges the bubble, causing a pressure and temperature rise inside the cavity. Pressure rise inside the cavity causes the bubble to push against the top membrane. Consequently, the top membrane flexes out and the expansion process takes place. Once expansion is complete and the top membrane reaches its maximum deflection point, the thermal switch makes contact with the bottom membrane enabling heat to be conducted away from the engine. When heat is removed from the engine,

through the cold thermal switch, vapor condenses back onto the bottom membrane. During resonant operation of the engine, energy is stored in the flexing top membrane as a result of the expansion process. Next, this energy stored in the top membrane causes the membrane to flex in, compressing the working fluid. At the end of the compression process the working fluid returns to its initial state and the cycle is repeated. Major sources of irreversibility in the engine are heat transfer over finite temperature differences during heat addition and rejection, heat transfer into and out of engine thermal mass and viscous losses due to liquid working fluid motion. The maximum pressure and volume changes measured inside engine cavity are 45Pa and 0.55mm^3, respectively. The measured second law efficiency of the micro heat engine is about 16%.

The engine was, also, operated at sub-resonant and super-resonant conditions. For both conditions, i.e. sub-resonant and super-resonant conditions, the pressure and volume became coupled. The pressure-volume diagram described a sigmoidal shape. The data show that resonant operation is valuable. When the engine was operated at off-resonant conditions, pressure and volume changes were significantly reduced. The area inside PV diagram became smaller and less mechanical work was observed. For an off-resonant operation, the shape of the PV diagram revealed that variation in volume was accompanied by variation in pressure.

BIBLIOGRAPHY

[1] Jacobson S and Epstein A 2003 An informal survey of PowerMEMS *Proc. ISMME2003*

[2] Epstein A *et al.* 1997 Micro heat engines, gas turbines, and rocket engines-The MIT microengine project *Proc. 28th AIAA Fluid Dynamics and Fourth AIAA Shear Flow Control Conf 1997* (Snowmass Village, CO, July 1997)

[3] Fu K, Knobloch A J, Martines F C, Walther D C, Fernandez-Pello C, Pisano A P and Liepmann D 2001 Design and fabrication of a silicon-based MEMS rotary engine *Proc. ASME Int Mech. Eng, Congress and Expo.* (New York, 11–16 Nov) Paper No: IMECE2001/MEMS-23925

[4] Symko O G, Abdel-Rahman E, Kwon Y S, Emmi M and Behunin R 2004 Design and development of high-frequency thermoacoustic engines for thermal management in microelectronics *Microelectronics J.* **35 (2)** p 185-91 doi:10.1016/j.mejo.2003.09.017

[5] Herrault F, Crittenden T, Yorish S, Birdsell E, Glezer A and Allen M A 2008 Self-resonant, MEMS-fabricated, air-breathing engine *Proc. Solid-State Sensors, Actuators and Microsystems Workshop* 2008 (Hilton Head Island, South Carolina 2008) p 348-51

[6] Toriyama T, Hashimoto K and Sugiyama S 2003 Design of a resonant micro reciprocating engine for power generation *Proc. Transducers'03*(Boston, MA, June 2003)

[7] Schaevitz S, Franz A, Jensen K and Schmidt A 2001 A combustion-based MEMS thermoelectric power generator *Proc. Digest of Technical Papers, Transducers '01, 11th international conference on solid-state sensors and actuators (Munich, Germany, June 2001)*

[8] Isomura K, Murayama M, Teramoto S, Hikichi K, Endo Y, Togo S and Tanaka S 2006 Experimental verification of the feasibility of a 100 W class micro-scale gas turbine at an impeller diameter of 10 mm *J. Micromech. Microeng.***16 (9)** p S254-61 doi: 10.1088/0960-1317/16/9/S13

[9] Isomura K, Tanaka S, Togo S, Kanebako H, Murayama M, Saji N, Sato F and Esashi M 2005 Devlopment of micromachine gas turbine for portable power generation *JSME International Journal.***47(3)** p 459-64 doi: 10.1299/jsmeb.47.459

[10] Epstein A *et al.* Power MEMS and microengines 1997 *IEEE Transducers'97conf* (Chicago, IL, June 1997)

[11] Epstein A 2003 Millimeter-scale, MEMS gas turbine engines *Proc. ASME Turbo Expo'03* (Atlanta, Georgia, June 2003)

[12] Kahnna R 2003 MEMS fabrication perspective from the MIT microengine project *Surf Coat Tech* **163-164** p 273-80 doi:10.1016/S0257-8972(02)00637-0

[13] Fernandez-Pello A *et al.* 2003 MEMS rotary engine power system *IEEJ Trans.SM* **123(9)** p 326-330

[14] Fu K, Knobloch A, Martines F, Walther D, Fernandez-Pello C, Pisano A, Liepmann D, Miyaska K and Maruta K 2001 Design and experimental results of small scale rotary engines *Proc. ASME Int Mech. Eng, Congress and Expo.* (New York, Nov 2001) IMECE2001/MEMS-23924

[15] Sprague S B, Park S-W, Walther D C, Pisano A P and Fernandez-Pello C A 2007 Development and characterization of small-scale rotary engines *Int. J. Alternative Propulsion* **1(2/3)** p 275-93 doi: 10.1504/IJAP.2007.013016
[16] Lee C H, Jiang K C, Jin P and Prewett P D 2004 Design and fabrication of a micro-Wankel engine using MEMS technology *Microelectronic Eng* **73-74** p 529-34 doi:10.1016/j.mee.2004.03.030
[17] Jiang K C, Prewett P D, Ward W C, Tian Y and Yang Y 2001 Design of a micro-Wankel rotary engine for MEMS fabrication *Proc. SPIE* **4407** p 54-60
[18] Jin P, Jiang K and Sun N 2003 Microfabrication of ultra-thick SU-8 photoresist for microengines *Proc. SPIE* **4979** 105-110
[19] Aichlmayr H T, Kittelson D B and Zachariaah M R 2002 Miniature free-piston homogenous charge compression ignition engine-compressor concept –Part I: Performance estimation and design considerations unique to small dimensions *Chem Eng Sci* **57** (19) 4161-71 doi:10.1016/S0009-2509(02)00256-7
[20] Aichlmayr H T, Kittelson D B and Zachariaah M R 2002 Miniature free-piston homogenous charge compression ignition engine-compressor concept –Part II: Modeling HCCI combustion in small scales with detailed homogenous gas phase chemical kinetics *Chem Eng Sci* **57 (19)** 4173-86 doi:10.1016/S0009-2509(02)00257-9
[21] Frechette L G, Lee C, Arslan S and Liu Y-C 2003 Preliminary design of a MEMS steam turbine power plant on a chip *Proc. 3rd int'l Workshop on Micro & Nano Tech. for Power Generation & Energy Conv.* (PowerMEMS'03) (Makuhari, Japan, Dec 2003)
[22] Frechette L G, Lee C and Arslan S 2004 Development of a MEMS-based Rankine cycle steam turbine for power generation: project status *Proc. 4th int'l Workshop on Micro & Nano Tech. for Power Generation & Energy Conv.* (PowerMEMS'04) (Kyoto, Japan, Nov 2004) p 92-95
[23] Lee C, Liamini M and Fréchette L 2006 Design, fabrication and characterization of a microturbopump for a Rankine cycle micro power generator *Proc. 2006 Solid State Sensor, Actuator and Microsystem Workshop* (Hilton Head Island, SC, June 2006)
[24] Nakajima N, Ogawa K and Fujimasa I 1989 Study on micro engines-miniaturizing Stirling engines for actuator and heat pumps, micromechanics and MEMS *Proc. IEEE Micro electro mechanical system Workshop* (Salt Lake city, UT, USA, July 1989)
[25] Geng T, Schoen M A, Kuzentsov A V and Robert W L 2007 Combined numerical and experimental investigation of a 15-cm valveless pulsejet *Flow Turbulence Combust* **78** p 17-33 doi: 10.1007/s10494-006-9032-8
[26] Hashimoto K, Ogawa J, Toriyama T and Sugiyama S 2003 Design of a resonant micro reciprocating engine for power generation *Proc. TRANSDUCERS '03. The 12th International Conference on Solid State Sensors, Actuators and Microsystems* (Boston, June 2003)
[27] Strasser M, Aigne R, Lauterhach C, Stvr T, Franosch M and Wachutka G 2003 Micromachined cmos thermoelectric generators as on-chip power supply *Proc. TRANSDUCERS '03. The 12th International Conference on Solid State Sensors, Actuators and Microsystems* (Boston, June 2003)

[28] Leonov V, Fiorini P, Sedky S, Torfs T and Hoof C 2005 Thermoelectric mems generators as a power supply for a body area network *Proc. TRANSDUCERS'O5. The 13th International Conference on Solid-state Sensors, Actuators and Microsystems* (Seoul, Korea, June 2005)
[29] Sato N, Ishii H, Urano M, Sakata T, Teradal J, Morimura H, Shigematsu S, Kudou K, Kamei K and Machida K 2005 Novel mems power generator with integrated thermoelectric and vibrational devices *Proc. TRANSDUCERS'O5. The 13th Intemarional Conference on Solid-state Sensors, Actuators and Microsystems* (Seoul, Korea, June 2005)
[30] Wang W, Jia F, Huang Q and Zhang J 2004 A new type of low power thermoelectric micro-generator fabricated by nanowire array thermoelectric material *Microelectronic Eng* **77 (3-4)** p 223–29 doi:10.1016/j.mee.2004.11.005
[31] Bottner H, Nurnus J, Gavrikov A, Kuhner G, Jagle M, Kunzel C, Eberhard D, Plescher G, Schubert A and Schlereth K 2004 New thermoelectric components using microsystem technologies *J .Microelectromech S* **13** p 414-20
[32] Bardaweel H K, Anderson M J, Richards R F and Richards C D 2008 Optimization of the dynamic and thermal performance of a resonant micro heat engine *J. Micromech. Microeng* **18 (10)** 104014 doi: 10.1088/0960-1317/18/10/104014
[33] Whalen S, Thompson M, Bahr D, Richards C and Richards R 2003 Design, fabrication and testing of the P3 micro heat engine *Sensor Actuator A* **104 (3)** p 290-98 doi:10.1016/S0924-4247(03)00032-3
[34] Weiss L W, Cho J H, McNeil K E, Richards C D, Bahr D F and Richards R F 2006 Characterization of a dynamic micro heat engine with integrated thermal switch *J. Micromech. Microeng* **16 (9)** S262-69 doi: 10.1088/0960-1317/16/9/S14
[35] Cho J, Wiser T, Bahr D, Richards C and Richards R 2007 Fabrication and characterization of a thermal switch *Sensor Actuator A* **133** 55-63.
[36] Cho J H, Richards C D and Richards R F 2008 A facility for characterizing the steady-state and dynamic thermal performance of microelectromechanical system thermal switches *Rev Sci Instrum* **79 (3)** 034901
[37] Cho J H, Weiss L W, Richards C D, Bahr D F, and Richards R F 2007 Power production by a dynamic micro heat engine with an integrated thermal switch *J. Micromech. Microeng* **17 (9)** S217-23 doi: 10.1088/0960-1317/17/9/S02
[38] Weiss L W 2008 A novel MEMS-based micro heat engine and operating cycle *PhD thesis Washington State University*
[39] Whalen S 2004 Cycle work from a MEMS heat engine and characterization of the liquid-vapor phase change actuation mechanism *PhD thesis Washington State University*
[40] Hsu T 2002 MEMS and Microsystems Design and Manufacture McGraw Hill 1st ed
[41] Liu C 2006 Foundation of MEMS Pearson Prentic Hall 1st ed
[42] Lee H 2008 Experimental and numerical study of evaporating flow heat transfer in micro-channel *PhD thesis Washington State University*
[43] Snyder G J, Fleurial J-P, Calliat T, Yang R and Chen G 2002 Supercooling of Peltier cooler using a current pulse *J. Appl. Phys* **92 (3)** 1564-69 doi: 10.1063/1.1489713

[44] Cho J 2007 Design, fabrication and characterization of a MEMS thermal switch and integration with a dynamic micro heat engine *PhD thesis Washington State University*
[45] Bardaweel H K, Anderson M J, Weiss L W, Richards R F and Richards C D 2009 Characterization and modeling of the dynamic behavior of a liquid-vapor phase change actuator *Sensor Actuator A* **149 (2)** p 284-91 doi:10.1016/j.sna.2008.11.020
[46] Bardaweel H, Weiss L, Anderson M, Richards R and Richards C Characterization and modeling of the dynamic behavior of a liquid-vapor phase change actuator *Proc. ASME Int Mech. Eng, Congress and Expo.* (Seattle, Nov 2007) Paper No: IMECE2007-42567
[47] Schrage R 1953 A Theoretical Study of Interphase Mass Transfer New York: Columbia University Press
[48] Boethling R S and MacKay D 2000 Handbook of Property Estimation Methods for Chemicals: Environmental and Health Sciences Boca Raton, FL: CRC Press
[49] Kinsler L, Frey A, Coppens A and Sanders J 2000 Fundamentals of Acoustics Wiley 4th ed
[50] Haberman R 2004 Applied Partial Differential Equations with Fourier Series and Boundary Value Problems Pearson Prentic Hall 4th ed
[51] Palm III W 2000 Modeling, Analysis and Control of Dynamic Systems Wiley 2nd ed
[52] Vlassak J J and Nix W D 1992 A New bulge test technique for the determination of Young's modulus and Poisson's ratio of thin film *J Mater Res* **7(12)** p 3242-49 doi: 10.1557/JMR.1992.3242
[53] Robinson M 2007 Microstructural and geometric effects on the piezoelectric performance of PZT MEMS *PhD thesis Washington State University*
[54] Cengel Y and Boles M 1994 Thermodynamics An Engineering Approach McGraw Hill 2nd ed
[55] Burden R and Faires J 2005 Numerical Analysis Thomson Higher Education 8th ed

Appendix A

Solution of the linearized model of the micro heat engine

The linearized set (5.16) can be represented as:

$$[A]\left\{\dot{X}\right\} = [B]\{X\} + q(t)\{C\} \quad , \tag{A-1}$$

where the state variables are given by

$$\{X\} = \begin{Bmatrix} \Delta V_g \\ \Delta \dot{V}_g \\ \Delta p \\ \Delta T \\ \Delta T_l \end{Bmatrix}.$$

The coefficient matrices $[A]$ and $[B]$ are the coefficient matrices of the unknowns column vectors $\left\{\dot{X}\right\}$ and $\left\{X\right\}$ respectively. The coefficient matrices [A] and [B] are given by

$$[A] = \begin{bmatrix} 1 & 0 & 0 & 0 & 0 \\ \dfrac{(b + b_f)}{(\pi r_o^2)^2} & \dfrac{(m + \overline{m})}{(\pi r_o^2)^2} & 0 & 0 & 0 \\ 0 & 0 & 0 & 0 & C_T \\ 1 & 0 & \left(\dfrac{V_o}{\rho_o R T_o} + \dfrac{(\pi r_i^2)^2}{s_h} \right) & \dfrac{V_o}{T_o} & 0 \\ 0 & 0 & -\dfrac{V_o}{\rho_o C_p T_o} & \dfrac{V_o}{T_o} & 0 \end{bmatrix}$$

$$[B]=\begin{bmatrix} 0 & 1 & 0 & 0 & 0 \\ \dfrac{-s}{\left(\pi r_o^2\right)^2} & 0 & 1 & 0 & 0 \\ 0 & 0 & h_{fg}S\sqrt{\dfrac{M}{2\pi R_u}}\,\dfrac{\gamma+1}{2\gamma\sqrt{T_o}} & 0 & -\left(U+h_{fg}BS\sqrt{\dfrac{M}{2\pi R_u}}\right) \\ 0 & 0 & -\dfrac{S}{\rho_o}\sqrt{\dfrac{M}{2\pi R_u}}\,\dfrac{1}{\sqrt{T_o}} & \dfrac{S}{\rho_o}\sqrt{\dfrac{M}{2\pi R_u}}\,\dfrac{\rho R}{2\sqrt{T_o}} & B \\ 0 & 0 & 0 & -\dfrac{U_B}{\rho_o c_p T_o} & 0 \end{bmatrix}$$

The column vector $\{C\}$ represents the coefficients of the input rate of heat $q(t)$, given by

$$\{C\}=\begin{Bmatrix} 0 \\ 0 \\ 1 \\ 0 \\ 0 \end{Bmatrix}$$

The solution of the linear system (A-1) takes the form

$$X_i = \hat{X}_i\, e^{j\,2\pi f_o t} \quad , \tag{A-2}$$

and the derivative of (A-2) is given by

$$\dot{X} = j(2\pi f_o)\,\hat{X}_i\, e^{j\,2\pi f_o t} \quad . \tag{A-3}$$

By substituting (A-2) and (A-3) into (A-1), the linear set (A-1) becomes a set of algebraic equations. In solving for the state variables set $\{X\}$, MATLAB code was used.

Appendix B
FFT algorithm

```
%
clear all;
close all;
clc
%=============================================================
=======
%FFT algorithm.
%=============================================================
=======
load m5u.txt -ascii        ; %Loading the input data file.
x=m5u(:,7)                 ; %Deflection array.
t=m5u(:,1)                 ; %Time array.
x0=x                       ;
t0=t                       ;
N=5000                     ; %Number of sampling points.
dt=t(2)-t(1)               ; %Sampling frequency.
fs=1/dt                    ;
fn1=fs/2                   ;
y1=fft(x)                  ;
y1=y1(1:(N/2)+1)           ;
m1=abs(y1)                 ;
p1=angle(y1)*(180/pi)      ;
m1=(2/N)*m1                ;
f=linspace(0,fn1,(N/2)+1) ; %Creating the frequency array.
m01=m1.*(2*pi*f')          ;
%=============================================================
=======
v=m5u(:,6)                   ; %Voltage to the heater.
v1=1.94-v                    ;
R=8.8                        ; %Measured resistance of the
heater.
y2=fft(v1.^2/(R))            ;
y2=y2(1:(N/2)+1)             ;
m2=abs(y2)                   ;
m02=(2/N)*m2                 ;
p2=angle(y2)*(180/pi)        ;
f=linspace(0,fn1,(N/2)+1)    ;
g1=angle(y1./y2)*(180/pi)    ;
%=============================================================
=======
figure
subplot(2,1,1)
loglog(f',m01./m02,'b')     ;
grid on                     ;
ylabel('(mic/sec)/watt')
```

```
xlabel('frequency(Hz)')
title('Velocity transfer function of the SiNx membrane')
%
subplot(2,1,2)
semilogx(f,g1,'b')
xlabel('frequency(Hz)')
ylabel('angel(2*pi*f*m1)*180/pi')
title('Phase angle of the velocity transfer function of
SiNx membrane ')
%
figure
subplot(2,1,1)
plot(t0,x0,'b')
grid on
ylabel('Deflection(mic)')
xlabel('time(sec)')
title('deflection of the SiNx membranes measured in
micrometers')
%
data =[f',m01./m02 ,g1]    ;
save TFS0.1.dat data -ascii;
%
```

Appendix C

Least squares algorithm

```
clear all;
close all;
clc
%=====================================
%Least square method
%=====================================
EnginePars8mmCantilever                  ;%Calling the file
with properties.
P1=P                                     ;%P:structure.
%=====================================
load testopencir.dat;
M=testopencir       ;
M=M(2:end,:)        ;
%=========================================
%Define the floating parameters;
%Initial guess for the floating parameters;
%=========================================
X0(1)=P1.U*1          ; %Heat losses from liquid layer.
X0(2)=P1.CT*10        ; %Thermal storage.
X0(3)=P1.b*1          ; %Damping.
X0(4)=P1.hB*1         ; %Heat losses from the bubble.
X0(5)=P1.m*1          ; %Equivalent mass.
% Seeting upper and lower bounds on the values.
lb(1)=0;    ub(1)=10000    ;
lb(2)=0;    ub(2)=10000    ;
lb(3)=0;    ub(3)=1000     ;
lb(4)=0;    ub(4)=1000     ;
lb(5)=0;    ub(5)=1000     ;
%=========================================
%calling the Minimizer function to perform the
optimization.
%=========================================
%OPTIONS(1)=1
;
P.Nfit=35           ;
P1.Nfit=P.Nfit      ;
% calling the optimization function.
Xd = fmincon(@(X)
squarederrorfcn(X,P1,M),X0,[],[],[],[],lb,ub,[],[]);
```

```
Xd                                                          ;
% Update the floating parameters to the final values.
P1.U     =Xd(1);
P1.CT    =Xd(2);
P1.b     =Xd(3);
P1.hB    =Xd(4);
P1.m     =Xd(5);
% updating the P structure.
P1.Rb=(P1.U/P1.hfg)/((P1.U/P1.hfg)+P1.B)
P1.Rb=P1.Rb*(P1.betab/P1.rhov)*sqrt(P1.M/(2*pi*P1.Ru))*(P1.
g+1)/(2*P1.g*sqrt(P1.To))

P1.Rb=1/P1.Rb
P1.R1=(P1.b)/((pi*P1.ro^2)^2)
%
f  =M(:,1);
xm =M(:,2 ;
xp =M(:,3);
%
P1.Rb=(P1.U/P1.hfg)/((P1.U/P1.hfg)+P1.B)
P1.Rb=P1.Rb*(P1.betab/P1.rhov)*sqrt(P1.M/(2*pi*P1.Ru))*(P1.
g+1)/(2*P1.g*sqrt(P1.To))
P1.Rb=1/P1.Rb
P1.Cb=(P1.Vo/(P1.g*P1.rhov*P1.R*P1.To))+(((pi*P1.ri^2)^2)/P
1.sh)
P1.R1=(P1.b)/((pi*P1.ro^2)^2)
P1.C1=((pi*P1.ro^2)^2)/P1.s
%=========================================
%Solving the linear set model using the updated values of
the floating parameters.
for j1=1:P1.Nfit
     warning off                        ;
     Y(:,j1)=freqres1(2*pi*f(j1),P1);
     warning on                         ;
end

R=((Y(1,:)/(pi*P1.ro^2))*1e6)';
R=abs(R)                            ;
Ph=angle(Y(1,:))'*(180/pi)     ;
%=========================================
%Plotting.
figure
subplot(2,1,1)
h1=loglog(f(1:P1.Nfit),abs((Y(1,:)/(pi*P1.ro^2))*1e6'),'g-'
...
                     ,f,xm,'bs')
ylabel(' \Gamma[kf_{p}](µm/W)')
```

```
legend(h1,'Model \Gamma','Measured X_{k}/Q_{k}')
title([ '  CT=',num2str(P1.CT)                    ...
       ,'  U =',num2str(P1.U)                     ...
       ,'  b =',num2str(P1.b)                     ...
       ,'  hB=',num2str(P1.hB)                    ...
       ,'  m =',num2str(P1.m)])
grid on
%
subplot(2,1,2);
semilogx(f(1:P1.Nfit),Ph ,'g-'  ...
                        ,f,xp ,'bs' )

xlabel(['Frequency (kHz)'])                          ;
ylabel(['Phase (deg)'])                              ;
title('Phase of the dispalcment tranfer function')
grid on
%
figure
subplot(2,1,1)
h2=loglog(f(1:P1.Nfit),abs((2*pi*f(1:P1.Nfit)').*(Y(1,:)/(p
i*P1.ro^2))*1e3'),'g-'...
,f,abs((2*pi*f).*xm*1e-3),'bs')
legend(h2,'Model \Gamma','Measured X_{k}/Q_{k}')
ylabel(' \Gamma[kf_{p}] (mm/s/W)')
title('Velocity transfer function ')
grid on
%==========================================================
=================
%Export the data as output files.
PTF=abs((2*pi*f(1:P1.Nfit)').*(Y(1,:)/(pi*P1.ro^2))*1e3') ;
MTF=abs((2*pi*f).*xm*1e-3)                               ;
fd =f(1:35)                                              ;
data=[fd,PTF']                                           ;
save modelvel.dat  data -ascii
data=[f,MTF]                                             ;
save measuredvel.dat  data -ascii

%==========================================================
=====
```

EnginePars8mmCantilever

```
clear all;
close all;
%=====================================================
%Working fluid properties.
%=====================================================

P.rhov=3.53                                          ;
P.rhol=1775                                          ;
P.mul=467.04e-6                                      ;
P.M=338/1000                                         ;
P.Ru=8.31                                            ;
P.Ah=9.73                                            ;
P.Bh=1562                                            ;
P.Ch=0                                               ;
P.cp=755.2                                           ;
Psat=25.097                                          ;
P.R=(Psat*1000)/(P.rhov*(273+21))                    ;
P.cv=P.cp-P.R                                        ;
P.g=P.cp/P.cv                                        ;
P.hfg=94.05e03                                       ;
%=====================================================
% Properties of the engine
%=====================================================

P.s    =2435              ; % Corrected stiffness.
P.ro   =(10e-3)/2         ;
P.ri   =0.9*P.ro          ;
P.L    =150e-6            ;
P.S    =pi*P.ri^2         ;
P.Vo   =P.S*P.L           ;
P.beta =1.0               ;
P.betab=P.beta*P.S        ;
P.sh   =5600              ;
P.b    =0.1               ;
P.CT   =1e-1              ;
P.hB   =1e-6              ;
P.m    =2.0e-3            ;
%=====================================================
% Environmental parameters
%=====================================================

P.To=294                             ;
P.Po=10^(P.Ah-(P.Bh/(P.To+P.Ch)));
%=====================================================
```

```
% Computed parameters
%=====================================================

P.B=P.betab*sqrt(P.M/(2*pi*P.Ru))                                ;
P.B=P.B*(10^(P.Ah-(P.Bh/(P.To+P.Ch))))/sqrt(P.To)                ;
P.B=P.B*( ((P.Bh*log(10))/(P.To+P.Ch)^2)-(1/(2*P.To)) )          ;
P.U=1*P.B*P.hfg                                                  ;
P.Rb=(P.U/P.hfg)/((P.U/P.hfg)+P.B)                               ;
P.Rb=P.Rb*(P.betab/P.rhov)*sqrt(P.M/(2*pi*P.Ru))*(P.g+1)/(2
*P.g*sqrt(P.To))
;
P.Rb=1/P.Rb                                                      ;
P.Cb=(P.Vo/(P.g*P.rhov*P.R*P.To))+(((pi*P.ri^2)^2)/P.sh);
P.R1=(P.b)/((pi*P.ro^2)^2)                                       ;
P.C1=((pi*P.ro^2)^2)/P.s                                         ;
```

Freqres1

```
%This function is called upon solving the linear set of
equations.
function X=freqres1(w,P)
%  X(1)= Delta V
%  X(2)= Delta Vdot
%  X(3)= Delta p
%  X(4)= Delta rhov
%  X(5)= Delta T
%  X(6)= (psi/pi*ro^2)*V
%  X(7)= Delta Tl
%
A1=zeros(6,6);B1=zeros(6,6); C1=zeros(6,1);
%=====================================================
% Row 1 Newtons Law for Diaphragm
A1(1,1)=1                                                ;
% Row 2 Newtons Law for Diaphragm
 A1(2,2)=(P.m)/(pi*P.ro^2)^2                             ;
% Row 3 Conservation of Mass
A1(3,1)=P.rhov                                           ;
A1(3,3)=P.rhov*((pi*P.ri^2)^2)/P.sh                      ;
A1(3,4)=P.Vo                                             ;
% Row 4 Conservation of Energy
A1(4,4)=-(P.Vo*P.Po)/P.rhov                              ;
A1(4,5)=P.rhov*P.Vo*P.cv                                 ;
% Row 5 Ideal Gas
A1(5,3)=-1/(P.R*P.To)                                    ;
A1(5,4)=1                                                ;
A1(5,5)=P.Po/(P.R*P.To^2)                                ;
% Row 6 Energy Conservation for liquid layer
A1(6,6)=P.CT                                             ;
%=====================================================
% Row 1 Newtons Law for Diaphragm
B1(1,2)=1                                                ;
% Row 2 Newtons Law for Diaphragm
B1(2,1)=-P.s/(pi*P.ro^2)^2                               ;
B1(2,2)=-(P.b)/(pi*P.ro^2)^2                             ;
B1(2,3)=1                                                ;
% Row 3 Conservation of Mass
B1(3,3)=-P.betab*sqrt(P.M/(2*pi*P.Ru))*(1/sqrt(P.To))    ;
B1(3,5)=P.betab*sqrt(P.M/(2*pi*P.Ru))*((P.rhov*P.R)/(2*sqrt
(P.To)))
;
B1(3,6)=P.B                                              ;
% Row 4 Conservation of Energy
```

```
B1(4,5)=-P.hB                                                    ;
% Row 6 Energy Conservation for liquid layer
B1(6,3)=P.hfg*P.betab*sqrt(P.M/(2*pi*P.Ru))*(1/sqrt(P.To))
;
B1(6,5)=-P.hfg*P.betab*sqrt(P.M/(2*pi*P.Ru))*
        ((P.rhov*P.R)/(2*sqrt(P.To)))
;
B1(6,6)=-(P.hfg*P.B+P.U)
;
%=========================================================
% Row 7 Energy Conservation for liquid layer
C1(6,1)=1
;
%X=inv(i*w*A1-B1)*C1;
X=(i*w*A1-B1)\C1    ;
```

Squarederrorfcn

```
%This function calculates the square of the error to be
used for optimization step later on.
function K=squarederrorfcn(X,P1,M)
%M is the experimental data.
%P is the model parameter.
%X is the floating parameters in the model.
%==============================
%Define the floating parameters.
P1.U    =X(1);
P1.CT   =X(2);
P1.b    =X(3);
P1.hB   =X(4);
P1.m    =X(5);
%
P1.Rb=(P1.U/P1.hfg)/((P1.U/P1.hfg)+P1.B);
P1.Rb=P1.Rb*(P1.betab/P1.rhov)*sqrt(P1.M/(2*pi*P1.Ru))*(P1.
g+1)/(2*P1.g*sqrt(P1.To))                    ;
P1.Rb=1/P1.Rb                          ;
P1.R1=(P1.b)/((pi*P1.ro^2)^2)          ;
P1.L1=(P1.m)/((pi*P1.ro^2)^2)          ;
%==============================
f =M(:,1);
xm=M(:,2);
xm=xm'   ;
xp=M(:,3);
%==============================
%Compute the predicted data from the model parameters
%==============================
for j1=1:P1.Nfit
     warning off                       ;
     Y(:,j1)=freqres1(2*pi*f(j1),P1);
     warning on                        ;
end

Y1=(Y(1,:)/(pi*P1.ro^2))*1e6        ; %Y1 is the deflection
in micrometers
%==============================
%Compute the square of the error for each data point
%==============================
K=0; %initialize the error to be zero.
for i1=1:P1.Nfit
    K=K+((xm(i1)-abs(Y1(i1)))/xm(i1))^2
end
```

Appendix D

Modeled Pressure-volume diagram (for specified heat input)

```
clear all;
close all;
clc
%=======================================
EnginePars8mmCantilever;
P1  =P                                  ;
N   =500                                ;
fn  =130.0                              ;%fn: resonant
frequency
i1  =200                                ;
ti  =0.0                                ;%Initial time.
Tp  =1*(1/fn)                           ;%fundamental period.
T   =(0.01*Tp)                          ;%pulse duration
j1  =0:i1                               ;
t   =(j1/i1)*(Tp-ti)+ti                 ;%generated time
array.
E   =1.0e-3                             ;%input energy
%=======================================
for k2=1:N
     warning off                                ;
     Y(:,k2)   =freqres1(2*pi*(k2./Tp),P1)      ;
     warning on                                 ;
end
%=======================================
VOL     =(Y(1,:))                           ;
VOL     =2*(Y(1,:))                         ;
PRE     =(Y(3,:))                           ;
% Define the heating/cooling pulse shape in terms of
Fourier series.
for d1=1:i1
   for k=1:N
L1   =(2./(k*pi))*sin((T./Tp)*k*pi)
L2   =cos((T./Tp)*k*pi)
L3   =cos(2*pi*(k/Tp).*t(d1))
L4   =(2/(k*pi))*((cos(((T/Tp)*k*pi)).^2)-1)
      *sin(2*pi*(k/Tp)*t(d1))
```

```
L5   =(2/(k*pi))*sin((T/Tp)*k*pi)*cos((T/Tp)*k*pi)
       *cos(2*pi*(k/Tp)*(t(d1)-(Tp/2)))
L6   =(2/(k*pi))*((cos(((T/Tp)*k*pi)).^2)-1)
       *sin(2*pi*(k/Tp)*(t(d1)-(Tp/2)))
q(k) =((L1*L2*L3)-L4)-(L5-L6)

%VOLUME CHANGES INSDIE THE ENGINE/CONVERTED TO TIME DOMAIN
V1   =(2./(k*pi))*(abs(VOL(k)))*sin((T./Tp)*k*pi)
V2   =cos((T./Tp)*k*pi)
V3   =cos(2*pi*(k/Tp).*t(d1)+angle(VOL(k)))
V4   =(2/(k*pi))*(abs(VOL(k)))*((cos(((T/Tp)*k*pi)).^2)-
       1)*sin(2*pi*(k/Tp)*t(d1)+angle(VOL(k)))
V5   =(2/(k*pi))*(abs(VOL(k)))*sin((T/Tp)*k*pi)*
      cos((T/Tp)*k*pi)*cos(2*pi*(k/Tp)*(t(d1)-
      (Tp/2))+angle(VOL(k)))
V6   =(2/(k*pi))*(abs(VOL(k)))*((cos(((T/Tp)*k*pi)).^2)-
       1)*sin(2*pi*(k/Tp)*(t(d1)-(Tp/2))+angle(VOL(k)))
VOLUME(k) =((V1*V2*V3)-V4)-(V5-V6)

%PRESSURE RISE INSIDE THE ENGINE/CONVERTED TO TIME DOMAIN
P1   =(2./(k*pi))*(abs(PRE(k)))*sin((T./Tp)*k*pi)
P2   =cos((T./Tp)*k*pi)
P3   =cos(2*pi*(k/Tp).*t(d1)+angle(PRE(k)))
P4   =(2/(k*pi))*(abs(PRE(k)))*((cos(((T/Tp)*k*pi)).^2)-
       1)*sin(2*pi*(k/Tp)*t(d1)+angle(PRE(k)))
P5   =(2/(k*pi))*(abs(PRE(k)))*sin((T/Tp)*k*pi)*
      cos((T/Tp)*k*pi)*cos(2*pi*(k/Tp)*(t(d1)-
      (Tp/2))+angle(PRE(k)))
P6   =(2/(k*pi))*(abs(PRE(k)))*((cos(((T/Tp)*k*pi)).^2)-
       1)*sin(2*pi*(k/Tp)*(t(d1)-(Tp/2))+angle(PRE(k)))

PRESSURE(k) =((P1*P2*P3)-P4)-(P5-P6)
end
   Q1(d1)=(E/T)*sum(q)                          ;%HEAT FUNCTION.
   VOLUME1(d1)=(E/T)*sum(VOLUME)                ;%VOLUME
CHANGES.
   PRESSURE1(d1)=(E/T)*sum(PRESSURE)            ;%PRESSURE RISE.
End

%Plotting
figure
subplot(2,1,1)
  plot(VOLUME1*1.0e9,PRESSURE1*1e-3,'-o')
subplot(2,1,2)
  plot(t(1:200),Q1,t(1:200),PRESSURE1*1.0e-3,'-')
```

```
figure
subplot(2,1,1)
  plot(t(1:200),Q1,t(1:200),(VOLUME1/(pi*P.ro^2))*1.0e6,'-
')
subplot(2,1,2)
  plot(t(1:200),Q1)
%
X1 =VOLUME1*1.0e9
Y1 =PRESSURE1*1e-3
data=[X1',Y1']
save PREVOL2.dat  data -ascii
%=========================================
```